Investigation of novel freestanding heterostructures

Dissertation

Zur Erlangung des Doktorgrades der Naturwissenschaften
(Dr. rer. nat.)

der

Naturwissenschaftlichen Fakultät II
Chemie, Physik und Mathematik

der Martin-Luther-Universität
Halle-Wittenberg

Vorgelegt von

Herrn Ke Gu

Gutachter: Prof. Dr. Stuart S.P. Parkin
Prof. Dr. Ingrid Mertig
Prof. Dr. Amalio Fernández-Pacheco

Tag der öffentlichen Verteidigung: 25.07.2024

Eidesstattliche Erklärung

Hiermit erkläre ich, dass ich die vorliegende Arbeit selbstständig verfasst und keine anderen als die angegebenen Quellen und Hilfsmittel benutzt habe. Alle Stellen der Arbeit, die wörtlich oder sinngemäß aus anderen Quellen übernommen wurden, sind als solche kenntlich gemacht. Ich habe keine vergeblichen Promotionsversuche unternommen und keine Dissertation an einer anderen wissenschaftlichen Einrichtung zur Erlangung eines akademischen Grades eingereicht. Ich bin weder vorgestraft noch sind gegen mich Ermittlungsverfahren anhängig.

Halle (Saale), den 31.10.2023,

Ke Gu

Acknowledgments

In May 2020, I came to Halle (Saale), a small but beautiful city. It was a hard time because of COVID, and I was asked to take a 2-week quarantine before starting my job at Max Planck Institute of Microstructure Physics. I also felt more or less isolated for the first few months, as there were few connections and everything was online. At that time, I could not imagine how fruitful these 4 years would be. Looking back on the days I spent at MPI-Halle, I realize how much support I have received.

First of all, I would like to express my greatest appreciation to my supervisor, Prof. Stuart Parkin, for providing me with the invaluable opportunity to study at our institute and to join the prestigious Max Planck Society. I would like to thank him for his guidance during my Ph.D. studies, which has been crucial for my academic career: he provided me with a platform that allowed me to access the most cutting-edge research fields and facilities, and to interact effectively with researchers with different expertise; his insightful and creative inputs during discussions have both improved my research abilities and made me more enthusiastic about my field of study; his trust in my work has been a constant motivation for me to continue my studies; his hardworking attitude has been a model for me. It is always a great experience to work with Stuart and I am sure that this pleasant experience will have a great impact on my future life, not only in the academic part.

I would also like to thank Prof. Ingrid Mertig, my co-supervisor at the International Max Planck Research School for Science and Technology of Nano-Systems (IMPRS-STNS). Unlike us, as theoretical physicists, she has provided me with enlightening perspectives from a different point of view than our experimentalists. I have learnt a lot from her.

Furthermore, I would also like to express my gratitude to Prof. Tetsuya Hasegawa (retired from The University of Tokyo), who supervised me during my M.Sc. studies, and Prof. Tsukasa Katayama (Hokkaido University), who was my subgroup leader at that time. They cultivated my interest in solid state physics, helped me learn deposition and characterizations techniques, and guided me through the whole process of a project from idea to manuscript. The perseverance I acquired at that time is very important for my Ph.D. research.

I would like to give special thanks to Dr. Fan Li, Dr. Binoy Krishna Hazra and Dr. Yicheng Guan, who have continuously supported me during my Ph.D. research through our productive discussions and collaborations. I have learnt a lot from their deep knowl-

edge of experimental facilities and theories. Their research successes also encourage me to move forward.

Special thanks also go to all of my collaborators, including Dr. Hakan Deniz, Dr. Wenjie Zhang, Dr. Peng Wang, Dr. Abhay Kant Srivastava, Norbert Schammelt, Yasser Pordeli, Kajal Tiwari, Zihan Yin, Zhong Wang, etc. Without their contributions, I could not have fulfilled our research goals.

I have enjoyed a lot working here at MPI-Halle with wonderful colleagues, such as Dr. Jae-Chun Jeon, Dr. Andrea Migliorini, Dr. Fang Chi, Dr. Tianping Ma, Dr. Hyeon Han, Berthold Rimmler, Mostafa Marzouk, Jiho Yoon, Tianzhe Chen, Jingrong Ji, Jibo Zhang, Guanmin Li, Yishen Xie, Mingqun Qi, and so on. I would like to thank them all for their numerous help and the joyful time we spent together.

As a member of IMPRS-STNS, I participated in many well-organized activities such as workshops, retreats, seminars, etc. Through these activities, I have built relationships with other students and gained many useful skills such as poster design, organizing presentations and so on. Therefore, I would like to thank Antje Paetzold, Michael Strauch and Dr. Ann-Kristin Flieger for their selfless dedication and valuable support in making this IMPRS-STNS project run smoothly and be successful for the first 5-year evaluation. I am sure that this project can be even more significant and successful in the future.

I would also like to express my sincere gratitude to my friends. Apart from life in the lab, we have shared countless moments of laughter together. Their unwavering friendship has been a source of strength throughout my Ph.D. studies.

Finally, I would like to express my deepest gratitude to my parents for their love, tolerance and support over the years. They have encouraged me to follow my own interests and to study abroad. Yet academic life is hard and highly competitive, their company gives me the strength to move on determinedly.

Abstract

Freestanding thin films exhibit many intriguing properties and can be readily integrated with other types of materials and structures to create novel properties, going beyond normal epitaxial thin films and facilitating applications in next-generation devices and the investigation of emergent phenomena. In this thesis, we utilize a water membrane based lift-off and transfer technique to fabricate several different types of freestanding heterostructures and systematically investigate their functionalities and device performance.

The fabrication of three-dimensional (3D) nanostructures is crucial for nanoelectronic devices with a small device footprint. One of the most promising future memory devices is magnetic racetrack memory (RTM), in which data is encoded in magnetic nanoobjects, e.g. magnetic domain walls (DWs), which are moved along nanowires by current pulses. RTM is promising due to its high packing density, low energy consumption and high speed. However, so far it has only been explored in two dimensions. Here, we show that freestanding racetracks formed from heavy metal/ferromagnetic (HM/FM) heterostructures have comparable device performance to those fabricated from conventional as-deposited thin films. Having demonstrated that the structures and magnetic properties of freestanding HM/FM heterostructures are largely preserved throughout the entire process, we then fabricate, for the first time, 3D racetracks by covering protrusions patterned on a sapphire substrate with freestanding magnetic membranes. We show that the current-induced DW motion (CIDWM) in 3D racetracks formed from HM/FM heterostructures can be modulated by the local geometry. We further demonstrate efficient CIDWM with a velocity of up to 600 m s^{-1} in 3D racetracks formed from freestanding synthetic antiferromagnetic heterostructures transferred onto $\sim$900 nm high protrusions. In addition, we fabricate freestanding HM/FM racetracks without any buffer layer and reduce the thickness of the HM layer down to 25 Å. We show that they have almost identical performance to the devices formed from conventional HM/FM heterostructures. Freestanding magnetic heterostructures, as demonstrated here, may enable future DW logic and 3D spintronic devices with high data capacity.

Another application of the water membrane based freestanding technique is to form "Twisted structures". Due to the rich interactions at twisted interfaces, twistronics has attracted much attention and sparked a wealth of new physics. However, up till now, twisted correlated oxides, which can stimulate the discovery of novel phenomena, have been little studied. Through our technique, we create twisted $La_{2/3}Sr_{1/3}MnO_3$ bilayers with a con-

trollable twist angle that show anomalous diamagnetic behavior. This diamagnetism is attributed to the appearance of antiferromagnetic coupling at the twisted interface.

Our results demonstrate the robustness and versatility of the water membrane based freestanding technique and show the great potential of freestanding heterostructures not only in applications such as memory devices, but also in fundamental research.

Zusammenfassung

Freistehende dünne Schichten weisen viele faszinierende Eigenschaften und können leicht mit anderen Arten von Materialien und Strukturen integriert werden, um neuartige Eigenschaften zu erzeugen, die über normale epitaktische Dünnschichten hinausgehen und Anwendungen in elektronischen Bauelementen der nächsten Generation sowie die Untersuchung neuartiger Phänomene erleichtern. In dieser Arbeit wird eine auf Wassermembranen basierende Abhebe- und Transfertechnik genutzt, um verschiedene Arten von freistehenden Heterostrukturen herzustellen, deren Funktionalitäten und Leistung anschließend systematisch untersucht werden.

Die Herstellung von dreidimensionalen (3D) Nanostrukturen ist entscheidend für nanoelektronische Bauelemente mit geringem Platzbedarf. Eine der vielversprechendsten zukünftigen Speichertechologien ist der magnetische Racetrack-Speicher (engl. *magnetic racetrack memory*, RTM), bei dem Daten in magnetischen Nanoobjekten wie magnetischen Domänenwänden (DWs) kodiert werden, die durch Stromimpulse entlang von Nanodrähten bewegt werden. RTM ist aufgrund der hohen Packungsdichte, des geringen Energieverbrauchs und der hohen Geschwindigkeit vielversprechend. Bislang wurde es jedoch nur in zwei Dimensionen erforscht. Hier wird gezeigt, dass freistehende Racetracks, die aus Heterostrukturen von Schwermetallen (engl. *heavy metal*, HM) und Ferromagneten (FM) gebildet werden, eine vergleichbare Leistung aufweisen wie solche, die aus konventionellen, direkt abgeschiedenen Dünnschichten hergestellt werden. Nachdem gezeigt wurde, dass die Strukturen und magnetischen Eigenschaften von freistehenden HM/FM-Heterostrukturen während des gesamten Prozesses weitgehend erhalten bleiben, werden zum ersten Mal 3D-Racetracks hergestellt, indem auf einem Saphirsubstrat strukturierte Vorsprünge mit freistehenden magnetischen Membranen bedeckt werden. Es wird gezeigt, dass die strominduzierte DW-Bewegung (engl. *current-induced domain wall motion*, CIDWM) in 3D-Racetracks, die aus HM/FM-Heterostrukturen gebildet werden, durch die lokale Geometrie moduliert werden kann. Des Weiteren wird effiziente CIDWM mit einer Geschwindigkeit von bis zu 600 m s^{-1} in 3D-Racetracks demonstriert, die aus freistehenden synthetischen antiferromagnetischen Heterostrukturen gebildet werden, die auf ~ 900 nm hohe Vorsprünge übertragen werden. Darüber hinaus werden freistehende HM/FM-Racetracks ohne Pufferschicht hergestellt und die Dicke der HM-Schicht auf 25 Å reduziert. Es wird gezeigt, dass sie eine fast identische Leistung wie die aus herkömmlichen HM/FM-Heterostrukturen hergestellten Bauelemente aufweisen.

Freistehende magnetische Heterostrukturen, wie hier demonstriert, könnten zukünftige DW-Logik- und 3D-Spintronik-Bauelemente mit hoher Datenkapazität ermöglichen.

Eine weitere Anwendung der auf Wassermembranen basierenden freistehenden Technik ist die Bildung "verdrehter Strukturen" (engl. *twisted*). Aufgrund der reichhaltigen Wechselwirkungen an verdrehten Grenzflächen hat die Twistronik viel Aufmerksamkeit auf sich gezogen und eine Fülle neuer physikalischer Erkenntnisse hervorgebracht. Bislang wurden verdrehte korrelierte Oxide, die zur Entdeckung neuer Phänomene anregen können, jedoch nur wenig untersucht. Mit der hier verwendeten Technik werden verdrehte $La_{2/3}Sr_{1/3}MnO_3$-Doppelschichten mit einem kontrollierbaren Verdrehungungswinkel erzeugt, die ein anomales diamagnetisches Verhalten zeigen. Dieser Diamagnetismus wird auf das Auftreten von antiferromagnetischer Kopplung an der verdrehten Grenzfläche zurückgeführt.

Unsere Ergebnisse belegen die Robustheit und Vielseitigkeit der auf Wassermembranen basierenden freistehenden Technik und zeigen das große Potenzial freistehender Heterostrukturen nicht nur für Anwendungen wie Speicherbauelemente, sondern auch für die Grundlagenforschung.

Glossary

Terms	
2D	Two-dimensional
3D	Three-dimensional
AFM	Atomic force microscopy
ALD	Atomic layer deposition
CIDWM	Current-induced domain wall motion
CVD	Chemical vapor deposition
DMI	Dzyaloshinskii–Moriya interaction
DW	Domain wall
EBL	Electron beam lithography
ECT	Exchange coupling torque
FeRAM	Ferroelectric Random Access Memory
FIB	Focused ion beam
FM	Ferromagnetic
FMR	Ferromagnetic resonance
FTJ	Ferroelectric tunnel junction
HM	Heavy metal
ICT	Information and Communication Technology
IP	In-plane
MBE	Molecular beam epitaxy
MFM	Magnetic force microscopy
MOKE	Magneto-optic Kerr effect
MRAM	Magnetic Random Access Memory
MTJ	Magnetic tunnel junction
OOP	Out-of-plane
PFM	Piezoresponse force microscope
PLD	Pulsed laser deposition
PMA	Perpendicular magnetic anisotropy
PPMS	Physical Property Measurement System
PVD	Physical vapor deposition
RHEED	Reflection high energy electron diffraction

Terms	
RKKY	Ruderman–Kittel–Kasuya–Yosida
RMS	Root mean square
RTM	Racetrack Memory
SAF	Synthetic antiferromagnetic
SEM	Scanning electron microscopy
SHE	Spin Hall effect
SOC	Spin-orbit coupling
SOT	Spin-orbit torque
SQUID	Superconducting quantum interference device
SS	Subthreshold swing
STT	Spin-transfer torque
TEM	Transmission electron microscopy
VdW	Van der Waals
VSM	Vibrating-sample magnetometer
XRD	X-ray diffraction

Contents

Chapter 1

Introduction

"It might tell us much of great interest about the strange phenomena that occur in complex situations," said by Richard Feynman in his famous lecture "There is Plenty of Room at the Bottom" when describing the importance of the field at the bottom [1]. As he proposed in his visionary lecture, thin films or two-dimensional (2D) materials could host properties not present in three-dimensional (3D) single crystals, while heterostructures could host phenomena not present in the constituent phases. These words are still relevant even today after almost 65 years. In recent decades, thin films and 2D materials, such as perovskite oxide thin films, graphene and other materials have attracted much attention due to their exotic properties including superconductivity [2–4], ferroelectricity [5,6], ferromagnetism [7, 8], multiferroicity [9] and so on. Also, the techniques used to synthesize these materials and their heterostructures - including molecular beam epitaxy (MBE), pulsed laser deposition (PLD), atomic layer deposition (ALD), stamp transfer, etc. - have been developed due to advances in all aspects, including lasers and vacuum equipment [10]. However, freestanding thin films, which can go beyond these conventional materials and be further applied in flexible electronics and integrated with other types of materials, e.g. 2D transition-metal dichalcogenides [11], have only recently been identified as one of the future directions [12].

In general, complex thin films, especially oxides and their heterostructures, are epitaxially deposited on substrates. These methods allow atomic-scale control of the layer structure, but have unavoidable limitations that can prevent the integration of these thin films with other materials. First of all, heteroepitaxy refers to a growth mode in which grown crystalline layers are in registry with seed layers. This means that only some limited combinations of materials with similar crystal structures, orientations and lattice parameters can be deposited by heteroepitaxy, despite several novel deposition methods such as van der Waals (vdW) epitaxy [13, 14]. Second, epitaxial thin films are usually deposited under extreme conditions, e.g. high temperature and high vacuum, which can hinder their integration with materials that are unstable in these conditions. This can further limit their application in flexible electronics, where thin films often need to be attached to thermodynamically unstable polymers [15, 16]. What's more, high temperature may cause interdiffusion across the interface and hinder the formation of a sharp inter-

face [17, 18]. Last but not least, since epitaxial thin films are clamped by the substrate, their structures and properties are often affected by the strain effect, leading to differences as compared to bulks [19, 20].

On the other hand, benefiting from the weak interlayer bonding, a large number of van der Waals materials, which can be exfoliated into monolayers, are therefore used to fabricate heterostructures [21]. The process is quite simple as compared to thin film deposition and is attracting people to go beyond simple stacking of materials to twisted heterostructures. Focusing on the nontrivial electronic correlations in Moiré lattices, twistronics has attracted broad research interests for the ongoing discoveries of diverse novel physics, such as the emergence of superconductivity, correlated insulating and topological states in magic-angle graphene, and strongly correlated electronic phases and Moiré excitons in transition-metal dichalcogenides [2, 22–25]. Considering spin as another property of electrons, the magnetic twisted lattices can be a promising stage to investigate spin correlations, which would be possible to add a new dimension to twistronics and spintronics [26]. However, most 2D vdW materials are non-ferromagnetic (FM) and some of the known magnetic materials among them have low Curie temperatures, which significantly limits further research and applications [27].

In order to overcome the aforementioned difficulties and limitations, freestanding thin films have recently been extensively studied, bridging the gap between different types of materials. It is now possible to release ultrathin single-crystal films with thicknesses ranging from one unit cell (u.c.) [28] to several tens of nanometers from their substrates and transfer them directly onto various kinds of bases, even at twisted angles [29, 30], bypassing the restrictions of conventional epitaxy. Novel functionalities, including flexible electronics and junctions based on vdW materials and oxide thin films, can be realized in this way [11, 31, 32]. Moreover, freestanding thin films can exhibit different properties when compared to as-deposited thin films, thus providing a new regime for investigating fundamental properties such as flexoelectricity [33,34]. Lastly, the freestanding characteristic also allows correlated oxides to be excellent candidates for magnetic Moiré lattices, whose complexity facilitates the discovery of new phenomena and physics far beyond what can be found in epitaxial bilayers.

Freestanding thin films as a broadly defined field is now rapidly developing. In this thesis, we first show that complex heavy metal/ferromagnetic (HM/FM) heterostructures deposited on a water-soluble oxide $Sr_3Al_2O_6$ (SAO) with a buffer layer of MgO can be detached from their substrate, here a $SrTiO_3$ (STO) substrate, with the magnetics properties largely intact. We then fabricate Hall-bar and racetrack memory (RTM) devices from the freestanding films and demonstrate that they exhibit comparable performance to the as-deposited films. We further realize a 3D RTM device by transferring the HM/FM heterostructures onto a pre-patterned sapphire substrate. We show that chiral domain walls (DWs) of different types can be selectively passed across the protrusions after systematically studying the current-induced DW behavior with varying the protrusion height and geometry, showing significant potential as key components in DW logic devices [35]. We

also realize highly efficient 3D RTM devices designed from freestanding synthetic antiferromagnetic (SAF) films. A similar DW velocity versus current density curve compared to the 2D as-deposited thin films is observed in 3D SAF RTM devices with protrusions up to ~ 900 nm high. Furthermore, by removing the MgO buffer layer, we show that SAO itself acts as a good buffer to obtain HM/FM heterostructures with a perpendicular magnetic anisotropy (PMA). Freestanding RTM devices can be obtained without any buffer layer, which facilitates further combinations with magnetic or ferroelectric bases. In the second use of our water membrane technique, we choose the well-known half-metallic ferromagnetic $La_xSr_{1-x}MnO_3$ ($x = 0.67$) (LSMO) to fabricate twisted bilayers by transferring a freestanding LSMO layer onto an as-deposited LSMO layer. We observe anomalous diamagnetic behavior in magnetic hysteresis of the twisted bilayers and anomalous magnetoresistance responses to magnetic field in the twisted bilayers, indicating diamagnetic behavior. This diamagnetic behavior is then attributed to the formation of spin textures with interlayer and intralayer antiferromagnetic coupling.

This thesis is organized as follows: Chapter 2 gives a background on freestanding thin films, including their synthesis, transfer and functionalities, and ends with an introduction of the methods presented in this thesis; Chapter 3 focuses mainly on the background of magnetic DWs and their motions; Chapter 4 introduces the experimental methods and setups used in this thesis; Chapter 5 discusses magnetic and transport properties in freestanding PMA samples together with current-induced domain wall motion (CIDWM) results in these samples; Chapter 6 shows CIDWM results in 3D racetracks formed from freestanding HM/FM and SAF samples; Chapter 7 discusses results of freestanding HM/FM layers without any buffer layers; Chapter 8 shows the anomalous magnetic signals in twisted LSMO bilayers; finally, Chapter 9 presents a conclusion and outlook based on the current state-of-the-art.

Chapter 2

Freestanding thin films

In this chapter, we will introduce the background of the freestanding thin films, starting from a brief review of previous studies on freestanding techniques and their applications. Then, the perovskite-like water-soluble $(Ca, Sr, Ba)_3Al_2O_6$, which is usually utilized as a sacrificial buffer to obtain freestanding thin films, will be introduced. Finally, the method developed by the author to obtain large size oxides sheets will be introduced.

2.1 Previous studies of freestanding techniques

2.1.1 Physical lift-off process

Various kinds of physical lift-off processes have been developed to obtain freestanding thin films including laser lift-off, vdW epitaxy assisted mechanical lift-off and substrate thinning, as shown in Fig. 2.1. From more than 20 years ago, freestanding thin films have already been achieved by laser [36]. Ferroelectric $(Pb, La)(Zr, Ti)O_3$ (PLZT) films were transferred to stainless steel after irradiation with a single excimer laser pulse through their substrates (Fig. 2.1 a). However, the structure of the bottom surface can be destroyed by laser irradiation, which means that only relatively thick films can be transferred through this method (the film thickness in this study was 1.4 μm). Also, a rough bottom surface can impede the coupling between the freestanding thin film and the transferred bases. Alternatively, as schematically illustrated in Fig. 2.1 b, ion etching is applicable to reduce the thickness of substrates to achieve freestanding, e.g. a freestanding $Pb_{1.1}Zr_{0.48}Ti_{0.52}O_3$ film with flexibility was obtained after deep reactive ion etching while the structure remained undamaged [37]. This method has a similar disadvantage to the first method: the quality of the bottom surface cannot be guaranteed. In addition, the thinning process is often laborious.

Very recently, with insights from mechanical exfoliation of 2D vdW materials, vdW epitaxy assisted mechanical lift-off has also been demonstrated to fabricate freestanding films (Fig. 2.1 c). First, the deposition of well-ordered epitaxial thin films on 2D layered materials can be realized even for dissimilar crystalline structures [38–40]. Distinct from conventional heteroepitaxy, where strong chemical bonds determine the lattice structure

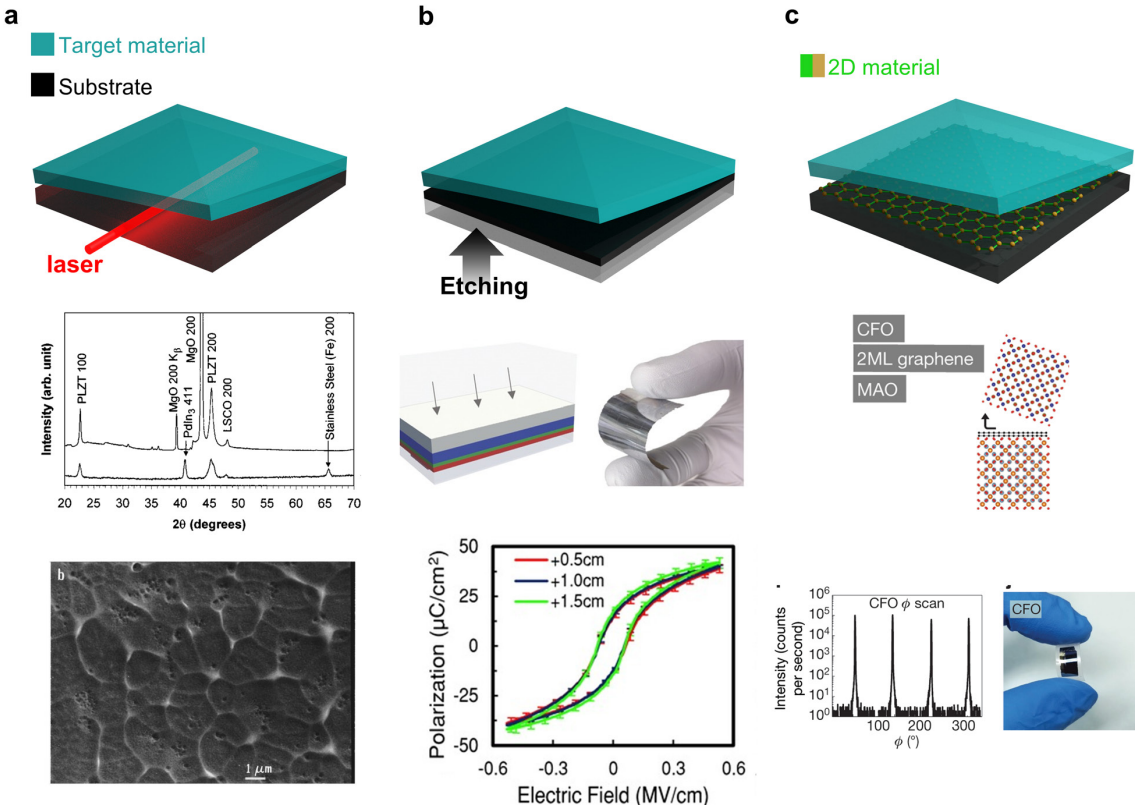

Figure 2.1: Physical freestanding techniques. **a,** Laser lift-off. θ–2θ XRD patterns show that PLZT films are successfully detached from the substrate. Scanning electron microscopy images show the PLZT film surface after the process. Figures are adopted from Ref. [36]. **b,** Substrate thinning. By deep reactive ion etching from the backside, flexible freestanding ferroelectric samples are realized on the stainless steel. Figures are adopted from Ref. [37]. **c,** VdW epitaxy assisted mechanical lift-off. Single crystal freestanding CFO is obtained by exfoliation after deposition on bilayer graphene. Figures are adopted from Ref. [14].

and orientation of the deposited thin films, vdW epitaxy involves the formation of weak bonds between the film and the substrate, thus allowing the deposition and exfoliation of epitaxial thin films. For instance, Kum et al. [14] obtained freestanding membranes of perovskite $BaTiO_3$ (BTO), spinel $CoFe_2O_4$ (CFO) and garnet $Y_3Fe_5O_{12}$, after remote epitaxial deposition of them on different substrates coated with bilayer graphene. Although a clean interface can be obtained through this simple and universal lift-off method, it is difficult to obtain large-area homogeneous freestanding films because the quality of 2D buffer layers can greatly affect the property of the top layers. This may obstruct its further application in device fabrication.

2.1.2 Chemical lift-off process

To avoid the aforementioned problems, people have developed chemical lift-off processes as well. The earliest preparation of freestanding thin films was realized by Konagi et al. in 1978 [41]. They fabricated a freestanding n-GaAs film by selective etching a $Ga_{0.3}Al_{0.7}As$ buffer in hydrofluoric acid. After 45 years of development, chemical exfoliation is now one of the main methods for producing freestanding thin films. In contrast to physical lift-off processes, where various strategies are used to remove substrates, chemical exfoliation mainly involves selective etching processes to remove substrates or sacrificial layers, which is simpler and usually more efficient (Fig. 2.2) [42–44].

Among the chemical lift-off processes, the most straightforward one, i.e. etching substrates, was first developed at a similar time to the invention of physical laser lift-off. Gan et al. [42] reported a freestanding $SrRuO_3$ (SRO) thin film by etching the $SrTiO_3$ (STO) substrates in strong acid (50% HF:70% HNO_3:H_2O = 1:1:1), as shown in Fig. 2.2 a. X-ray diffraction (XRD) confirmed that the freestanding SRO is strain-free. This relaxation of lattice resulted in an increase in the Curie temperature. However, it is cumbersome to completely etch the substrate or etch enough to release the target materials, and expensive single crystal substrates cannot be reused after this process. To improve this process, Paskiewicz et al. [43] used photolithography process to create homogeneously distributed holes in the SRO (Fig. 2.2 b). Then, the etching process can be greatly accelerated and substrates can be reused after post treatments. Besides, the etching rate can be increased by improving the etching selectivity, e.g., NaCl crystal with high surface finish was selected as the substrate due to its high solubility in water [45]. The freestanding metal-insulator-metal structure Pt/WO_x/Ti was fabricated by this process, but the substrate is sensitive to humidity and requires special care during deposition. In short, only limited etchants can be used to etch substrates, which means only limited freestanding thin films can be obtained.

To improve the quality and expand the family of freestanding thin films, researchers have turned to sacrificial layers that are inserted between substrates and target thin film materials. For example, Bakaul et al. [44] showed that $Pb(Zr_{0.2}Ti_{0.8})O_3$ (PZT) films, $(CaTiO_3/SrTiO_3)_6$ superlattices, and SRO/$BiFeO_3$ (BFO)/CoFeB/Pt multilayers were released and subsequently transferred onto Si wafers after selective etching of a 20 nm thick

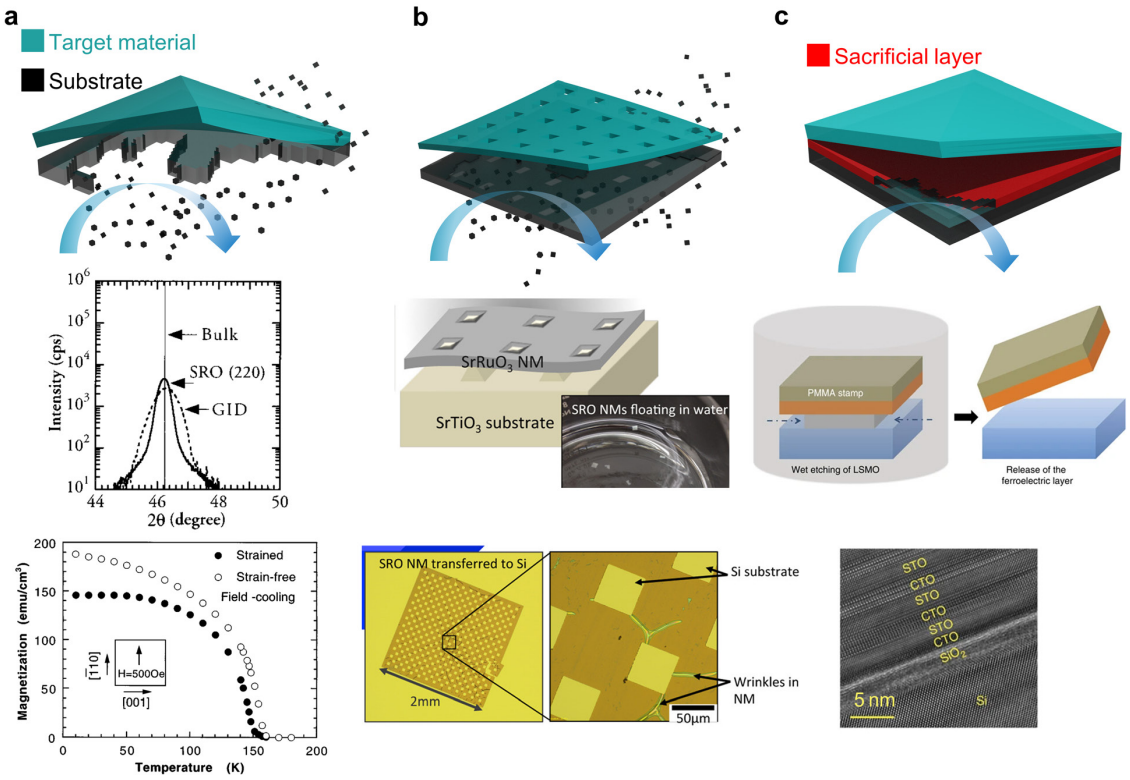

Figure 2.2: Chemical freestanding techniques. **a,** Etching substrates. θ–2θ XRD patterns and magnetization to temperature curves show that freestanding ferromagnetic SRO is successfully obtained. Figures are adopted from Ref. [42]. **b,** Etching substrates from the top. After patterning the target thin film SRO with photolithography, the etching process can be accelerated and freestanding SRO thin films are transferred onto Si wafers. Figures are adopted from Ref. [43]. **c,** Etching sacrificial layers. Freestanding oxide heterostructures are released from substrates after wet etching of LSMO sacrificial buffer. Figures are adopted from Ref. [44].

sacrificial LSMO ($x = 0.7$) in the aqueous solution: $KI + HCl + H_2O$ (Fig. 2.2 c). As shown in this work, thin oxide films down to one unit cell (4 Å) can be transferred, as well as silicon-on-insulator transistors can be fabricated from freestanding PZT transferred onto silicon. After rapid development in these years, etching of sacrificial layers has proven to be an affordable, convenient and fast method. This technique offers tremendous flexibility due to the discovery of various sacrificial buffer materials, as summarized in Table 2.1. For example, perovskite oxides such as LSMO [44, 46–51], SRO [52–54], $SrCoO_{2.5}$ (SCO) [55] have also been used as sacrificial buffers. A major advantage of these perovskites is that they usually have a similar structure to the target material, which can be helpful in maintaining in-plane (IP) orientation and forming single crystal thin films. Furthermore, the properties of different perovskites make them suitable for different etchants. For example, $NaIO_4$ solution can be used to dissolve SRO since RuO_2 can be oxidized to volatile RuO_4 while SCO can be dissolved in weak acetic acid. In addition to perovskites, metal oxides have been demonstrated as sacrificial layers, e.g. BaO [56, 57], MgO [58, 59], AlO_x [60, 61], ZnO [62, 63] and VO_2 [64]. Metals such as copper can also be used to obtain freestanding layers [34]. The limitation of small lattice mismatch, which is required to obtain epitaxial freestanding thin films, is overcome by selecting the appropriate materials.

Table 2.1: Sacrificial layers in literature. Various types of sacrificial buffers are listed in this table with their synthesis methods, crystallinity, removals, and target materials.

Sacrificial layer	Preparation method	Crystallinity (bilayer)	Removal	Target Materials
$SrTiO_3$ (Top substrate)	-	Single crystal	HF + HNO_3 + H_2O	$SrRuO_3$ (SRO) [43]
$La_{1-x}Sr_xMnO_3$	PLD	Single crystal	KI + HCl solution	$LiFe_5O_8$ [46], $PbZr_xTi_{1-x}O_3$ (PZT) [47, 48], $Ba_{1-x}Sr_xTiO_3$ [49, 50], (SRO/PZT/SRO), $(CaTiO_3/SrTiO_3\,(STO))_6$ [44, 51, 65]
$SrRuO_3$	PLD	Single crystal	$NaIO_4$ solution	$La_{0.7}Sr_{0.3}MnO_3$ [52], $LaAlO_3$ (LAO)/STO [53, 54],
$Sr_3Al_2O_6$	PLD/MBE	Single crystal	H_2O	$La_{0.7}Sr_{0.3}MnO_3$ [66],$SrTiO_3$ [67], $PbTiO_3$ [68], $BaTiO_3$ [69], VO_2 (amorphous) [70], Fe_3O_4 [71], $YBa_2Cu_3O_{7-x}$ [72], etc.
$Ba_3Al_2O_6$	PLD	Single crystal	H_2O	La:$BaSnO_3$ [73]
$SrCoO_{2.5}$	PLD	Single crystal	Vinegar, 36% CH_3COOH, carbonated drinks	$SrRuO_3$ [55]
$SrVO_3$	PLD	Single crystal	H_2O	$SrTiO_3$ [74]
$YBa_2Cu_3O_7$	PLD	Single crystal	HCl (0.6%)	$SrRuO_3$ [75], $La_{0.7}Sr_{0.3}MnO_3$ [75, 76]
BaO	PLD	Single-/polycrystal or amorphous	H_2O	$BaTiO_3$ (STO buffer) [56], $SrRuO_3$, FeSe (polycrystal/amorphous) [57]
MgO	PLD	Single crystal	$(NH_4)_2SO_4$ (10%)	$CoFe_2O_4$ [58, 59],
AlO_x	PLD	Amorphous	NaOH solution	(SRO/PZT/SRO/YSZ) [60], $LaAlO_3$ [61]
ZnO	Sputtering/PLD	Single crystal	HCl solution	VO_2 [62], GaN (MOVPE) [63]
VO_2	PLD	Single crystal	H_2O_2 solution	TiO_2 [64]
AlO_x/Al	PLD/EB evaporation	Amorphous/poly	Dilute KOH	$SrRuO_3$ [57]
Cu	Sputtering	Polycrystal	HNO_3	Pt [77]
In-Zn-O	Spincoating	Amorphous	H_3PO_4	PZT [78]
Photoresist	Spincoating	Amorphous	Dimethyl carbonate	LiPON [79]

2.2 Properties and applications of freestanding thin films

2.2.1 Physical properties of freestanding thin films

The fascinating physical properties and the great potential to create heterostructures with various kinds of materials are critical for both fundamental research and applications of freestanding thin films. In this section, representative properties such as ferroelectricity,

ferromagnetism, superconductivity, flexoelectricity, phase transition and strain effect on these properties will be briefly introduced with seminal works as examples.

Ferroelectricity

Materials with ferroelectricity have spontaneous polarization that can be switched by an external electric field. L. Han et al. [68] synthesized freestanding $PbTiO_3$ (PTO) thin films by dissolving SAO, while both layers were deposited by MBE. Ferroelectricity of freestanding PTO thin films down to 4 u.c. (transferred onto Si wafer coated with Au) was confirmed by piezoresponse force microscope (PFM) (Fig. 2.3 a-b). Also, the downward self-polarization disappears in the ultrathin sample (Fig. 2.3 b), which is originated from the drastic reduction of the tetragonality, this is, the *c/a* ratio, shown in the XRD results of freestanding thin films with different thicknesses ranging from 4 u.c. to 60 u.c. (Fig. 2.3 c-d). Besides, these freestanding thin films provide an excellent platform for continuous strain tuning. After transferring the freestanding sample onto poly(ethylene terephthalate) (PET), continuous uniaxial tensile strain of up to 6.4% was applied to these samples (Fig. 2.3 e). This value is much higher than what can be achieved in an as-deposited sample [80]. IP domain writing was realized with tensile strain (Fig. 2.3 f). This group then continued their research in freestanding PTO/STO bilayers [81]. Switchable skyrmion-like polar nanodomains, which had only been observed in as-deposited samples, were integrated on silicon (Fig. 2.3 g). As shown in Fig. 2.3 h, freestanding BaTiO3 (BTO) membranes were also obtained by removing SAO, as reported by G. Dong et al [69]. Out-of-plane (OOP) PFM measurements show the ferroelectricity of the transferred sample (Fig. 2.3 i). Interestingly, superelasticity was found in this freestanding thin film. Freestanding BTO films can withstand bending up to 180° and recover their original state, as demonstrated by in-situ bending in scanning electron microscopy (SEM) (Fig. 2.3 j). This is mainly due to the existence of dynamic evolution of ferroelectric nanodomains. Recoverable strain could reach $\sim 10\%$, as also proved by atomistic simulations. This group then used this technique to build periodic wrinkled membranes with freestanding BTO on poly(dimethylsiloxane) (PDMS) [82]. Regions with different types of strain exhibited different polarizations, i.e. OOP and IP polarization dominate compressive and tensile regions, respectively (Fig. 2.3 k). Zigzag textures can also be obtained by this method [83]. Freestanding ferroelectric thin films show large flexibility and strong correlation with strain, potentially enabling their use in next-generation flexible electronic devices.

Ferromagnetism

Ferromagnetism is a property of materials with electrons in unfilled shells and show an observable moment in the absence of external magnetic field. LSMO is one of the most famous ferromagnetic oxides due to its high Curie temperature, intrinsic magnetoresistance properties, strain controlled magnetic anisotropy and half-metallicity [84, 85]. As

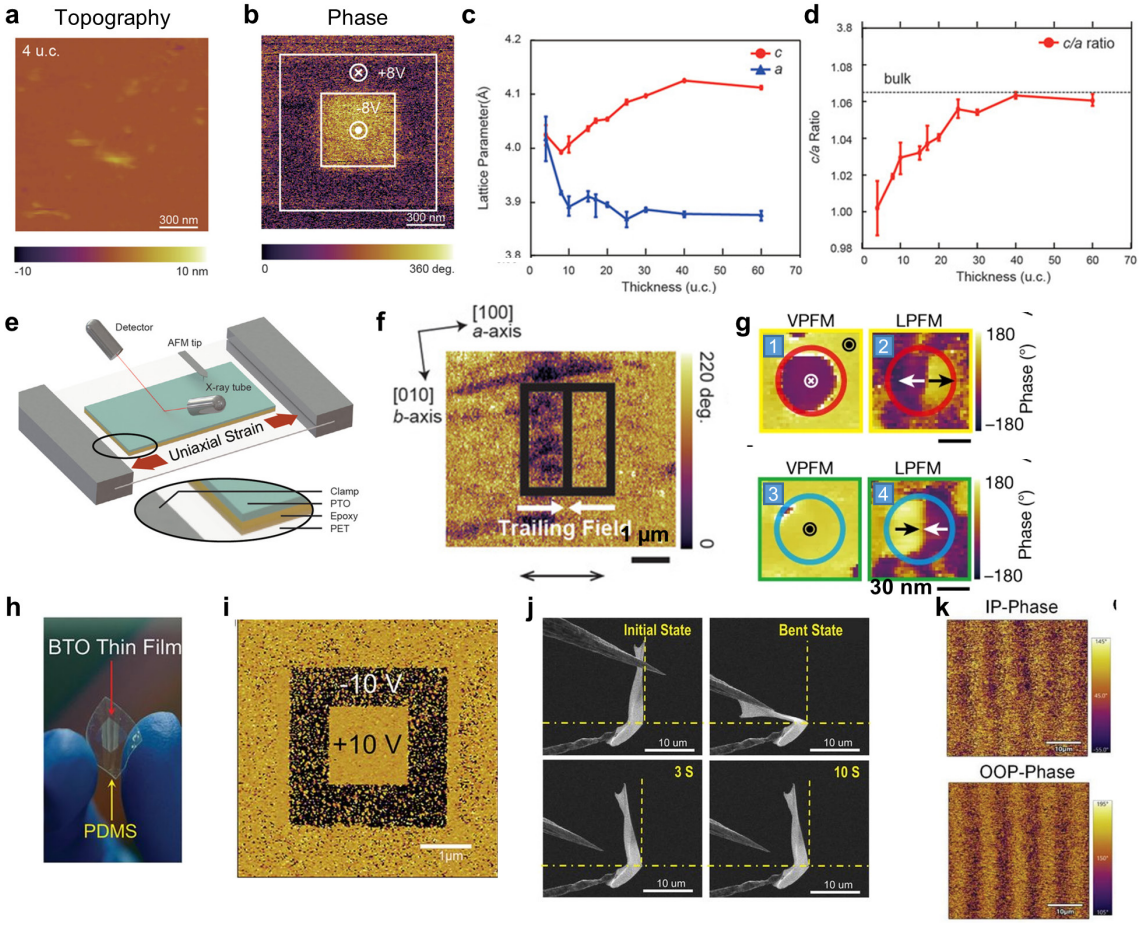

Figure 2.3: Ferroelectricity in freestanding thin films. **a,b,** The surface morphology (**a**) and the out-of-plane PFM phase image (**b**) of a 4 u.c. freestanding PTO film. **c,d,** Evolution of both *c* and *a* lattice constants (**c**) and *c/a* ratio (**d**) with the film thickness. **e,** Design of the stage used for applying tensile strain. **f,** In-plane domain switching via trailing field. Scale bar, 1 μm. (**a**-**f**) are adopted from Ref. [68]. **g,** Zoomed-in vertical (1 and 3) and lateral (2 and 4) PFM images for center-divergent domain (top) and center-convergent domain (bottom). This figure is adopted from Ref. [81]. **h,** A photograph of the freestanding BTO thin film transferred onto PDMS. **i,** Out-of-plane PFM phase image of BTO transferred on Pt/Si. **j,** SEM images of in situ bending of a BTO sheet (20 μm × 4 μm × 60 nm) (**h**-**j**) are adopted from Ref. [69]. **k,** PFM images of wrinkled BTO. Figure is adopted from Ref. [82].

illustrated in Fig. 2.4 a, LSMO has an ABO_3 perovskite structure with a Mn ion at the center and La/Sr ions at the corner of the unit cell. A MnO_6 octahedron consists of the Mn ion surrounded by six oxygen ions. This octahedron can be modified by varying the dopant concentration and tuning the strain, resulting in changes in electronic properties. Therefore, obtaining freestanding LSMO is crucial for the application of freestanding thin films. Many groups have recently fabricated freestanding LSMO thin films using different sacrificial layers, including SRO and SAO [52, 66]. D. Lu et al. [66] first prepared freestanding LSMO and LSMO/STO superlattices by dissolving a water-soluble SAO layer (Fig. 2.4 b). Compared with the as-deposited thin film, the magnetic properties were well remained or even enhanced after transfer. The Curie temperature was slightly higher and the residual resistivity was lower, as shown in Fig. 2.4 c. More strikingly, this tendency is much clearer in superlattice samples: the resistivity peak, which is often observed in superlattice [86], increased by ~ 40 K. Similar enhancement was found in other orientations of freestanding LSMO thin films by Z. Lu et al. [87]. Different oriented freestanding LSMO thin films show clear strain relaxation as the XRD peaks shift to the left compared to the as-deposited thin films and become closer to the bulk value, while all the freestanding and strained films show room temperature ferromagnetism and the Curie temperature of all cases was increased after lift-off (Fig. 2.4 d). This enhancement can be attributed to strain relaxation after the transfer process, as the Mn-O-Mn bonding can be affected by strain [88, 89]. H. Wang et al. [90] further investigated the effect of strain on the magnetic properties of freestanding LSMO transferred onto PDMS bases, which ensure uniform bending. They first confirmed that the ferromagnetic resonance (FMR) spectrum of the transferred films was similar to that of the as-deposited thin films, both exhibiting a typical modified Dysonian line shape (Fig. 2.4 e). The bending axis was set along the [010] direction of the LSMO films, and then FMR spectra were obtained for freestanding films under different bending radii. When the field angle is close to 90°, the resonance field (H_r) of all thin films, bending or unbent, approaches the same maximum. At a relatively higher field angle ($> 40°$), H_r decreases with reducing bending radii. The experimental results show a good agreement with the modelling results based on the misorientation effect, suggesting that this effect is crucial during bending processes (Fig. 2.4 f). Small differences between theoretical and experimental results may result from inhomogeneity in the films. As shown in Fig. 2.4 g, continuous tuning of H_r can be realized by bending with the magnetic field applied in a moderate direction (73°). The integration of both invariable and tunable microwave magnetisms in a single LSMO thin film was realized in freestanding flexible sheets, as demonstrated in this work. In addition, the magnetism of many other freestanding thin films has also been investigated: modulated magnetic anisotropy was discovered in freestanding SRO [55], and controllable enhanced magnetic properties similar to those in freestanding LSMO was found in freestanding $Ni_{0.5}Zn_{0.5}Fe_2O_4$ ferrite membranes [91]. Developing freestanding magnetic thin films can potentially boost spintronic applications.

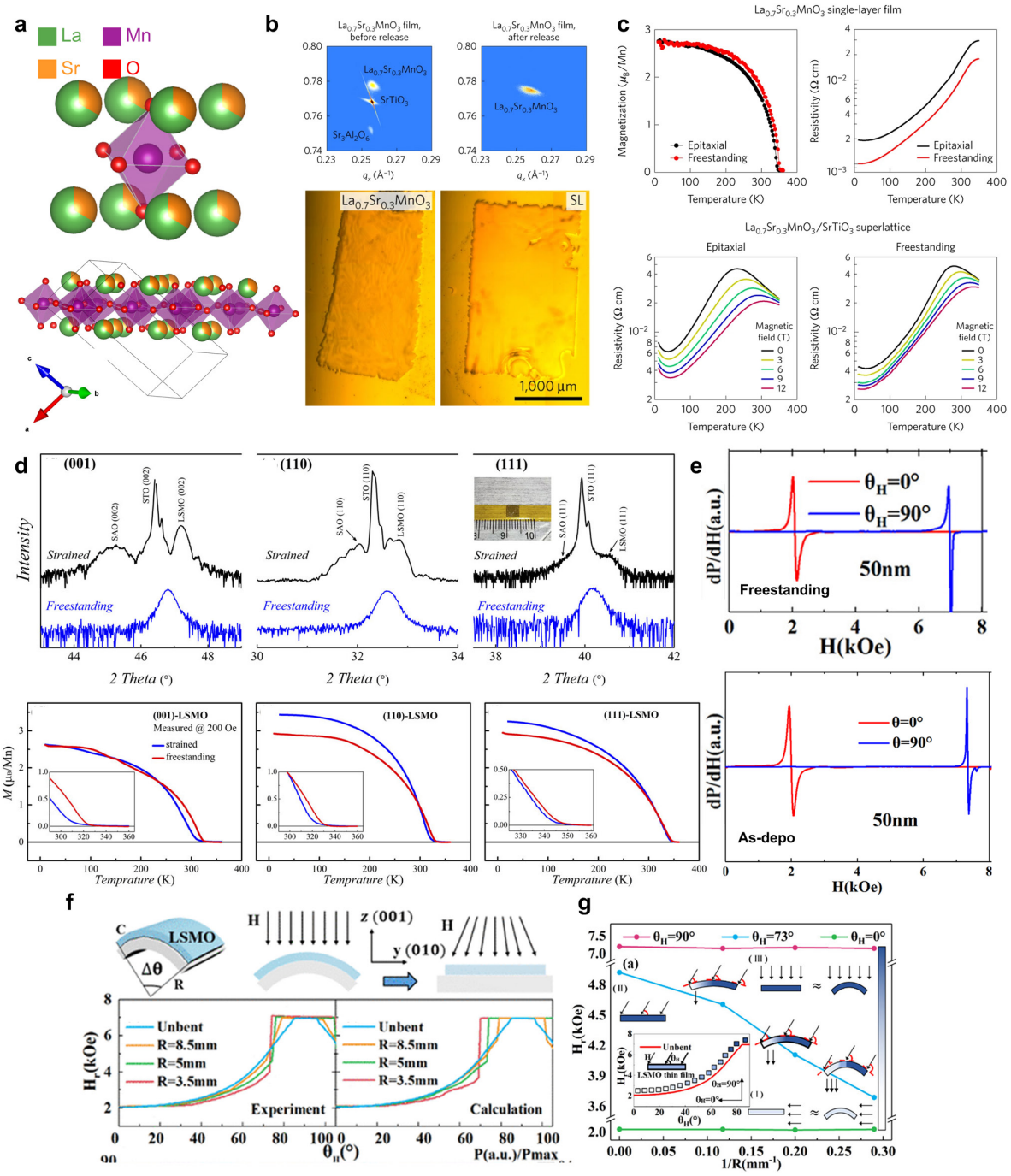

Figure 2.4: Ferromagnetism in freestanding thin films. **a,** Crystal structure of LSMO. **b,** Reciprocal space mapping images of LSMO before (top-left) and after (top-right) transfer, and photos of freestanding LSMO and STO/LSMO superlattice. **c,** Magnetic and transport properties of freestanding and epitaxial LSMO. (**a**-**c**) are adopted from Ref. [66]. **d,** Out-of-plane XRD patterns (top) and *M*-*T* curves (bottom) of freestanding and as-deposited LSMO thin films with different orientations. Figures are adopted from Ref. [87]. **e,** FMR spectra of the LSMO thin films before (top) and after (bottom) transfer. **f,** Bending tuned FMR: schematic illustration (top) and experimental (bottom-left) and calculated (bottom-right) field angle dependent H_r curves. **g,** H_r for the freestanding LSMO thin film under different bending. (**e**-**g**) are adopted from Ref. [90].

Superconductivity

Cuprate superconductors are a big family of high-temperature superconducting materials consisting of layers of copper oxides and other metal oxides. After the discovery of the first cuprate superconductor in 1986 in the Ba-La-Cu-O system [3], various kinds of superconductors with different critical temperatures (T_c) up to 133 K have been synthesized (Fig. 2.5 a) [92, 93]. Among them, $Bi_2Sr_2CaCu_2O_{8+\delta}$ is interesting because it is exfoliable and thus can be used as a stage to study 2D superconductivity with spectroscopic tools such as angle-resolved photoemission spectroscopy [94]. Long-range order, such as superconductivity, is usually suppressed with reducing dimensions, making the 2D case attractive for many researchers [95]. However, $Bi_2Sr_2CaCu_2O_{8+\delta}$ is unstable because it can react with water and oxygen dopants can be rapidly lost, so it must be treated in a cold and inert environment, making it difficult to obtain thin layers and fabricate heterostructures [94]. On the other hand, freestanding superconducting $YBa_2Cu_3O_{6+\delta}$ (YBCO) may allow easy fabrication of heterostructures and integration with varied bases. Z. Chen et al. [72] first reported freestanding YBCO obtained by dissolving SAO in alkaline solution with an encapsulating epitaxial $LaAlO_3$ (LAO) layer applied as a protective buffer (Fig. 2.5 b). As shown in Fig. 2.5 c, the crystallinity of the freestanding YBCO was confirmed by XRD after transfer, showing that the lattice parameter approached the optimal doped bulk value (11.691 Å) [96]. The resistivity was then confirmed by four-point measurement. The room temperature resistivity is comparable to that of high quality bulks while T_c (90.5 K) is also comparable to that of as-deposited thin films (92.2 K), as shown in Fig. 2.5 d. In addition, they found that the deposition conditions and the thickness of the buffer layer are crucial for the solubility of SAO. Furthermore, Z. Jia et al. [97] removed the LAO buffer and dissolved the YBCO/SAO bilayer in sodium hydroxide solution (pH-13). A similar transport property was found after transfer, with a slight variation of T_c from 90 K to 89.1 K (Fig. 2.5 e). This good quality of freestanding YBCO can be attributed to the formation of a self-passivated layer as confirmed by Raman spectra (Fig. 2.5 f). Interestingly, the freestanding YBCO thin films show different T_c at different bending states. As shown in Fig. 2.5 g-i, T_c was higher for inward bending and conversely was lower for outward bending. Compressive strain released after lift-off may explain this phenomenon. Usually, buffer layers such as STO or LAO have to be deposited to ensure epitaxial growth of YBCO on substrates with large lattice mismatch, e.g. Si [98]. This process can impede its coupling with other materials and its use in 3D devices. Freestanding YBCO is suitable for application in 3D vertical junctions or flexible electronics, and coupling between freestanding YBCO and other materials, e.g. vdW materials, which may allow the discovery of novel functionalities.

Flexoelectricity

Flexoelectricity is a property of all insulators that allows them to polarize under inhomogeneous strain, i.e., it is the coupling between polarization and strain gradient [99]. This

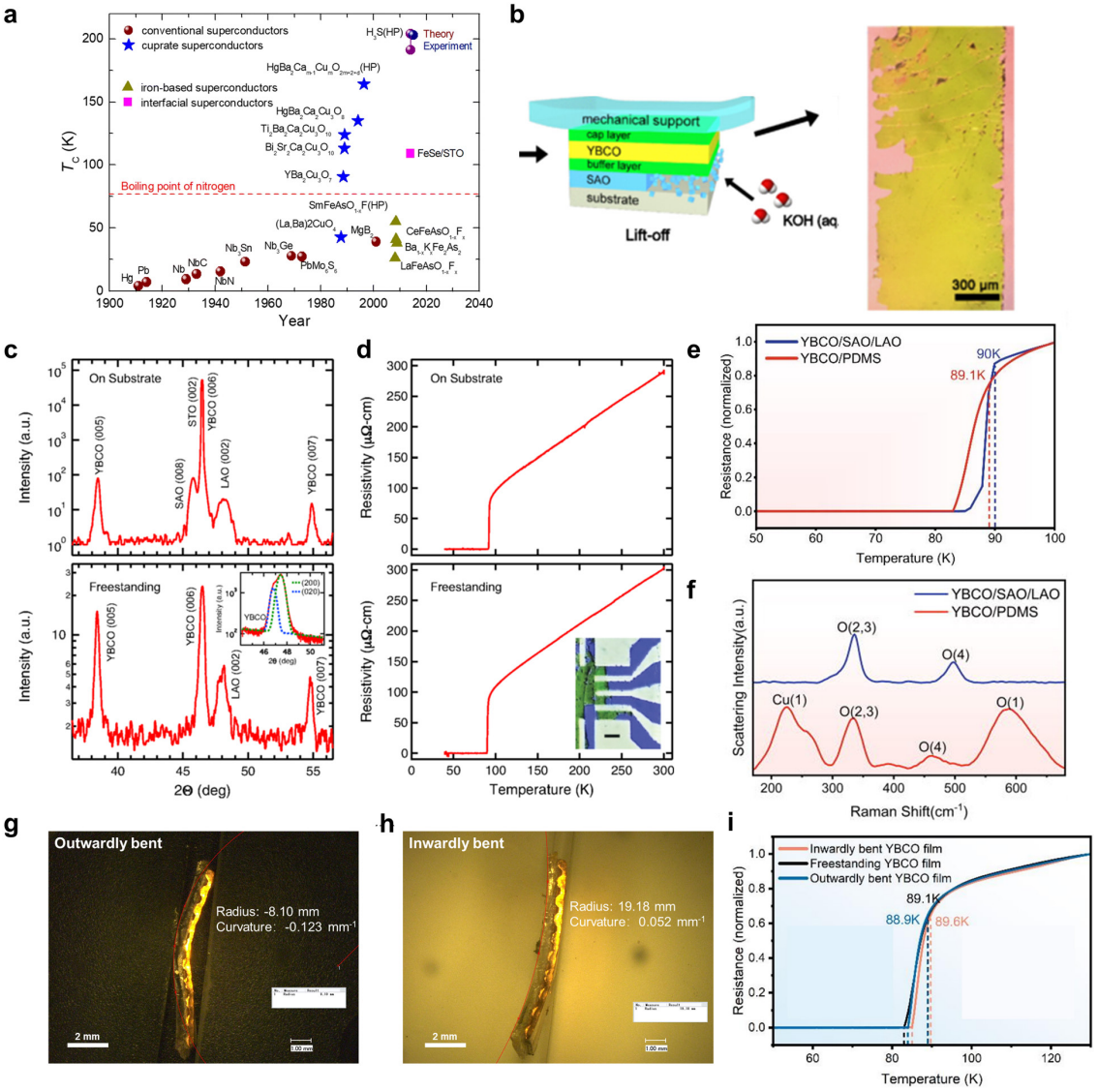

Figure 2.5: Superconductivity in freestanding thin films. **a,** Discovery time and critical temperature of superconductors (adopted from Ref. [92]). **b,** Lift-off and transfer of freestanding YBCO. Right figure is a photo of transferred YBCO. **c,** θ–2θ XRD patterns of YBCO/LAO before (top) and after (bottom) transfer. **d,** Resistivity to temperature curves of as-deposited (top) and freestanding (bottom) YBCO. (**b**-**d**) are adopted from ref [72]. **e,f,** Resistance to temperature curves (**e**) and Raman spectra (**f**) of YBCO before and after transfer. **g**-**h**, Photos show outward (**g**) and inward (**h**) bending of YBCO. **i,** Comparison of the temperature-dependent resistance at different bending states. (**e**-**i**) are adopted from Ref. [97].

concept was first developed in the 1960s [100] and has recently been found to be significantly enhanced by reducing the dimensions [101]. Unlike homogeneous strain, the strain gradient does break the inversion symmetry, allowing centrosymmetric dielectric materials to exhibit electrical response to deformations [102]. This makes flexoelectricity potentially interesting for many applications. However, the strain gradient is usually generated by a localized effect, such as dislocations formed by varying growth conditions or an external force applied via a scanning probe tip [5, 103], and often cannot be continuously varied. Alternatively, freestanding thin films offer a novel platform to introduce a controllable macroscale strain gradient in themselves. R. Guo et al. [33] first reported the continuous control of photoconductance by the flexoelectric effect in freestanding BFO. Flexible BFO with bottom electrode LSMO was transferred onto PDMS and then patterned with Pt, as shown in Fig. 2.6 a. A controllable strain gradient in freestanding BFO can be obtained by continuous bending (Fig. 2.6 b), which can further determine the photocurrent or photovoltage of BFO. Polarization-Volatge (P-V) loops measured under different bending radii show a horizontal right shift with increasing strain, indicating the generation of an effective built-in electric field that can tune the photoconductance of flexible thin films (Fig. 2.6 c). Moreover, both the open-circuit voltage (V_{oc}) and the short-circuit current density (J_{sc}) of the device increase or decrease with the strain gradient when polarization is downward or upward, respectively (Fig. 2.6 d). In addition, the continuous tuning is repeatable and multivalued photovoltage or photocurrent can be obtained after bending up to 300 times, which can be further applied in photovoltaic devices or strain sensors (Fig. 2.6 e). On the other hand, S. Cai et al. [34] investigated the microscopic scale and found a significant change in the thickness of the bent freestanding BFO, which can be attributed to a flexoelectricity-piezoelectricity interplay (Fig. 2.6 f). Also, strain gradients up to 3.5×10^7 m^{-1} were confirmed by atomic-resolution scanning transmission electron microscopy high-angle annular dark-field (STEM-HAADF) measurements (Fig. 2.6 g). This ultra-high (nearly an order of magnitude larger than in the epitaxial films [104]) and uniform strain gradient generated in ultra-thin freestanding thin films provides a new path to obtain large flexoelectric polarization. This unusual property in freestanding thin films may lead to the development of functional devices, such as energy harvesters.

Other properties

In addition to the aforementioned properties, some interesting phenomena and properties have also been observed as well, such as phase transition in thin freestanding thin films [28, 67] and multiferroicity [105]. Zhong et al. [105] fabricated freestanding self-assembled CFO-BTO heteroepitaxial nanostructures, as shown in Fig. 2.7 a. Room temperature multiferroicity was confirmed by PFM and magnetic force microscopy (MFM) measurements (Fig. 2.7 b-c). Flexible multiferroics can be realized in this way. D. Ji et al. [28] observed a strong enhancement of tetragonality in freestanding BFO upon approaching the 2D limit (Fig. 2.7 d). This structural change can lead to a giant polarization

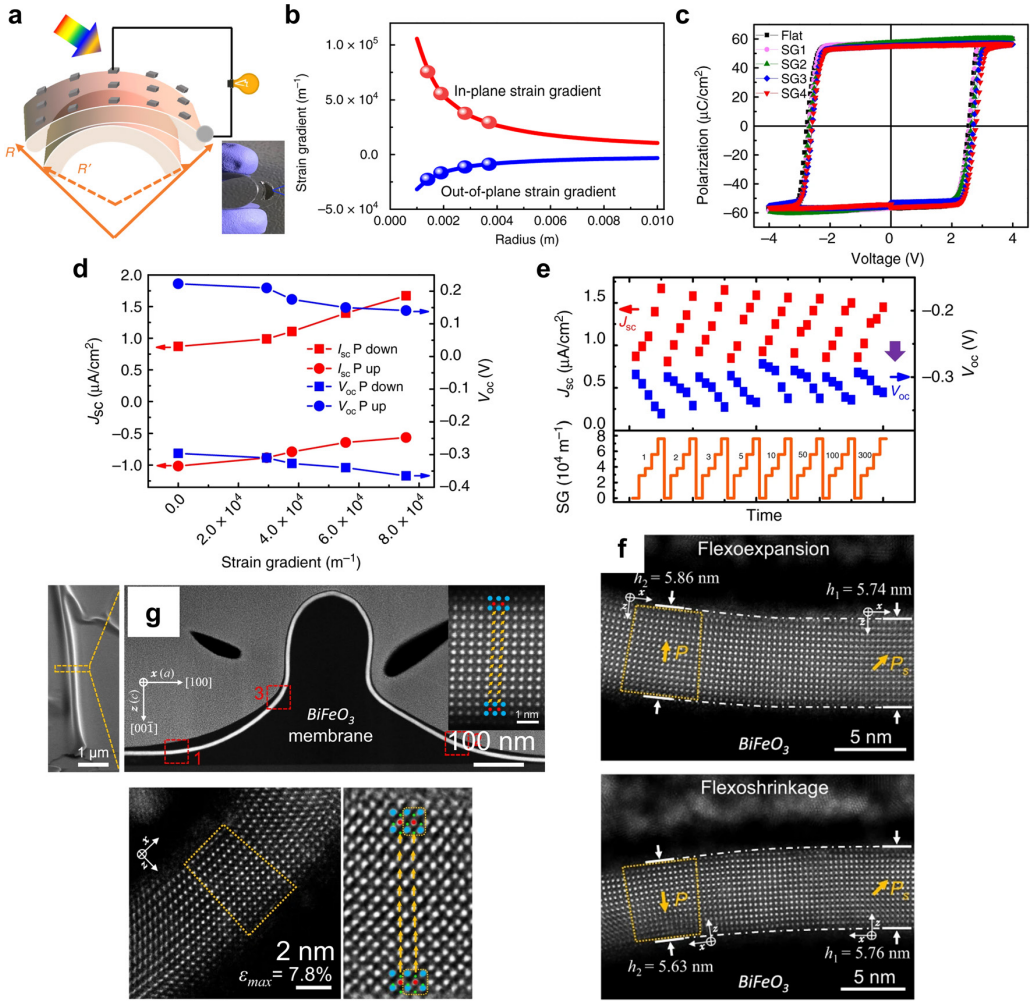

Figure 2.6: Flexoelectricity in freestanding thin films. **a,** Realization of the strain gradient in freestanding BTO by bending. **b,** The strain gradient as a function of the bending curvature. **c,** *P*-*V* loops of the flexible devices at different bending states. **d,** In-plane strain gradient dependent V_{oc} and J_{sc} for both polarizations. **e,** The variation of V_{oc} and J_{sc} as a function of the in-plane strain gradient after different bending cycles. (**a**-**e**) are adopted from Ref. [33]. **f,** The flexoexpansion and flexoshrinkage effects observed in freestanding BFO. **g,** SEM and STEM-HAADF images of wrinkled BFO. The top left is a plan view while others are cross-sectional images. (**f**-**g**) are adopted from Ref. [34].

in freestanding thin films. A similar transition was also observed in freestanding STO by C. Chiu et al. [106]. They confirmed this change by spectroscopic measurements. The broadening and shift of e_g spectral line suggests a lower symmetry, which may result from the off-center displacement of Ti^{4+} in the TiO_6 octahedron (Fig. 2.7 e). In addition, a transition from crystalline to amorphous phase was found in freestanding STO (Fig. 2.7 f) [67]. The transition may be attributed to the breaking of the chemical bond at the 2D freestanding-sacrificial buffer interface, which may define a dimensional limit for some types of freestanding materials.

In summary, freestanding thin films can largely retain the properties of the as-deposited thin films and sometimes show intriguing properties such as enhanced elasticity. In addition, freestanding thin films are able to be easily integrated with various kinds of bases, including flexible organics. Both advantages in preparation and diverse properties are crucial for their application in novel functional devices.

2.2.2 Applications of freestanding thin films

Recently, freestanding thin films have been used in many next-generation electronic and optoelectronic devices due to the rapid development of fabrication methods and the growing family of freestanding materials. This section highlights freestanding thin film based applications, such as memory devices and sensors.

Memories

Ferroelectric materials are used in information storage because of their switchable remnant polarizations. Non-volatile information can be stored by encoding "0" and "1" states into "up" and "down" (or inversely) polarizations. Going beyond ferroelectric random access memory (FeRAM) where a capacitive readout process is involved [107], ferroelectric tunnel junctions (FTJs), in which the readout is realized by measuring the tunnel current, can be fast, low power-consuming and highly scalable. Although FTJs have a simple structure, the growth conditions of ferroelectric materials are usually incompatible with the current Si-based semiconductor industry [108, 109]. To overcome this difficulty, the freestanding technique has been proposed to enable facile integration of ferroelectric materials on Si and flexible bases for next-generation memory devices. D. Lu et al. [110] first fabricated FTJs from freestanding BTO/LSMO/BTO trilayers (Fig. 2.8 a). The resistive switching behavior was confirmed by using a conductive atomic force microscopy (AFM) tip. An on/off ratio of > 100 was achieved, enabling binary logic value storage (Fig. 2.8 b). Good uniformity, repeatability and stability, comparable to devices fabricated from as-deposited epitaxial films, were also confirmed in their devices (Fig. 2.8 c-e). Meanwhile, by transferring freestanding BTO/LSMO bilayer onto flexible bases such as PET, flexible FTJs were fabricated (Fig. 2.8 f) [31]. A clear hysteresis of the resistance was observed by measuring the current with a low voltage applied (reading

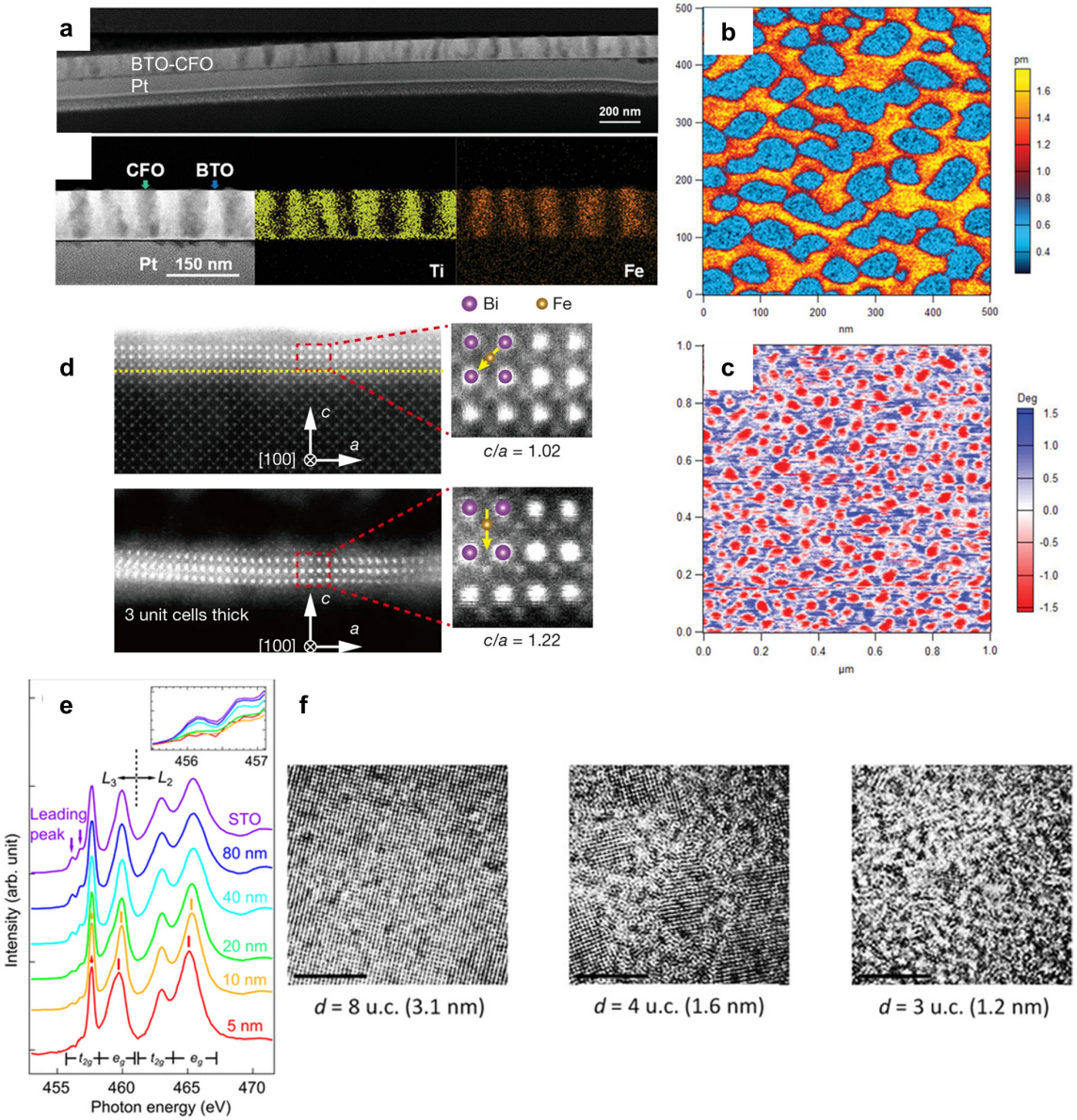

Figure 2.7: Other properties in freestanding thin films. **a,** Cross-sectional STEM images and element mapping of freestanding BTO-CFO. **b,c,** PFM amplitude (**b**) and MFM magnetic phase (**c**) images of freestanding BTO-CFO. (**a**-**c**) are adopted from Ref. [105]. **d,** Cross-sectional HAADF images of a 3 u.c. BFO film before (top) and after (bottom) transfer. Figures adopted from Ref. [28]. **e,** Ti $L_{2,3}$-edge X-ray absorption spectra of STO substrate and freestanding STO of different thicknesses (adopted from Ref. [106]). **f,** TEM images of STO membranes of different thicknesses. Figures are adopted from Ref. [67].

voltage: 200 mV), indicating memristive properties (Fig. 2.8 g). Moreover, they found that multivalued states can be realized by a series of voltage pulses (Fig. 2.8 h). This type of modulation can be used in non-von Neumann computing, such as neuromorphic computing [111].

In addition, flexible FeRAM devices based on thin PZT capacitors were fabricated on Si wafers after thinning substrates by a deep reactive ion etching [37]. Ferroelectricity was confirmed at different bending radii (Fig. 2.8 i). The retention of the devices was also tested after 1300 bending cycles at minimum bending (Fig. 2.8 j). Some other materials, such as WO_x, can also be applied in memristive devices. A flexible artificial memristive synapse was fabricated from freestanding WO_x after dissolving the NaCl substrate (Fig. 2.8 k) [45]. Stable memristive behavior without obvious degradation was confirmed at different bending states (Fig. 2.8 l). In short, these studies suggest a viable route towards non-volatile memories integrated with industrial semiconductors, i.e. Si-based devices, and flexible platforms, based on freestanding thin films.

Sensors

Due to the rapid development of information and communication technology (ICT), lightweight and wearable sensors have attracted much attention because they can be used to collect and transmit information, for example, in healthcare applications [112]. X. Li et al. [62] reported a flexible and sensitive sensor based on freestanding wafer-scale VO_2 membranes (Fig. 2.9 a). Since the resistivity of VO_2 is very sensitive to strain [113], it can be applied as a strain sensor. After transferring the freestanding VO_2 membranes onto PET bases, typical current-voltage (I-V) curves were measured under different strains (Fig. 2.9 b). Large changes in resistivity were confirmed. The freestanding VO_2 was then used to fabricate nanosensors to monitor the radial artery pulse (Fig. 2.9 c). The percussion wave and tidal wave shown in Fig. 2.9 c showed reproducible oscillations and a significant difference before and after the test subjects' exercise, suggesting that the freestanding VO_2 can be an ideal candidate for fabricating sensitive sensors. J. H. Han et al. [114] built a flexible piezoelectric acoustic sensor based on freestanding PZT thin films (Fig. 2.9 d). The freestanding thin films were lifted off using a laser-assisted method. Owing to the good piezoelectric property, the sensitivity of the resonant electrical output enables the acquisition of abundant and intrinsic voice information, which can be further applied to speaker identification. A standard dataset (40 people, 3080 voice data) was used for training and testing the recognition algorithm. Among the datasets, the 2800 data were used for training and the rest were used for testing. A speaker recognition rate of 97.5 % can be achieved, which is much higher compared to the micro-electromechanical systems microphone (Fig. 2.9 e). Moreover, this self-powered sensor has advantages in always-on and low energy consumption ICT applications compared to commercial condenser acoustic sensors that require external power to read capacitance. In addition, K. Song et al. [115] reported a light detection sensor based on freestanding BTO (Fig. 2.9 f). Transparent indium tin oxide was chosen as the top electrode. Light-induced heat

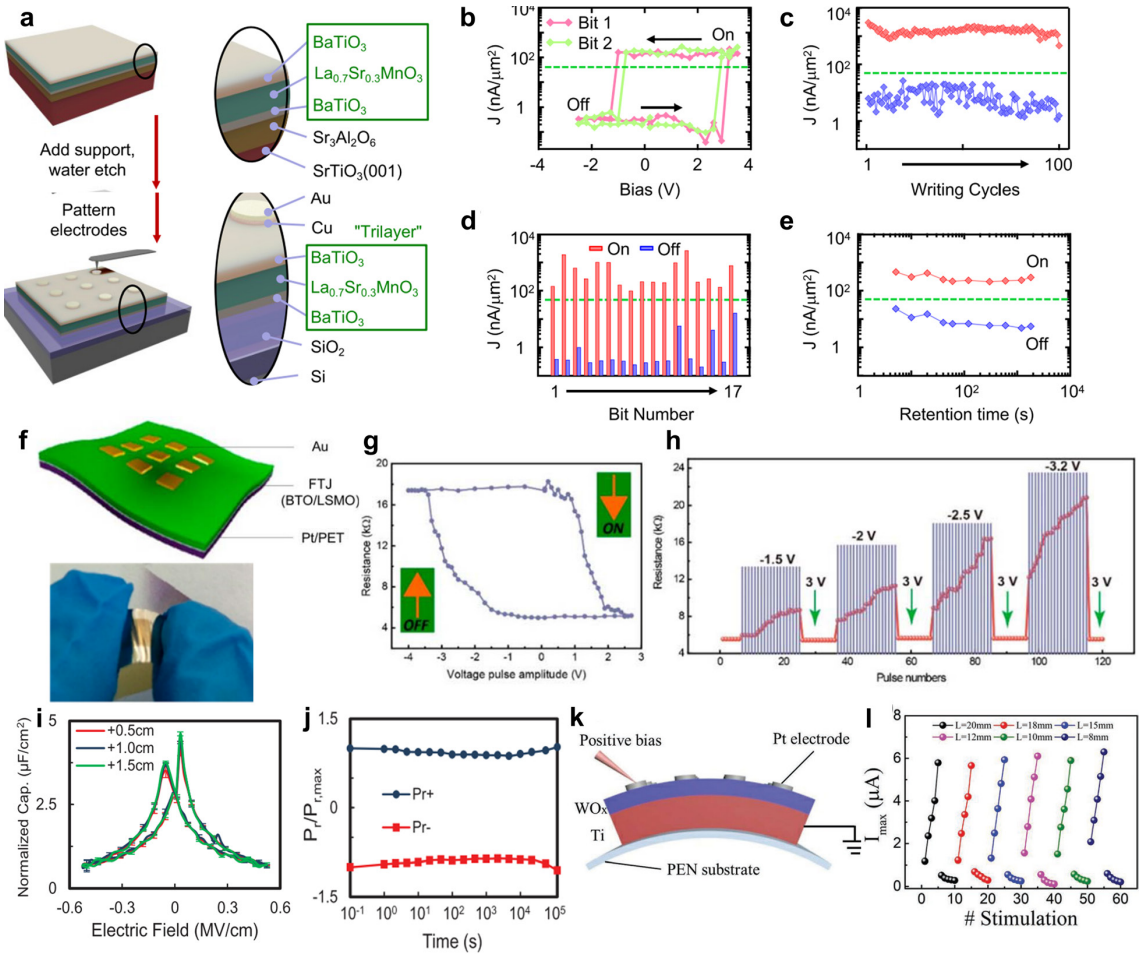

Figure 2.8: Memory devices based on freestanding thin films. **a,** Fabrication of FTJs from freestanding BTO/LSMO/BTO heterostructures. **b**-**e**, Resistive switching behavior of the freestanding FTJs. (**a**-**e**) are adopted from Ref. [110]. **f,** Flexible FTJs based on freestanding BTO/LSMO. **g,** Resistance as a function of operating voltage pulses. **h,** Device resistance state modulated by multiple 0.5-μs-long SET voltage pulses. (**f**-**h**) are adopted from Ref. [31]. **i,** Capacitance to electric field curves at different bending radii. **j,** Representative retention polarization plot of a device after 1300 bending cycles. (**i**-**j**) are adopted from Ref. [37]. **k,** Flexible memrisitive synapse based on freestanding WO_x. **l,** The potentiation and depression of the current value at different bending states. (**k**-**l**) are adopted from Ref. [45].

can cause a rapid temperature change of the thin film, which can be converted into an electrical signal by the pyroelectric effect (Fig. 2.9 g). Photodectivity, which represents the response of a photodetector, can be characterized by charge density. A much higher charge density was found in the freestanding detector, which means it is efficient and sensitive (Fig. 2.9 h). This enhancement seems to be a result of slow heat transfer from freestanding thin films to air. To be concluded, various kinds of sensors, which are fabricated from freestanding thin films, can be applied in many different fields, including health care, speaker recognition, light detection, etc.

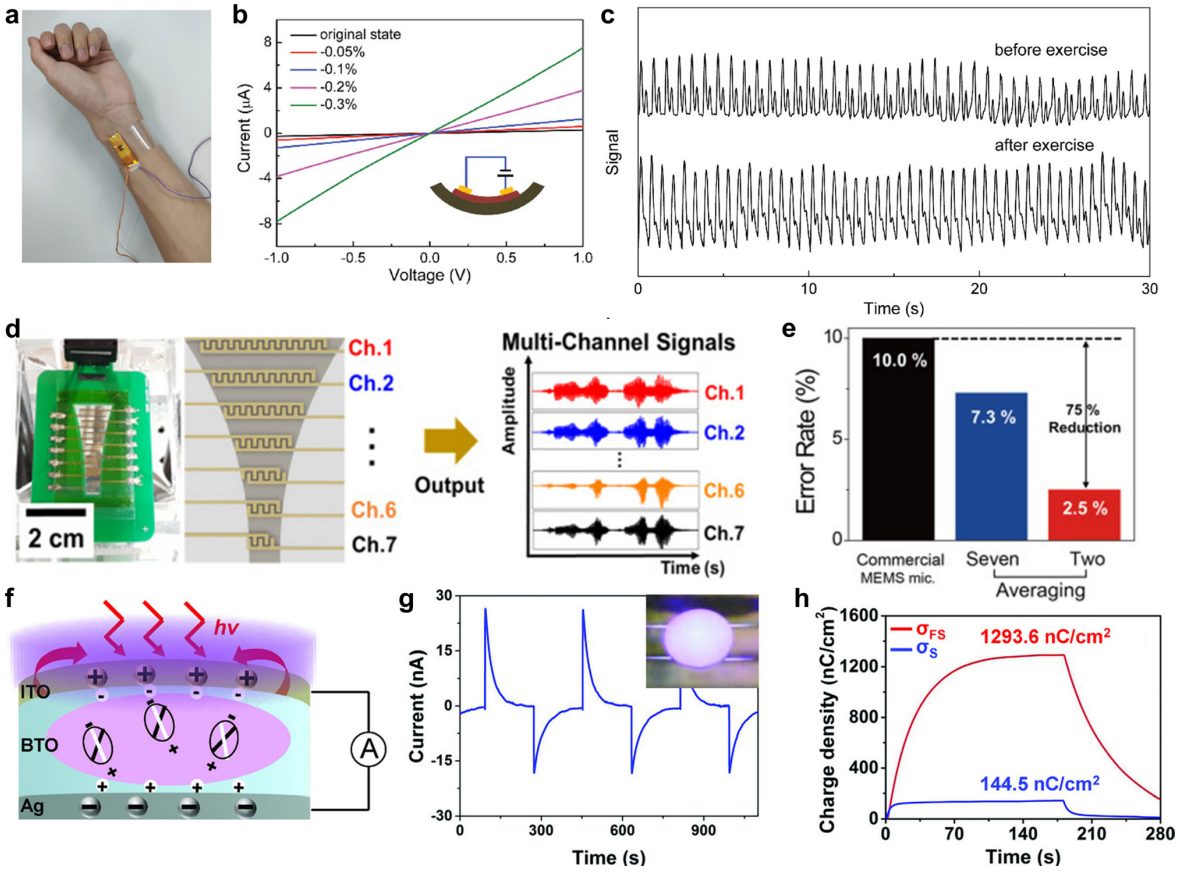

Figure 2.9: Sensors based on freestanding thin films. **a,** Photograph of a tactile sensor formed from freestanding VO_2. **b,** *I–V* curves of VO_2/PET under different bending states. **c,** Real-time radial artery pulse measurements before and after exercise. (**a**-**c**) are adopted from Ref. [62]. **d,** Photograph (left) and schematic (right) of a multi-channel flexible piezoelectric acoustic sensor. **e,** Comparison of recognition error rate. (**d**-**e**) are adopted from Ref. [114]. **f,** Schematic of ITO/BTO/Ag photodetector. **g,** Output currents under 365 nm illumination for freestanding photodetectors. **h,** Charge density for device on the substrate and in freestanding state. (**f**-**h**) are adopted from Ref. [115].

Energy applications

As a result of global warming and the rapid depletion of fossil fuels, the search for alternative energy sources and novel energy storage methods is becoming increasingly urgent. Freestanding thin films can also be applied in energy applications. K. -I. Park et al. [116] reported an energy harvester based on freestanding PZT thin film obtained through a laser

lift-off process (Fig. 2.10 a). The nanogenerator can reach a high output of $\sim$200 V and 150 µA/cm^2 under a small strain. In addition, by deforming the large-area freestanding membrane with a human finger, they illuminated an array of 105 blue light-emitting diodes (Fig. 2.10 b-c). D. Cheng et al. [79] reported a freestanding lithium phosphorus oxynitride (LiPON) thin film that can be used in a flexible and transparent solid-state lithium-ion battery (Fig. 2.10 d). The cell demonstrated stable plating and stripping over 13 cycles with no apparent degradation (Fig. 2.10 e). Freestanding LiPON can be used to shuttle lithium ions. The use of freestanding thin films can promote the development of energy applications.

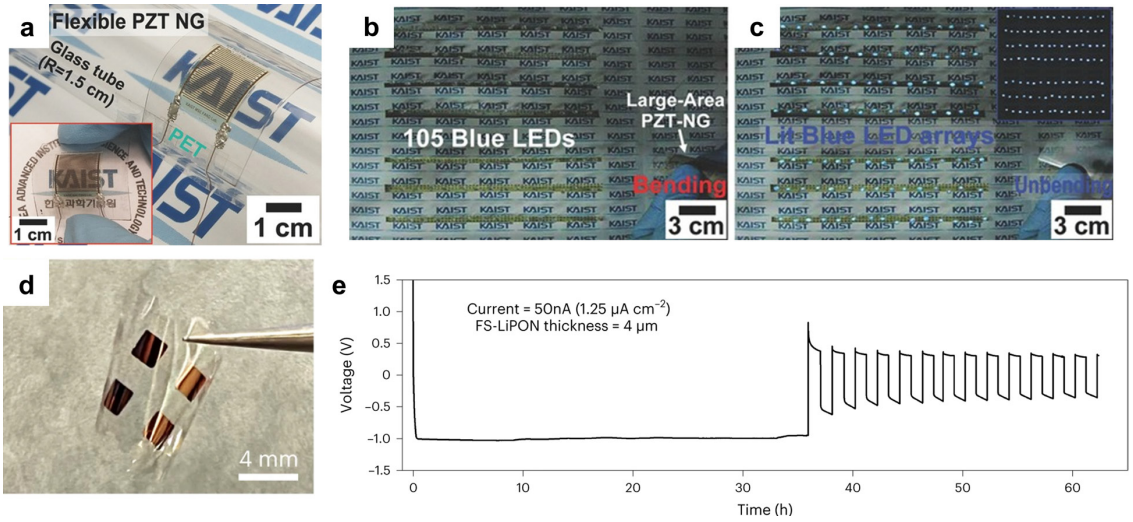

Figure 2.10: Energy devices based on freestanding thin films. **a,** Photos of a nanogenerator based on freestanding PZT attached to a glass tube and bent by fingers. **b,c,** The instantaneous lighting up of 105 commercial blue LEDs by bending (**b**) and releasing (**c**) the freestanding PZT. (**a**-**c**) are adopted from Ref. [116]. **d,** Photograph of the flexible LiPON Li-Cu cell. **e,** Voltage curve of lithium metal plating and stripping in the cell. (**d**-**e**) are adopted from Ref. [79].

Transistors

In order to build highly efficient electronic devices, scaling down and increasing the integration density are becoming increasingly important. However, this can be hindered by short channel effect and gate tunneling. To overcome these difficulties, high-κ materials, which exhibit higher gate insulation performance than conventional SiO_2, have attracted much attention. Some high-κ materials, such as HfO_2, can be deposited directly on Si using ALD or chemical vapor deposition (CVD) [117, 118]. However, due to the large structural difference between high-κ materials and silicon, the crystallinity of the high-κ material can be degraded, thus affecting the device performance [119]. On the other hand, 2D materials with excellent electrical and mechanical properties are recognized as promising candidates for next-generation channel materials. However, it is hard to deposit other materials, such as high-κ oxides, on top of 2D materials because there are no dangling bonds (which act as nucleation sites) on the surface and defects in 2D materials may be generated during growth. Without these drawbacks, freestanding high-κ materi-

als can be easily integrated with 2D materials on Si to form transistors. For instance, A. J. Yang et al. [11] reported a high performance MoS_2-based field-effect transistor (Fig. 2.11 a). As shown in Fig. 2.11 b, the transfer (I_D-V_G) curves exhibit characteristics of *n*-type transistors with a high on/off ratio (> 108) and a near-ideal subthreshold swing (SS) ($66\,\mathrm{mV\,dec^{-1}}$), close to the thermionic limit at room temperature), indicating a good interface quality. Inverters, which can be applied in digital circuits, can further be fabricated from the STO-gated transistors (Fig. 2.11 c). The high voltage gain values ($-\mathrm{d}V_{OUT}/\mathrm{d}V_{IN}$) show that the inverter is suitable for logic circuits and is robust against errors. Subsequently, J.-K. Huang et al. [32] demonstrated the applicability of the similar structure in large-scale device fabrication by integrating freestanding STO thin films on CVD-grown MoS_2 (Fig. 2.11 d). The correlation between the on/off ratio and the SS value of 50 devices confirmed good and stable device performance (Fig. 2.11 e).

Freestanding functional oxides, e.g. PZT, can also be integrated on a Si device [44]. The transfer curve shows counter-clockwise hysteresis for the transistor, indicating ferroelectric control of the charge, while the abrupt change in the current shows good crystallinity of the freestanding PZT thin film (Fig. 2.11 f). Other groups also reported freestanding ferroelectric/AlGaN/GaN high electron mobility transistors [120]. In addition, nitride-based semiconductors, such as AlGaN/AlN/GaN, were also detached from the substrate by an electrochemical lift-off process and then used in flexible transistor arrays [121]. In short, freestanding techniques can be used to fabricate novel transistors based on complex oxides and 2D materials with improved and emerging functionalities.

In conclusion, freestanding thin films can be used in various kinds of applications, creating more possibilities compared to conventional epitaxy. This can open up new routes for the fabrication and design of next-generation devices with superior performance, as it allows the selection of the optimal materials, whatever they are - complex oxides, 2D materials, III-V semiconductors, etc.

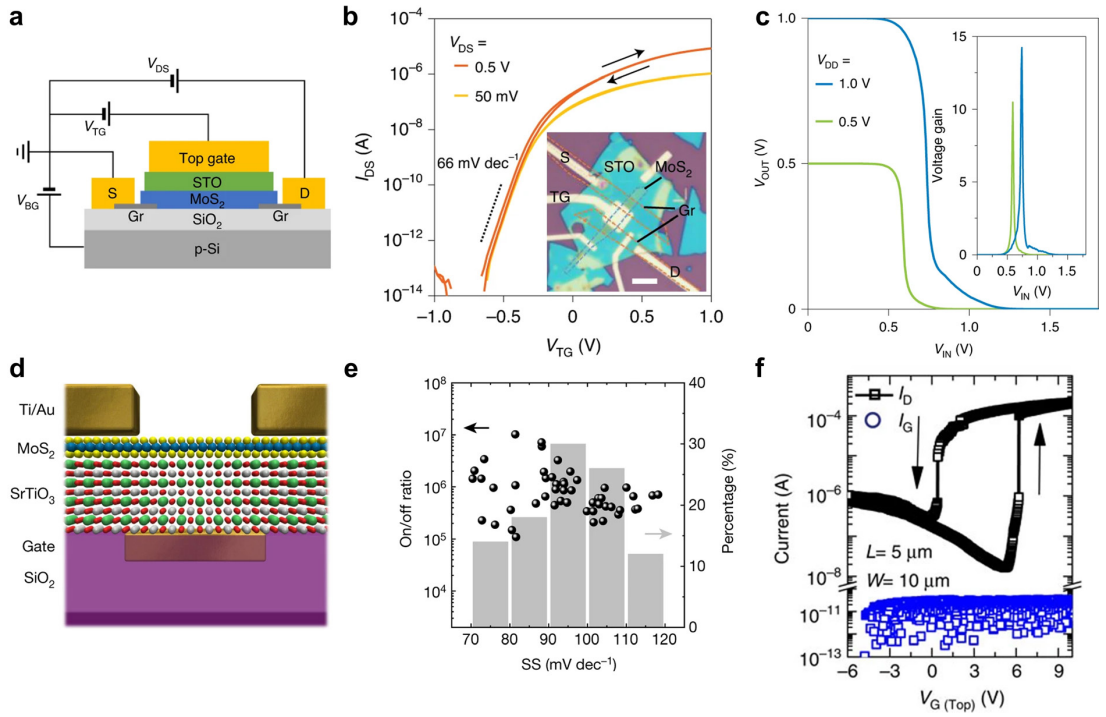

Figure 2.11: Transistors based on freestanding thin films. **a,** Schematic of the double-gated transistor based on freestanding STO. **b,** Double sweep I_{DS}-V_{TG} curves of the device with back gate grounded. The inset shows the optical image of the device. **c,** Voltage transfer curves of an inverter built on a WSe_2 *p*-type and MoS_2 *n*-type transistor. The inset shows the voltage gain of the device. (**a**-**c**) are adopted from Ref. [11]. **d,** Schematic of the local back-gated field-effect transistor. **e,** Scatter distribution (black dots) of on/off current ratios and subthreshold swing (SS) values, and statistical histogram (grey columns) of SS. (**d**-**e**) are adopted from Ref. [32]. **f,** I_D-V_G (top gate) characteristics of the ferroelectric transistor based on freestanding PZT with back gate grounded (adopted from Ref. [44]).

2.3 Water-soluble $(Ca, Sr, Ba)_3Al_2O_6$

Nowadays, $(Ca, Sr, Ba)_3Al_2O_6$ compounds have been widely used as sacrificial buffer layers to obtain freestanding thin films [66–69, 72, 73, 80, 81, 122]. This is mainly due to their ease of dissolution in water, their similar structures to those of perovskites, and their good chemical compatibility. As an example, the most commonly used SAO has a cubic unit cell (space group $Pa\bar{3}$), consisting of Sr ions and AlO_4 tetrahedrons (Fig. 2.12 a), with a lattice constant a = 15.844 Å [123]. On the one hand, the discrete $Al_6O_{18}{}^{18-}$ rings are easily reacted with water, resulting in a much higher water solubility of SAO than those aluminates with a continuous Al-O framework. On the other hand, the structure of SAO is very close to 4 times that of the most representative perovskite substrate material STO (a = 3.905 Å). As shown in Fig. 2.12 b and c, a 75% match of the oxygen sublattice of 4×4 STO and SAO can be clearly seen, while the 25% mismatch can be considered as vacancies. This strong resemblance allows the layer-by-layer growth of many perovskites on SAO, monitored by clear reflection high energy electron diffraction (RHEED) oscillations [28, 66, 68]. Furthermore, extremely thin freestanding membranes, down to the 2D limit, can be obtained with this sacrificial layer, indicating that the crystallinity of SAO is well preserved down to a few unit cells [28]. In addition, the epitaxial relationship between the sacrificial SAO and the target perovskite oxides exists not only in the (001) orientation but also in the (110) and (111) orientations, demonstrating the versatility of this sacrificial buffer. For instance, freestanding (110)- and (111) - oriented LSMO and SRO were obtained after alternating the orientation of the substrates and dissolving SAO [87, 124]. It is worth noting that the crystallinity of SAO deposited along (001) is the best among the three orientations, as confirmed by RHEED patterns.

As a family of isostructural compounds, $(Ca, Sr, Ba)_3Al_2O_6$ allows tuning of the lattice constant from 15.263 Å [126] to 16.498 Å [127] by varying the Ca:Sr:Ba ratio. This further facilitates the deposition and release of high quality freestanding thin films by reducing lattice mismatches and cracks that can be generated during the lift-off process. For example, P. Singh et al. [73] compared the quality of freestanding La-doped BaSnO3 membranes released from STO substrates using SAO and $Ba_3Al_2O_6$ (BAO) buffers and found that lattice-matched BAO resulted in a large-area high-mobility membrane, whereas SAO led to a high crack density. For the same purpose, $Ca_2SrAl_2O_6$ [128], $Ca_{1.5}Sr_{1.5}Al_2O_6$ [122] and $CaSr_2Al_2O_6$ [129, 130] have also been used as sacrificial buffers. Fig. 2.12 d summarizes the pseudo-cubic lattice parameters of the sacrificial layers together with some representative oxides [125]. Most of the oxide materials are unstable in either acidic or oxidizing solutions. The use of water as a general etchant greatly expands the family of freestanding thin films. Furthermore, $(Ca, Sr, Ba)_3Al_2O_6$ is safe and eco-friendly compared to $SrVO_3$ (SVO), which is toxic and therefore requires special care in handling [74].

However, the solubility of $(Ca, Sr, Ba)_3Al_2O_6$ is also determined by its composition. In the case of $Ca_3Al_2O_6$, it is poorly soluble in water due to the strong Ca-O bond [131]. By substituting Ca with Sr or Ba, the solubility can be greatly improved [66, 73]. Also,

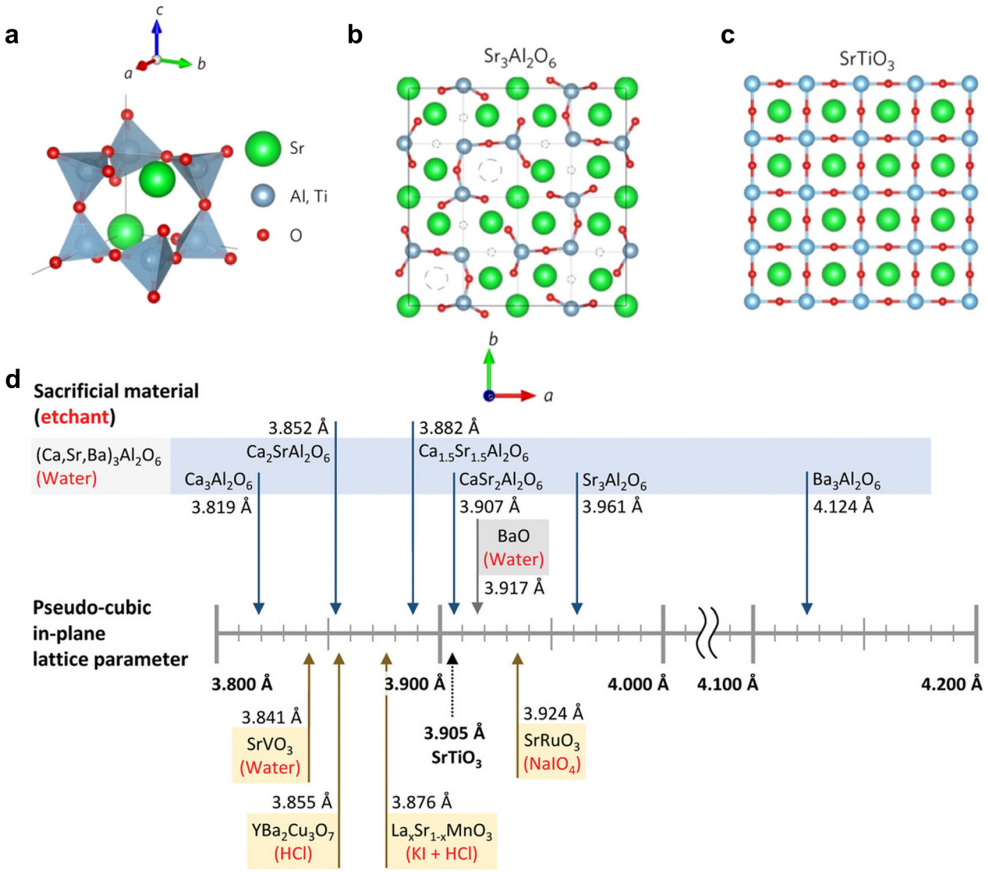

Figure 2.12: Structure of $(Ca, Sr, Ba)_3Al_2O_6$ compounds. **a,** $Al_6O_{18}{}^{18-}$ rings in SAO. **b,c,** Crystal structure of upper $\frac{1}{4}$ of the SAO unit cell (**b**) and of 4×4 unit cells of STO (**c**) projected onto the (001) plane. Dashed circles indicate vacancy sites. (**a**-**c**) are adopted from Ref. [66]. **d,** Lattice parameters of cubic or pseudo-cubic sacrificial materials. Blue highlights the $(Ca, Sr, Ba)_3Al_2O_6$ compounds and yellow highlights some other sacrificial materials (adopted from Ref. [125]).

the etching rate is related to the thickness of the sacrificial layer. A thicker sacrificial layer gives a higher etching rate, but may also affect the quality of the target materials, as the surface and crystallinity of the buffer layers may deteriorate with increasing thickness, especially in the case of PLD deposition. Considering that some target materials, such as YBCO, can also react with water [132], it should be careful with the choice of sacrificial layers. Alternatively, a sacrificial material with an ultrafast etching rate in water, such as $Sr_4Al_2O_7$, whose dissolution rate is nearly 10 times that of SAO, can also reduce potential dissolution damage [133].

It is noteworthy that the extreme growth conditions of $(Ca, Sr, Ba)_3Al_2O_6$, which usually involve high temperatures (>700 °C) and low oxygen partial pressure ($< 10^{-5}$ Torr), can lead to cationic interdiffusion at the interface and further affect the quality of target materials and the solubility of sacrificial materials [134]. This problem can be solved by inserting an ultrathin layer of STO (5 u.c.) between the sacrificial buffer layer and the target materials as an effective barrier [135]. In addition, the STO capping was found to be sufficient to protect the sacrificial layer from moisture, facilitating further combination with other deposition methods [136]. This is important for the deposition of heterostructures, as different types of materials may require optimizations in different chambers. For example, in our experiment (Chapters 5-6), an MgO buffer was used. This allows samples to be transferred from our PLD chamber to the sputtering chamber for subsequent depositions.

In conclusion, water-soluble $(Ca, Sr, Ba)_3Al_2O_6$ is a good candidate as a sacrificial buffer layer due to its tunable composition and lattice constant. Various kinds of freestanding membranes have been obtained by dissolving it in water, which has proven to be an environmentally friendly and safe process. Therefore, we also used SAO as a sacrificial buffer layer to obtain freestanding membranes (details in Chapters 5-8).

2.4 Lift-off and transfer process

In the wet etching process, the lift-off and transfer of freestanding thin films plays an important role, since it can greatly affect the quality and integrity of the freestanding membrane (Fig. 2.13 a) [46, 137]. This process can be mainly divided into 3 main steps: separation of the freestanding membrane from the substrate, transfer to specific bases, and removal of the support layer. Thanks to the rapid development in the exfoliation and transfer of 2D materials, we can refer to the well-established transfer process of vdW materials, such as graphene [138]. Just as polymer is used to support the 2D vdW materials during stamp transfer, a polymer capping layer is usually spin-coated or attached to the surface of the sample before the as-deposited sample is immersed in etchant. This protective capping can reduce the formation of wrinkles and folds during the etching process [139]. Many polymers and their combinations have been used as support layers, such as polyimide (PI) tape [46, 87], PDMS [28, 66], polymethyl-methacrylate (PMMA) [47, 67], etc. After separating the freestanding thin film from the substrate, the freestanding membrane

is then picked up together with the polymer support layer or scooped out of the water by the transfer base. Finally, the protective capping layers often need to be removed for further device fabrications, characterizations, etc.

However, this 3-step process has its own drawbacks. First of all, the process is complex, which hinders the potential integration with other structures, such as 3D structures. Second, the capping layer always covers the top surface of the as-deposited thin film, and if we want to characterize the bottom surface and turn the sample upside down, the polymer capping cannot be easily removed. Third, the process can limit the choice of bases, as some materials are weak against the heat or solvent used to remove the polymer capping. Fourth, freestanding membranes are prone to cracking during peeling or dissolution, which can limit their applications. For example, thermal release polymers such as PDMS ensure a better surface with negligible residues [66], but the heating and peeling off process inevitably introduces cracks. On the other hand, adhesive tape, such as PI tape, has been used to obtain large-area freestanding membranes with no visible damage [46], while it is almost impossible to remove the tape from freestanding membranes.

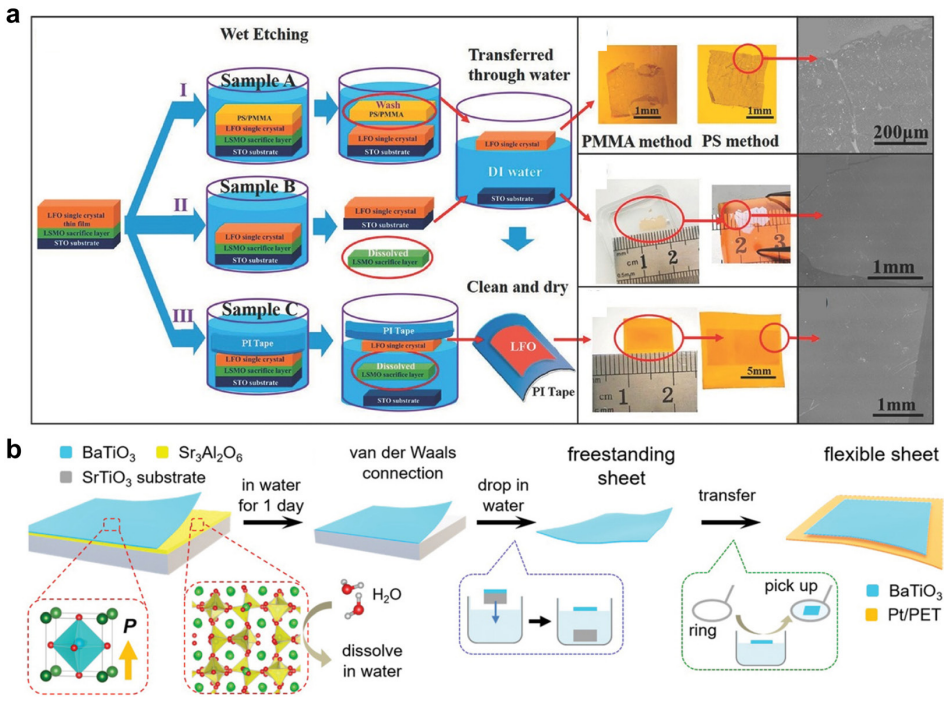

Figure 2.13: Lift-off and transfer of freestanding thin films. **a,** Schematic of three different lift-off and transfer methods and corresponding optical and SEM images of freestanding samples after transfer (adopted from Ref. [46]). **b,** Schematic of the water membrane based lift-off and transfer technique (adopted from Ref. [140]).

To overcome these difficulties, in my previous study, I have developed a method using a water membrane to support the freestanding thin films [140]. It is more versatile than the common methods discussed above. As schematically illustrated in Fig. 2.13 b, after dipping the freestanding membrane on STO into water again, the freestanding membrane can be separated from the substrate, which sinks in water, and then floats on the water surface. Due to the existence of water surface tension, we can form a water membrane

that can hold the freestanding membrane in a ring-like tool. The freestanding membrane together with the water membrane can be picked up by the ring and transferred onto other bases. If the freestanding thin film is single crystal and has a small mismatch with the substrate, no capping polymer is required.

This method easily produces large-size single-crystal crack-free SRO membranes, and the STO substrates can be reused, as demonstrated in Fig. 2.14. There are several additional advantages: 1, it is possible to turn the freestanding membranes upside down; 2, this method allows easy integration with most bases, including polymer, copper mesh, grids, etc.; 3, water surface tension can drag the freestanding thin films during evaporation of residual water, facilitating the formation of 3D structures. Considering these advantages, this water membrane based method was used to obtain freestanding membranes, which are discussed in this thesis (Chapters 5-8).

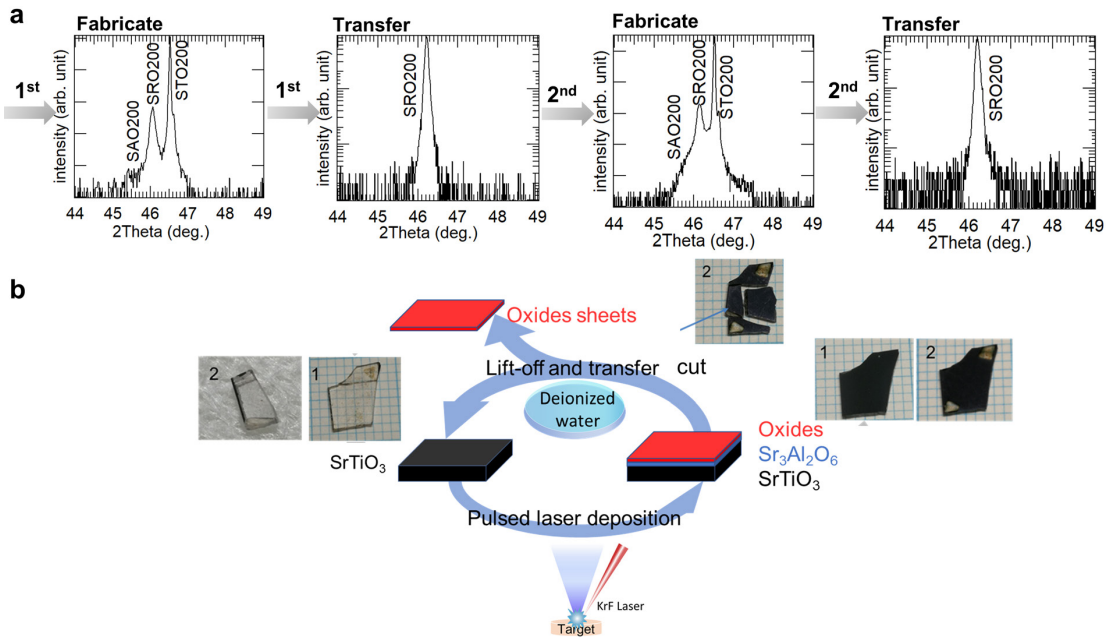

Figure 2.14: Substrate reuse. **a,** θ-2θ XRD pattern of SRO sheets and SAO/SRO bilayer films showing different stages of the substrate reuse process (adopted from Ref. [140]). **b,** Schematic of the substrate reuse process. Photos show the SAO/SRO bilayer films and bare STO substrates.

Chapter 3

Magnetic racetrack memory

Conventional electronic integrated circuits exploit the flow of electrons by using transistors, where the charge of electrons is used to represent digital signals. In addition to charge, spin, another intrinsic property of electrons, can also be used for information technology. Recently, spintronic devices, in which the spin and charge of electrons are used for data storage and processing, have attracted much attention for their promising future in next-generation, non-volatile, energy-efficient, higher-speed applications in computing [141]. A representative example is a non-volatile high-density memory device named Magnetic Random Access Memory (MRAM), which consists of an array of magnetic tunnel junctions and is already commercially available [142]. Different from MRAM, RTM uses a different strategy to process data. Here, individual bits can be encoded in magnetic DWs that are manipulated by electric current pulses within a single racetrack element, while reading devices can be integrated at fixed positions along the racetrack channel [143]. Due to the small width and high motion velocity of the DWs, RTM goes beyond MRAM, showing the possibility to realize larger data capacities and much higher processing speed. Since I used freestanding heterostructures to build freestanding RTM devices (Chapters 5-7), it is worth introducing the background of RTM at the beginning. In this chapter, I will first introduce the physical mechanism behind magnetic DWs, including their stabilization. Next, I will introduce the dynamics of DWs - that is, DW motion driven by field, spin-transfer torque, spin-orbit torque and exchange coupling torque - and their applications in RTM. Finally, DW motion in 3D structures will also be briefly reviewed, since it is related to our work in building 3D RTM devices.

3.1 Magnetic domain wall

3.1.1 Magnetism and magnetic interaction

Diamagnetism is a quantum mechanical effect of all materials, since any external magnetic field will generate effective currents in the orbitals of electrons that would oppose the change. Only if the material possess no other magnetism, i.e. its atoms have no net magnetic moment, can it be defined as a diamagnetic material. This is because the

magnitude of diamagnetism is quite small (magnetic susceptibility $\chi \sim 10^{-5}$) and it can be easily overcome by other magnetisms. But there is one exception, superconductors, which completely repel external magnetic fields from their interior, known as the Meissner effect ($\chi = -1$). Similar to diamagnetism, paramagnetism is also a weak magnetism ($\chi \sim 10^{-5} - 10^{-3}$) and paramagnetic materials can form a weak magnetization in the direction of the applied magnetic field. Due to the spin of the unpaired electrons in the materials, the atoms have a permanent magnetic dipole moment. In paramagnetic materials, these dipoles have no significant interaction with each other and are randomly oriented in the absence of an external field, resulting in a zero net magnetic moment of the materials. In addition, itinerant electrons can also lead to diamagnetism or paramagnetism, as explained by Landau diamagnetism or Pauli paramagnetism.

However, the term of magnetic structure refers to an ordered arrangement of magnetic moments that results in strong magnetic behavior. FM, antiferromagnetic, and ferrimagnetic structures are three typical magnetic structures (Fig. 3.1).

Fe, Co, Ni and alloys based on these elements have spontaneous magnetization below their Curie temperature and their magnetization decreases with increasing temperature. At temperatures above the Curie temperature, these materials exhibit paramagnetism. To explain these results, Weiss assumed that there are interactions between the magnetic ions, which are defined as "molecular field" based on phenomenology [144]. The "molecular field" is a kind of mean field and is proportional to the magnetization. Magnetic interaction between neighboring magnetic moments was thought to be a possible origin of the "molecular field", but the magnitude of magnetic dipolar interaction is quite small compared to the large "molecular field". After the discovery of quantum mechanics, Heisenberg proposed that electrons localized in the vicinity of atoms can create direct exchange interactions between magnetic ions, known as the Heisenberg exchange model [145]. The interaction energy can be written as:

$$\mathscr{H} = -2J_{ex}\boldsymbol{S}_i \cdot \boldsymbol{S}_j = \begin{cases} -\dfrac{\hbar^2}{2}J_{ex} & \uparrow\uparrow \\ +\dfrac{3\hbar^2}{2}J_{ex} & \uparrow\downarrow \end{cases} \text{(condisering 2 electrons)} \tag{3.1}$$

J_{ex} is the exchange coupling constant, $\boldsymbol{S}_{i/j}$ is the spin of the atoms, $\uparrow\uparrow$ or $\uparrow\downarrow$ refers to spin triplets with parallel spins and spin singlets with antiparallel spins. When $J_{ex} > 0$, parallel spins will have lower energy, leading to a ground state of ferromagnetism (Fig. 3.1 top). On the other hand, antiparallel spins are favored when $J_{ex} < 0$, resulting in an antiferromagnetic system with zero net magnetization (Fig. 3.1 middle). Considering more complex cases where the total spins are different for different magnetic ions, this difference between the closest magnetic moments will lead to ferrimagnetism (Fig. 3.1 bottom). Due to the Pauli Exclusion Principle, different spin orientations determine different spatial wave functions and distributions of electrons, resulting in different Coulomb interaction energies. In other words, the Coulomb interaction is the origin of the ex-

change interaction. In addition, some materials, such as MnO, whose 3*d* orbitals of the magnetic Mn^{2+} ions are far apart from each other due to the presence of O^{2-} in between, have a weak Heisenberg direct exchange interaction. Their antiferromagnetism should be explained by the indirect exchange interaction between magnetic ions mediated by intermediate non-magnetic ions, the so-called super-exchange interaction. Moreover, if there is a mixed valence state of the transition metal ions, caused by doping, etc., electrons can jump between close neighboring ions, leading to ferromagnetism. This is explained by the double-exchange interaction.

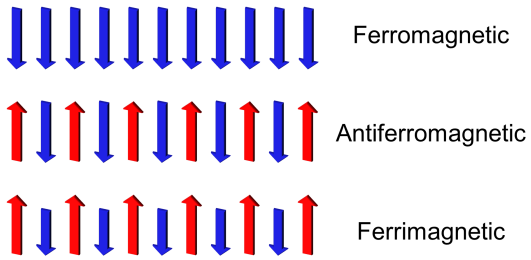

Figure 3.1: Schematic of ferromagnetic, antiferromagnetic and ferrimagnetic structures. The different arrows indicate the magnetic moments of different atoms.

The Heisenberg exchange model assumes that the electrons producing the magnetism are localized around the atoms in the crystal. However, based on this theory, the calculated atom's saturation magnetization should always be an integer multiple of the Bohr magneton (μ_B), which is inconsistent with the experimental data. This is because the electrons are not simply localized close to the atoms, but form a non-localized band. Considering 3*d* electrons, the electron-electron interaction can lead to a split between spin-up and spin-down electron bands (Fig. 3.2). The magnetic susceptibility can be written as [146]:

$$\chi = \frac{\chi_P}{1 - \frac{1}{2}UN(E_F)} \tag{3.2}$$

$\chi_P = \mu_0 \mu_B^2 N(E_F)$ is the magnetic susceptibility for Pauli paramagnetism [147], U is the Coulomb interaction between electrons, $N(E_F)$ is the density of states at the Fermi surface. Compared to χ_P, χ is increased by the Stoner factor (S):

$$S = \frac{1}{1 - \frac{1}{2}UN(E_F)} \tag{3.3}$$

Considering that the *d*-band is a narrow band, $N(E_F)$ and U are relatively large, resulting in a large χ and stabilization of ferromagnetism. Unlike the 3*d* electrons, the localized inner 4*f* electrons are difficult to interact with each other directly, so they are coupled via conduction electrons. This interaction is known as the Ruderman–Kittel–Kasuya–Yosida (RKKY) interaction, which can be used to explain the origin of ferromagnetism in 4*f* rare earth metals, antiferromagnetic coupling in multilayers, etc.

Another indirect interaction, called the Dzyaloshinskii–Moriya interaction (DMI), is very important in material systems with broken inversion symmetry and strong spin-orbit

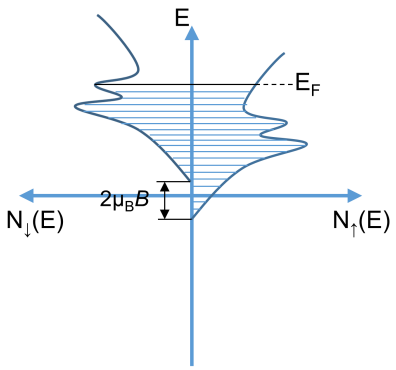

Figure 3.2: Split between electron bands caused by electron-electron interaction in a ferromagnetic metal.

coupling (SOC), which can result in canting of the neighboring spins. DMI describes an antisymmetric interaction where the spins interact through a third ligand and can be written as [148, 149]:

$$\mathscr{H}_{\mathrm{DMI}} = -\boldsymbol{D}_{ij} \cdot (\boldsymbol{S}_i \times \boldsymbol{S}_j) \tag{3.4}$$

Here, $\boldsymbol{D}_{ij}$ is the DMI constant vector, indicating the direction and magnitude of DMI.

3.1.2 Magnetic anisotropy and magnetic domain

In the previous section we focused mainly on the moment of magnetic atoms, but in real materials more factors need to be taken into consideration. For example, the anisotropy of the crystal structure can determine the anisotropy in the crystal field, the exchange interaction and the dipolar interaction, and further determine the magnetic anisotropy in materials; while the SOC in crystals and the anisotropy of the electron energy band can determine the orientation of the electron orbital, so that the moments of atoms and then the magnetization of materials are always aligned along some special crystallographic axes, known as easy axes. Considering the simplest case of uniaxial anisotropy, the anisotropy energy can be simply written as [150]:

$$E_A = K_u \sin^2 \theta \tag{3.5}$$

Higher order trivial terms are negligible, θ is the angle between the OOP perpendicular axis and the magnetization direction (Fig. 3.3), K_u is the uniaxial anisotropy constant. If $K_u > 0$, E_A can reach a minimum at $\theta = 0$ or π, resulting in a PMA. If $K_u < 0$, E_A will be minimized when $\theta = \frac{\pi}{2}$ or $\frac{3\pi}{2}$, leading to an IP magnetic anisotropy. If more energy terms are included, such as magnetostatic energy, K_u can be treated as K_u^{eff}, known as the effective uniaxial magnetic anisotropy constant. The effective uniaxial anisotropy field H_K^{eff}, which is the minimum field that can drive the magnetization perpendicular to the easy axis, can be written as [151, 152]:

$$H_K^{\mathrm{eff}} = \frac{2K_u^{\mathrm{eff}}}{\mu_0 M_{\mathrm{s}}} \tag{3.6}$$

M_s is the saturation magnetization of the sample. H_K^{eff} can be determined from the magnetization-field curve measured along the hard axis.

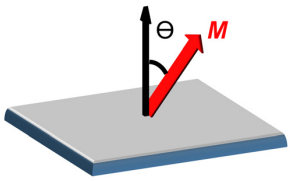

Figure 3.3: Magnetization direction in a thin film sample.

On the other hand, when looking at a large-scale sample, the sample should be divided into many small magnetic regions, in which the spontaneous magnetization is aligned in the same way. These small regions are called magnetic domains. The origin of the multi-domain structure is the competition between different energy terms. For example, the exchange interaction favors the case where all moments are aligned in the same direction, while other energy terms, such as the dipolar interaction, do not. To achieve a minimum total energy, multi-domains are then stabilized in the sample. It should be recognized that with a sufficiently strong external field, a single domain can also be stabilized in FM materials, and cooling from above the Curie temperature with this field, known as field cooling, can lead to a single domain structure. Correspondingly, cooling without an external field, known as zero field cooling, always creates multi-domains. Cooling with different fields may result in different magnetic structures, which is often used to investigate the magnetic properties of materials. In addition, in our experiment, we can set DWs by alternating the external magnetic field.

The transition region between different magnetic domains is the magnetic DW. Considering one of the simplest cases, where FM materials have a strong PMA, the magnetic DW is stabilized by the competition between the exchange interaction and the PMA, resulting in a DW structure with finite width [153]:

$$\begin{cases} \theta(y) = \pm 2 \arctan \exp(\frac{y}{\Delta}) \\ \varphi(y) = \Psi = \text{const} \end{cases} \tag{3.7}$$

Δ is the DW width, as the rotation is mostly concentrated in a region of width $\pi\Delta$ around the center; θ and φ are the polar and azimuthal angles of the magnetization, respectively (Fig. 3.4). Δ can be further determined by [151]:

$$\Delta = \sqrt{\frac{A}{K_u^{\text{eff}}}} \tag{3.8}$$

Here, K_u^{eff}, the effective uniaxial magnetic anisotropy constant, is explained in the beginning of this section, and A is the exchange stiffness. Thus, when the exchange interaction is large, i.e., A is large, the magnetization is more likely to align in one direction, resulting in a wider DW; when the PMA is large, i.e., K_u^{eff} is large, the magnetization prefers

to align along the easy axis, resulting in a narrower DW. In addition, φ is a fixed value in this DW configuration. This angle is also determined by the energy terms of the material system. For example, the long-range dipolar interaction in PMA samples favors the stabilization of the Bloch type DW, where φ is equal to 0 or π. Two types of chirality are degenerate in energy here, i.e. the Bloch type DW is achiral. However, taking into account the DMI, φ is equal to $\pm\frac{1}{2}\pi$ and a Néel type DW with fixed chirality is stabilized. These four typical types of DWs are illustrated in Fig. 3.4.

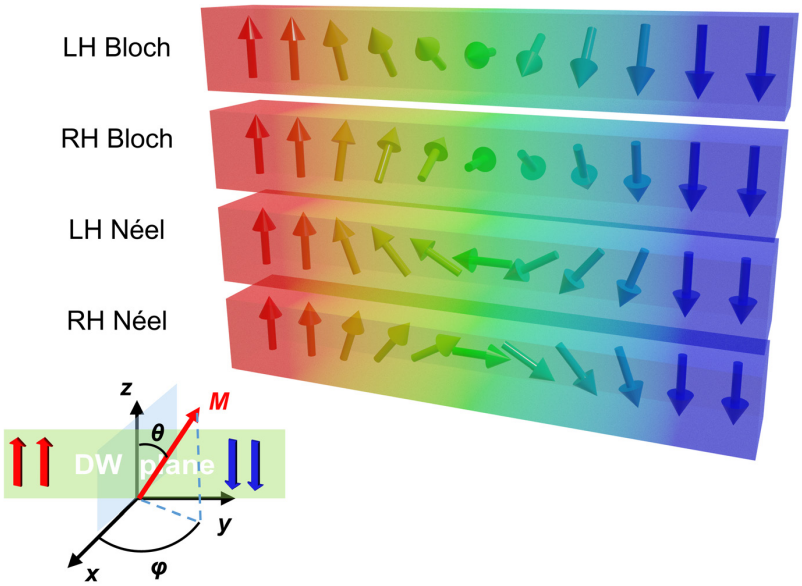

Figure 3.4: Illustration of the magnetic structure in four types of DWs. From top to bottom: Left-hand (LH) Bloch wall, right-hand (RH) Bloch wall, LH Néel wall, and RH Néel wall. Left-bottom: coordinate axes for the one-dimensional DW model.

3.2 Magnetic domain wall motion

3.2.1 Field-driven domain wall motion

The magnetization dynamics is based on the fundamental mechanics that the time-dependent magnetization change is proportional to a torque $\boldsymbol{T}$ by a constant, which can be written as:

$$-\frac{\mathrm{d}\boldsymbol{M}}{\mathrm{d}t} = \gamma \boldsymbol{T} \tag{3.9}$$

γ is the gyromagnetic ratio, and any torque on the magnetization can be considered to be provided by an effective field $\boldsymbol{H}_{\mathrm{eff}}$ (this effective field is a combination of the external magnetic field, the demagnetizing field (also known as the stray field), etc.):

$$\boldsymbol{T} = \boldsymbol{M} \times \boldsymbol{H}_{\mathrm{eff}} \tag{3.10}$$

By expressing $\boldsymbol{H}_{\text{eff}}$ and making some simplifications, the Landau-Lifshitz equation can be written as [154]:

$$\frac{\mathrm{d}\boldsymbol{M}}{\mathrm{d}t} = -\gamma \boldsymbol{M} \times \boldsymbol{H}_{\text{eff}} - \lambda \boldsymbol{M} \times (\boldsymbol{M} \times \boldsymbol{H}_{\text{eff}}) \tag{3.11}$$

λ is a phenomenological damping parameter and can be written as:

$$\lambda = \alpha \frac{\gamma}{M} \tag{3.12}$$

α is the dimensionless damping constant, $M = |\boldsymbol{M}(\mathrm{t})|$ is the magnitude of the magnetization. The damping term in the Landau-Lifshitz equation can be replaced by a term that depends on the time derivative of the magnetization [155]:

$$\frac{\mathrm{d}\boldsymbol{M}}{\mathrm{d}t} = -\gamma \left(\boldsymbol{M} \times \boldsymbol{H}_{\text{eff}} - \eta \boldsymbol{M} \times \frac{\mathrm{d}\boldsymbol{M}}{\mathrm{d}t} \right) \tag{3.13}$$

η is the damping parameter, which is determined by the material. As illustrated in Fig. 3.5, the first term, field-like torque, leads to precession around the field direction; and the second term, damping-like torque, leads to the final direction of the magnetization along the direction of the magnetic field.

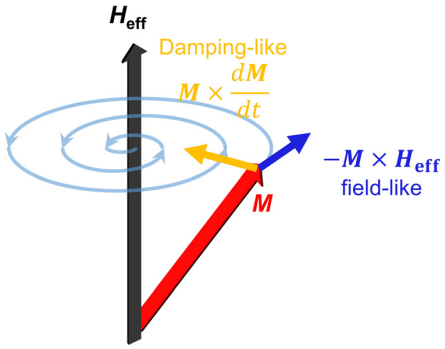

Figure 3.5: Illustration of the torques exerted on the magnetization. The terms of the Landau-Lifshitz equation are: precession (blue) and damping (yellow). The trajectory of the magnetization is marked by the spiral.

Considering the simplest one-dimensional DW with PMA case, by using the Landau-Lifshitz equation and the DW structure described as Eq. (3.7) ($\varphi(y,t) = \psi(t)$ and $\theta(y,t) = 2\arctan\exp\{[y-q(t)]/\Delta(t)\}$), one can obtain the expressions related to the differential of the wall energy $\mathrm{d}\sigma$ [153]:

$$\begin{cases} \dfrac{\partial \sigma}{\partial \psi} = 2\dfrac{M}{\gamma}(\dot{q} - \alpha\Delta\dot{\psi}) \\ \dfrac{\partial \sigma}{\partial q} = -2\dfrac{M}{\gamma}(\dot{\psi} + \dfrac{\alpha\dot{q}}{\Delta}) \end{cases} \tag{3.14}$$

Here, $\dot{q} = \mathrm{d}q/\mathrm{d}t$ and $\dot{\psi} = \mathrm{d}\psi/\mathrm{d}t$. Solutions of the DW motion velocity can be obtained after considering the conservation of energy, in a steady motion case, that is $\dot{q}(t) = V$ and $\dot{\psi} = 0$, the velocity V can be written as:

$$V = \frac{\gamma \Delta H}{\alpha} \tag{3.15}$$

H is the magnitude of the magnetization in the OOP direction (z-axis). The DW velocity in this case is inversely proportional to α and proportional to the field. However, the dynamic equilibrium with $\dot{q}(t) =$ constant and $\dot{\psi} = 0$ is realized by the effective torque, which has its own maximum. Therefore, there is a maximum field above which the linear relationship cannot be maintained, known as the Walker critical field, H_{w}. In Bloch walls with high Q (quality factor, determined by the material,$Q = K_u/(2\pi M^2)$), H_{w} can be written as [153]:

$$H_{\mathrm{w}} = 2\pi\alpha M \tag{3.16}$$

It should be recognized that if DMI is taken into consideration, which is the case for Néel DW, H_{w} can be much higher [156]. When $H > H_{\mathrm{w}}$, the drive term γH cannot be sufficiently balanced and ψ must continue to precess forward. Thus, the velocity must also oscillate due to the periodicity of the torque terms with ψ, known as "breakdown". When $H >> H_{\mathrm{w}}$, the only torque contributing to the velocity is the damping torque. This condition is known as the "free precession" limit, and the velocity is also proportional to the field. However, the above analysis is based on the simplest one-dimensional case, while in the real materials multi-dimensions and more interactions must also be considered, leading to different field-velocity behaviors.

3.2.2 Current-driven domain wall motion

As discussed in the previous section, the external magnetic field is sufficient to move the DWs, but it is not the optimal choice for application in DM devices, such as the racetrack, because the generation of the magnetic field is very energy-consuming, and the magnetic field hinders the minimization and stability of the devices. In addition, the two ends of the magnetic domains are driven in opposite directions, resulting in the annihilation of DWs. On the other hand, current pulse is a good choice because it can effectively drive DWs and can be easily applied in well-developed electronics.

A spin-polarized current generated in a FM material can be used to alter the orientation of the magnetization of the adjacent region in the material. This effect is known as spin-transfer torque (STT) and is often used to change the orientation of the magnetization of free layers after passing through fixed layers in magnetic tunnel junctions (MTJs) (Fig. 3.6). Generally, electric currents are unpolarized, consisting of half spin-up and half spin-down electrons, whereas spin-polarized currents have more electrons of either spin. In STT, this polarized current comes from the spin-dependent scattering in FM materials. Similar to the case of MTJs, STT can be used to drive DWs in the direction of the electron flow. This mechanism was first applied to permalloy (a type of Ni-Fe alloy)

nanowires [157]. Only a small amount of spin angular momentum is lost in the sample due to damping, and a large DW velocity of ~ 110 m s^{-1} can be achieved [158]. This step is the origin of RTM devices, defined as Racetrack Memory 1.0 (Fig. 3.7 a) [159]. However, in soft magnetic materials such as permalloy, the anisotropy is so weak that the DW width is also large, which hampers the application of such materials in high-density information storage. On the other hand, much narrower DWs can be stabilized in materials with significant anisotropy, as discussed in Section 3.1.2 and described by Eq. (3.8). STT-driven DW motion was then realized in material systems with PMA, e.g. Co/Ni multilayers, defined as Racetrack Memory 2.0 (Fig. 3.7 b) [159, 160]. A DW velocity similar to that in soft magnetic materials was demonstrated.

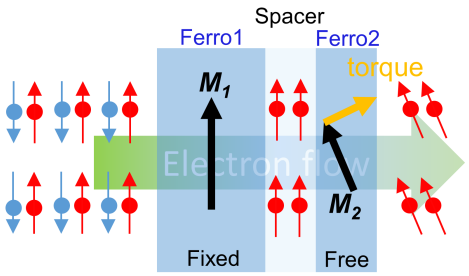

Figure 3.6: Illustration of the spin transfer torque in an MTJ. Spin-polarized currents are generated after passing through the fixed layer and can then affect the magnetization of the free layer.

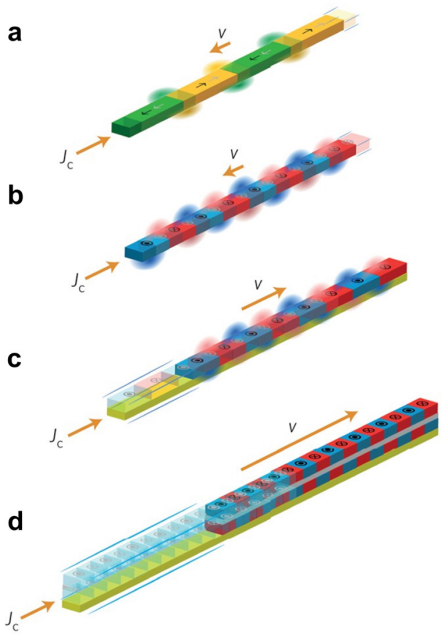

Figure 3.7: Evolution of racetrack memory. **a,** DWs driven by STT in in-plane magnetized racetracks. **b,** DWs driven by STT in perpendicularly magnetized racetracks. **c,** DWs driven by SOT in perpendicularly magnetized racetracks. **d,** DWs driven by the giant ECT in SAF racetracks. Arrows indicate directions of the DW motion and currents. Figures are adopted from Ref. [159].

The DW in multilayers consisting of FM and HM layers was then found to move much faster along the current direction, marking the development of Racetrack Memory 3.0 (Fig. 3.7 c) [159, 161]. In this case, the DW is driven by interface-derived spin-orbit

torques (SOTs). As the name implies, SOTs are derived from the SOC. The detailed mechanism is more complex and involves several distinct effects or interactions, each originating from the SOC. First, as mentioned in Section 3.1.2, DMI favors a stabilization of Néel-type DW with fixed chirality. The DMI field, which is longitudinal (in the DW plane) and independent of the current, alternates its direction between adjacent DWs, i.e. up-down and down-up DWs (Fig. 3.8). This chiral exchange field then imposes a torque on the canting moments in the DWs and drives the DWs to move in the same direction, since they have the same chirality, which is also determined by the DMI [162]. This DMI field can be determined from the DW velocity versus IP longitudinal field curves. Second, the Rashba effect originates from the discontinuity of electronic structures at the interface, which breaks the spin degeneracy of the energy bands and thus leads to spin accumulation when charge currents flow. An effective magnetic field acting on the magnetization of the FM layer is then generated. Third, the spin Hall effect (SHE) in HMs can generate a pure spin current in a direction perpendicular to the current direction towards the HM surface (Fig. 3.9). Its spin direction is perpendicular to both spin and charge current directions. This spin current can generate a STT on the magnetization, defined as SHE-STT. Different from the STT generated by current injection in FM materials used in RTM 1.0 and 2.0, SHE can induce much higher spin currents, because the spin current is not limited by the injection current in SHE. In other words, materials with larger spin Hall angles can generate higher spin currents. Therefore, the SHE-STT can also be larger, resulting in faster DW motion. In addition, both the directions of the field generated by the Rashba effect and the spin current generated by SHE depend on the current direction and not on the direction of the magnetization. These effects together contribute to the fast DW motion with a speed up to ~ 350 m s^{-1} [162]. Moreover, the chirality remaining in the DW potentially facilitates further applications in logic devices. However, the stray fields generated by each DW can still limit the DW density, hindering the realization of high-capacity data storage.

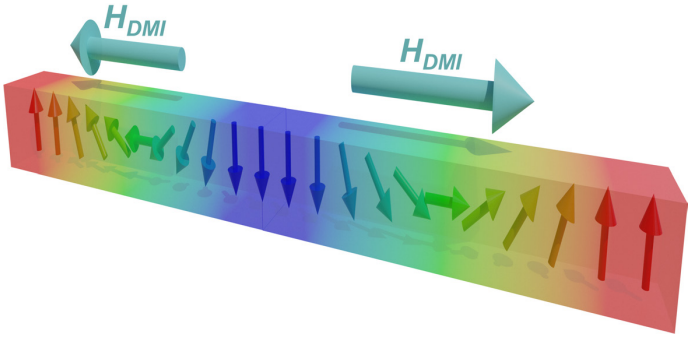

Figure 3.8: Illustration of the DMI field direction in Néel-type DWs. The DMI field alternates its direction between adjacent DWs.

Recently, superfast DW motion has been realized in SAF racetracks with velocities up to 750 m s^{-1} [163]. This advance is known as Racetrack Memory 4.0 (Fig. 3.7 d). An SAF structure consists of two perpendicularly magnetized FM layers that are antiferromagnetically coupled via a spacer layer by the long-range oscillatory RKKY interaction,

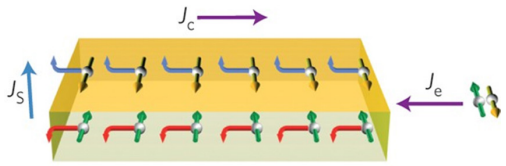

Figure 3.9: Illustration of the spin Hall effect. A spin current is generated by passing charge currents (adopted from Ref. [159]).

as also mentioned in Section 3.1.1. Due to the strong interlayer exchange coupling, the magnetic profile in one sublayer is the mirror image of the other, i.e. the position of the DWs in two sublayers is locked. In a typical SAF structure, Co/Ni/Co sublayers with PMA and a Ru spacer, coupled Néel-type DWs with the same chirality and width are stabilized (Fig. 3.10). Unlike the FM/HM case, an additional torque, known as the exchange coupling torque (ECT), is exerted on the DWs. This torque comes from the antiferromagnetic exchange coupling field and can be about an order of magnitude larger than the DMI field torque [163]. Therefore, this large torque is mainly responsible for the superfast DW motion in the SAF structure. The more identical the sublayers are (M_U, magnetization of the upper layer, and M_L, magnetization of the lower layer are closer to each other; M_R, remanent magnetization is smaller), the larger the torque is, resulting in a larger velocity (Fig. 3.11 b). In addition, unlike the FM case where the DW type also affects the motion behavior, in the SAF structure, up-down and down-up DWs show similar response to the IP longitudinal field, which can be explained by the symmetry in SAF structures (Fig. 3.11 c and d) [163]. Also, the DW in SAF racetracks is robust against the changes in local geometry due to the large ECT and the symmetric SAF structure, as demonstrated by our group's previous studies [164, 165]. In short, due to the elimination of stray fields, robustness against external fields, and highly efficient DW motion, the SAF structure is promising for the realization of high-capacity, high-performance, and low-energy-consumption RTM devices. Other complex spin textures, such as skyrmions, which may be more robust and efficient to manipulate, are also attractive for investigation and application.

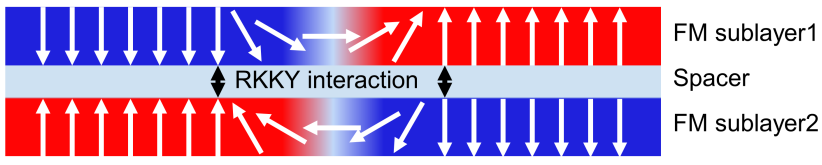

Figure 3.10: Illustration of a typical SAF structure. Two ferromagnetic sublayers are antiferromagnetically coupled via a spacer layer by the RKKY interaction. Coupled Néel-type DWs have the same DW width.

3.3 Domain wall motion in 3D structures

With the aforementioned developments in RTM (Fig. 3.7), devices are now efficient and robust. So, what is the next step? The 3D implementation of RTM is one possible di-

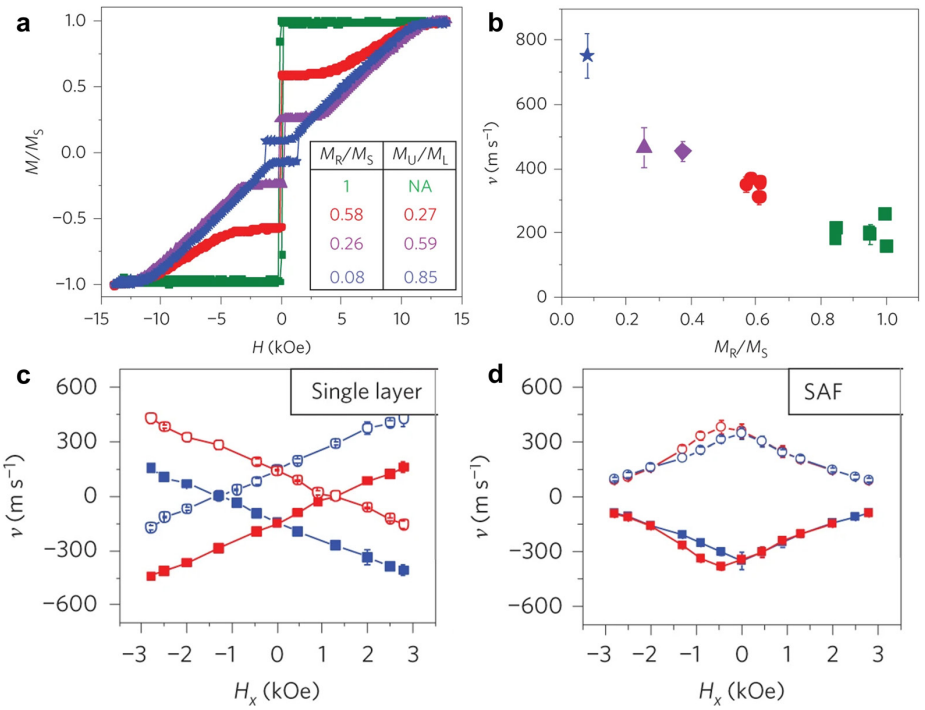

Figure 3.11: Current-induced DW motion in synthetic ferromagnetic and SAF structures. **a**, Normalized *M*-*H* hysteresis loops of samples with different remanent magnetizations (M_R). **b,** Maximum DW velocities in racetracks formed from samples with different M_R. Different colors correspond to different M_R, as shown in (**a**). **c,d,** Longitudinal field dependence of DW velocity in synthetic ferromagnetic (**c**) and SAF (**d**) structures. Figures are adopted from Ref. [163].

rection, as higher data density and more functionalities, such as tunable configuration, can be realized by utilizing the third dimension (Fig. 3.12 a) [143]. Several different methods have been proposed to fabricate 3D RTM devices, including ALD. ALD can form thin films with 3D structures because it ensures uniform deposition on the surfaces of 3D structures, such as trenches. Using $Co(PF_3)_4H$ as a precursor, Co thin films were deposited with PMA and the DW motion with a velocity of up to 10 m s^{-1} was demonstrated [166].

Another candidate is 3D nanowires, which can be prepared by electroplating in anodized alumina templates or by deposition on scaffolds built by 3D nanoprinting [167, 168]. 3D soft magnetic $Co_{30}Ni_{70}$ wires with a diameter of 90 nm can be obtained after selectively etching the porous anodized aluminum oxide templates (Fig. 3.12 b) [169]. These nanowires were then placed on Si wafers patterned with conductive pads. Current pulses were used to drive DWs in the nanowires. Here, the DW is a 3D Bloch-point wall. Interestingly, the DW velocity was found to be higher than the predicted value in these nanowires, which can be attributed to the topology of the DWs (Fig. 3.12 c and d). The current-induced Œrsted field facilitates the stabilization of Bloch-point walls with specific topology, overcoming the Walker breakdown in the dynamic response [167]. On the other hand, focused electron beam induced deposition was applied to fabricate 3D nonmagnetic structures and then permalloy was deposited on them by thermal evaporation to form a 3D magnetic conduit (Fig. 3.12 e and f) [21]. The magnetic properties were then char-

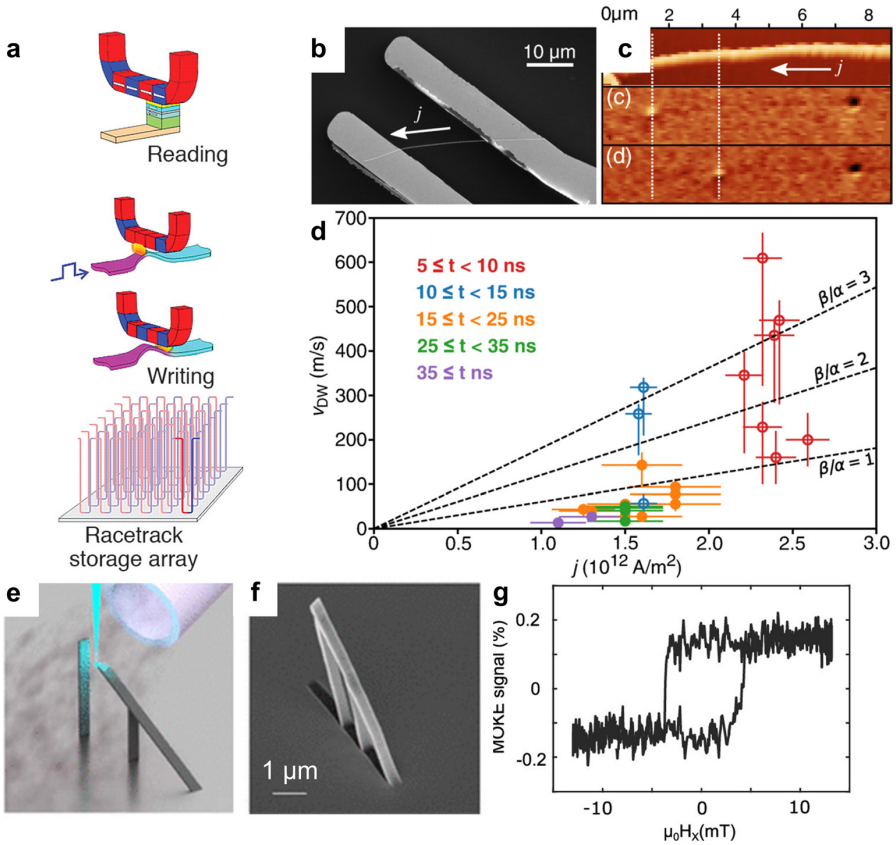

Figure 3.12: DW motion in 3D structures. **a,** Schematic of a 3D racetrack array and its reading and writing. Reading is done by an MTJ device, while writing is done e.g. by the fields of a DW moved in another nanowire (adopted from Ref. [143]). **b,** SEM image of a 3D $Co_{30}Ni_{70}$ nanowire with a diameter of 90 nm. **c,** AFM (top) and MFM (middle and bottom) images of the nanowire. The DW can be moved by a 5.8 ns current pulse ($J = 2.2 \times 10^{12} \mathrm{A/m^2}$), as shown in the comparison between the initial (middle) and final (bottom) states. **d,** DW velocity versus applied current density and duration. Dashed line is calculated from the one-dimensional model. (**b**-**d**) are adopted from Ref. [167]. **e,** Schematic of the fabrication of a 3D magnetic DW conduit by 3D printing. **f,** SEM image of a 3D magnetic conduit with 50 nm permalloy. **g,** *M*-*H* hysteresis loop measured by the dark-field magneto-optical Kerr effect setup. (**e**-**g**) are adopted from Ref. [168].

acterized by magneto-optical detection using a specific setup designed for 3D structures (Fig. 3.12 g) [168].

However, it is difficult to fabricate heterostructures in nanowires, which means that SAF structures cannot be realized in them, and then stray fields will hinder high-density integration. In addition, the manipulation of nanowires is cumbersome as compared to film deposition. As for ALD, although FM Co and Ni layers can be deposited, high quality interfaces and good thickness control, which are important for the RKKY interaction, remain difficult and require further work. In this thesis, by using freestanding heterostructures, we provide an alternative way to fabricate 3D RTM devices. Our methods combine the advantages of well-controlled film deposition with the simplicity of the freestanding technique.

Chapter 4

Experimental methods

In this chapter, I will briefly introduce the experimental methods used in this thesis. Generally, I will follow the order of the experiments, starting with thin film deposition, followed by characterizations such as X-ray diffraction, transport measurements, superconducting quantum interference device, Kerr microscopy, etc.

4.1 Pulsed laser deposition

PLD, also known as pulsed laser ablation, is a typical physical vapor deposition (PVD) method. Since the 1980s, high-power and highly reliable lasers have emerged and matured, providing a solid foundation for the application of lasers for deposition. In these years, PLD has been widely used to deposit thin films consisting of metals, oxides, nitrides and their multilayers or superlattices. The main advantage of PLD lies in the deposition of materials with complex components, such as $Pb(Zr_xTi_{1-x})O_3$ [170]. This is because the laser used in PLD has very high energy (typically > 1 J cm^{-2}), and the target can be instantaneously vaporized into a plasma with exactly the same composition as the target when this laser hits the target surface. The film formed by the migration of the plasma can then well replicate the composition of the target. In addition, it is also possible to tune the composition/vacancy of the samples since many parameters, including temperature and partial pressure, are adjustable over a wide range. In addition to thin films, PLD is also applied in the fabrication of other microstructures, e.g. nanotubes, quantum dots [171, 172].

Generally, the PLD process can be divided into the following three stages:

Interaction between target and laser pulses

PLD uses a high-power laser whose pulse width is often in the range of several nanoseconds. This laser beam can generate high power density when focused. It can then instantly heat part of the target to an extremely high temperature. The target material is then rapidly vaporized and ionized to form a high-density plasma. This plasma expands in a direction perpendicular to the target surface and diffuses to form a plume (Fig. 4.1 a). In this step, the interaction of the laser with the target material can determine the yield, composition, migration speed, etc.

Plasma propagation

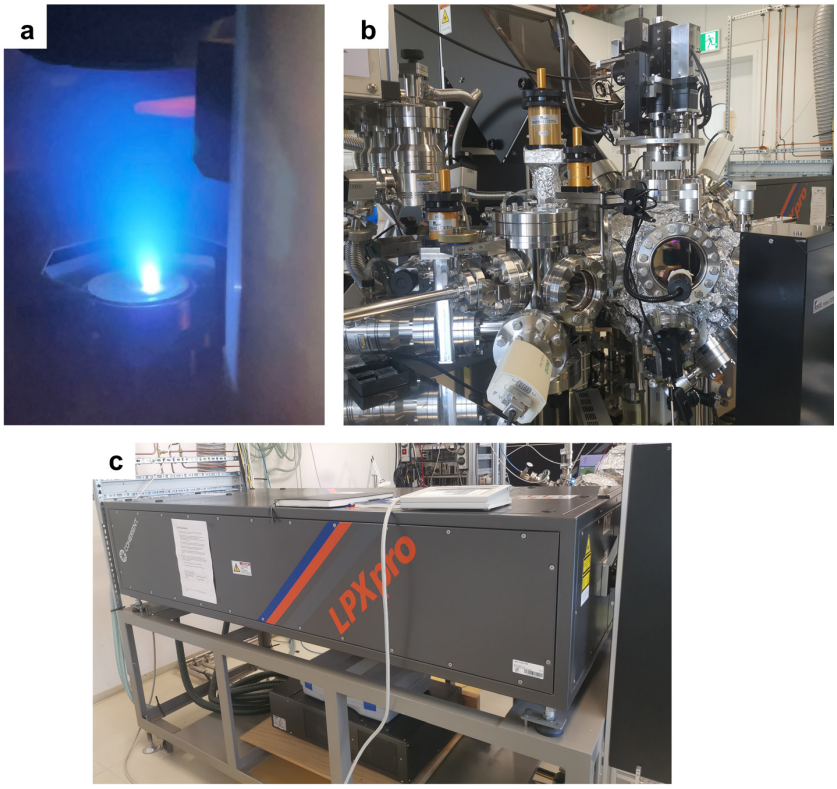

Figure 4.1: Pulsed laser deposition system. Photograph of a plasma plume (**a**), the load/lock chamber and main chamber (**b**), and the laser unit (**c**). To save space, multiple reflections are created in the light path.

The plasma formed by the ablated materials collides with and is scattered by the processing gas molecules in the chamber during diffusion. In this experiment, oxygen is used as the processing gas, but argon, hydrogen, nitrogen or other gases can also be used. Therefore, the partial pressure of the processing gas also plays an important role in the composition, kinetic energy and spatial distribution of the plasma plume, and thus affects the composition and structure of the deposited thin film.

Film formation on substrate

The formation of thin films from the ablated materials on the substrate's surface is a complex process. The energy of the plasma plume, the temperature of the substrate, and the affinity between the substrate and the ablator all affect the growth process, resulting in different growth modes and properties of the thin film.

Theoretically, a perfect substrate surface should be flat as a crystal plane, but the large-scale flat surface is energetically unstable. Therefore, the most ideal surface topography is step-and-terrace structure, which is often used for deposition. Usually, specific processes are required to obtain a step-and-terrace surface, such as annealing in oxygen at a high temperature or etching in a strong acid. Considering the ions moving on the surface, diffusion over the edges of the steps requires higher energy. The ions then form a film by bonding at lower energy points, i.e. edges or defects.

Generally, after propagation, the ions are adsorbed on the substrate's surface and subjected to 2D thermal motion, which shows four different growth modes: step-flow growth, layer growth, island growth or layer-island growth (Fig. 4.2) [173]. If the energy for thermal motion is insufficient, the ions may encounter other ions or clusters and nucleate on the surface before diffusing to the edge of the step. When the density of crystal nuclei on the surface is sufficiently high, the possibility of subsequent ions being captured by existing nuclei edges is greater than the formation of a new nucleus, and film formation begins. Interlayer transfer also affects the growth mode. If there is limited or no interlayer transfer, the subsequent ions will accumulate on the early formed nuclei, leading to 3D island growth. In another extreme case where the transfer is very fast, the ions at the top of the nuclei can be transferred to the edges to start 2D layer growth. These two growth modes often coexist in PLD, resulting in a layer-island growth mode.

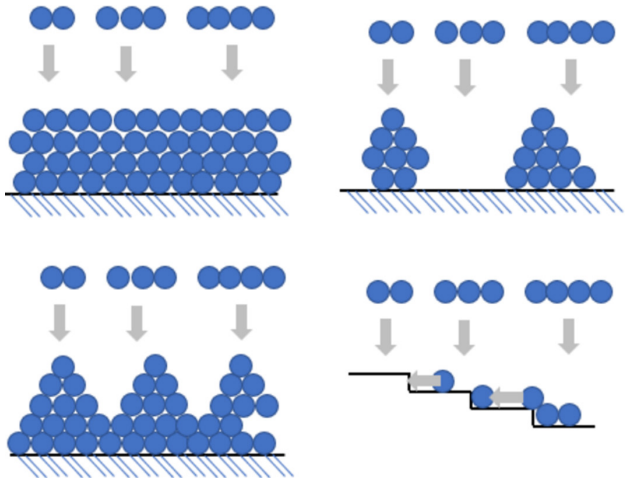

Figure 4.2: Schematic of thin film growth modes. Left top: layer growth, right top: island growth, left bottom: layer-island growth, right bottom: step-flow growth.

In short, the kinetic energy of the ions in 2D motion is the most important factor determining the growth mode. If this energy is insufficient to overcome the interlayer diffusion barrier, 3D island growth is favored, whereas if the energy exceeds the barrier, 2D layer growth is favored. And in 2D growth, if ion diffusion is sufficient and fast, step-flow growth is favored. Three parameters - substrate temperature, laser energy and collision loss of kinetic energy after diffusion - mainly determine the kinetic energy.

In general, one PLD system consists of a laser unit, an optical path, and a deposition chamber. In addition, the growth process can be monitored in situ by RHEED, and the vacuum in the main chamber can be maintained by incorporating a load/lock chamber. We have all these components in our PLD system, as shown in Fig. 4.1 b and c. A KrF excimer laser (248 nm) is used here. Precise deposition control can be achieved by adjusting the laser energy, pulse frequency, chamber pressure, substrate temperature, target-substrate distance, laser focus, etc. The base pressure of our main chamber can reach levels of 10^{-8} Torr, and the use of a heating laser allows rapid heating of the sub-

strate to above 800 °C within 20 minutes. All these advantages guarantee the high quality of deposited thin films.

4.2 Magnetron sputtering

Magnetron sputtering is another PVD technique. Similar to PLD (Section 4.1), sputtered atoms undergo thermal motion after propagation in a deposition chamber and form thin films on the substrate surface. The main difference between them is the mechanism used to generate the ions or atoms. In PLD, the ions are generated by a high-power pulsed laser, whereas magnetron sputtering uses a sputtering gas, usually an inert gas such as argon due to its high molecular weight, to sputter the atoms or ions from the target material at a high rate. In normal sputtering, electrons are generated and accelerated by a high voltage between the cathode - usually located behind the target - and the anode - usually an electrically grounded chamber. Afterwards, the electrons collide with the sputtering gas and ionize it. Finally, the positive sputtering gas ions can be accelerated toward the target and generate sputtered ions from target materials. This is usually used for sputtering conductive materials. To improve the etching rate and reduce the electron heating effect, magnetron sputtering uses magnetrons, which use strong electric and magnetic fields to confine the charged ions of the sputtering gas near the surface of the target. This requires a lower voltage and less sputtering gas than conventional sputtering, allowing the deposition of high-quality thin films with less contamination. In addition, radio frequency sputtering is often used to sputter insulators. In general, magnetron sputtering has many advantages, including high deposition rate, stable deposition process that is easy to handle, and large-area homogeneous deposition, which facilitates its wide application in industry. Various kinds of thin films used in microelectronics and optoelectronics are deposited by magnetron sputtering.

In this thesis, metal thin films, such as Pt, Co, Ni and Ru were deposited by magnetron sputtering in our ultra-high vacuum sputtering chamber (Fig. 4.3).

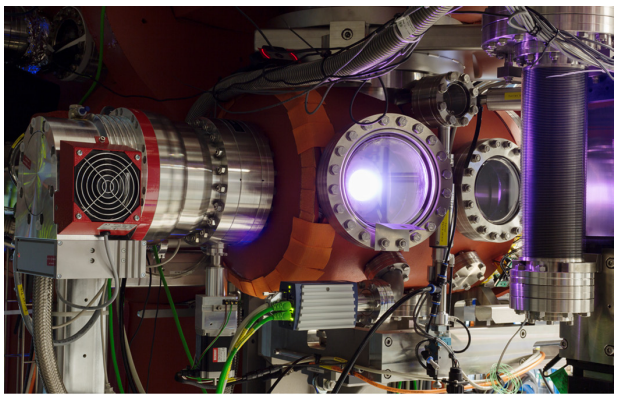

Figure 4.3: Ultra-high vacuum sputtering chamber. The purple light indicates the magnetron plasma.

4.3 Characterization methods

4.3.1 X-ray diffraction

XRD is a non-destructive method for characterizing the structure, chemical composition, and physical properties of materials. The wavelength of X-rays is in the similar order of molecules or unit cells, ensuring the possibility of scattering. In other words, crystal can act as a natural grating for X-rays. In this thesis, I mainly used XRD to analyze crystal structures, so I will mainly focus on the principles for this type of measurement.

According to X-rays, the refractive index for most materials is close to 1. To explain the diffraction caused by X-rays, Bragg proposed a simple but useful model. Assuming that the incident wave is reflected by parallel atomic planes in the crystal, where each atomic plane reflects only a small fraction of the radiation (usually $10^{-5} - 10^{-3}$ compared to the incident wave), high intensity can be reached because X-rays have sufficient penetration in materials. On the other hand, diffraction enhancement can be satisfied as described by the Bragg's formula [174]:

$$2\mathrm{d}\sin\theta = \mathrm{n}\lambda \tag{4.1}$$

Here, d is the plane spacing, and n is the diffraction order, as shown in Fig. 4.4. This formula is related to the lattice periodicity and provides only the diffraction enhancement condition, but lacks information about the diffraction intensity distribution.

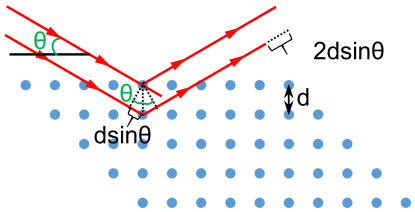

Figure 4.4: Diffraction in crystals. Diffraction enhancement can be satisfied when $2\mathrm{d}\sin\theta$ is equal to $\mathrm{n}\lambda$.

In fact, the XRD of crystals is mainly due to the interaction between electrons and X-rays. When a photon beam hits the crystal, photons jump to different energy levels due to scattering caused by electrons. Assuming that the scattering potential is proportional to the electron density, we can calculate the amplitude using the Born approximation, the far-field approximation, and neglecting magnetic scattering [175]:

$$u_{\boldsymbol{k}\to\boldsymbol{k}'} = c\int \mathrm{n}(\boldsymbol{r})e^{i(\boldsymbol{k}-\boldsymbol{k}')\cdot\boldsymbol{r}}\,\mathrm{d}\boldsymbol{r} \tag{4.2}$$

Here, $\boldsymbol{k}\to\boldsymbol{k}'$ is the scattering vector and $\mathrm{n}(\boldsymbol{r})$ is the electron density.

In this thesis, an XRD instrument designed by Bruker was used (Fig. 4.5 a). Cu radiation is used to generate X-rays and a Ge double crystal is applied as a monochromator to eliminate Cu $K_{\alpha 2}$ radiation. The average wavelength generated by the tube is 1.5418

Å, and the wavelength after the monochromator is 1.5406 Å. A stage that can move in 5 axes is used to mount samples (Fig. 4.5 b).

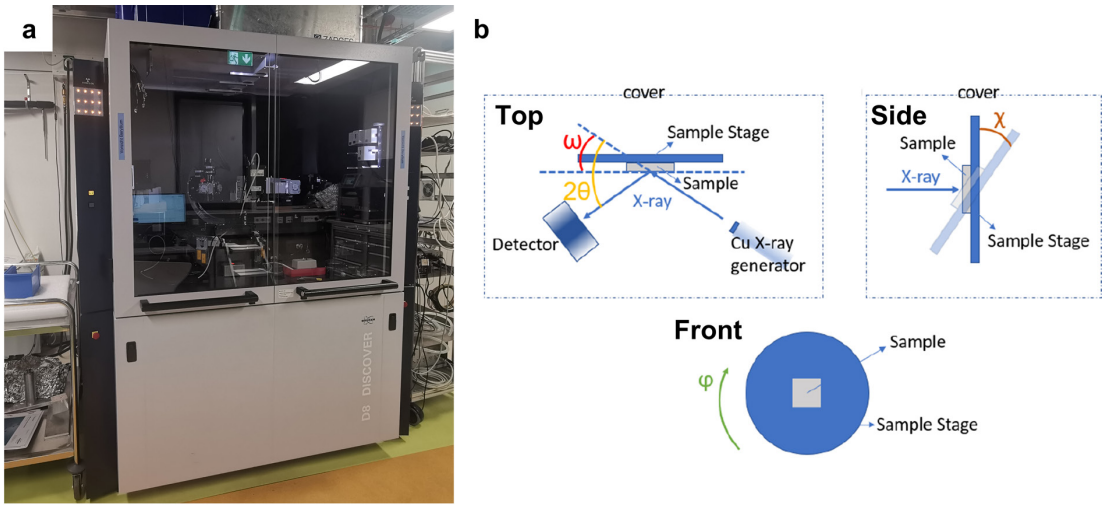

Figure 4.5: X-ray diffraction instrument. **a,** Bruker D8 XRD used in the experiment. **b,** Schematic images of the stage used in the instrument. The stage can move in 5 axes: x, y, z, φ and χ.

4.3.2 Atomic force microscopy

AFM is a type of scanning probe microscopy. It mainly consists of a micro-cantilever with a nanometer tip, a motion detector, a feedback loop for monitoring motion, a piezoelectric ceramic scanning stage, and an image acquisition, display, and processing system.

In general, AFM has three common modes: contact mode, non-contact mode, and tapping mode (Fig. 4.6 a-d). The differences between these three modes result from the interaction between the tip atom and the sample surface atom. The interaction between these two atoms is illustrated roughly in Fig. 4.6 a. In contact mode, the distance between the probe and the sample is very small, resulting in a repulsive force. Since the force-distance curve is quite sharp in this region, even a small change in distance can lead to a large change in atomic force. As the force acts on and deflects the micro-cantilever, the changes can be further amplified by shining a laser on the top of the cantilever. The resolution can reach 0.1 nm in this mode, but it may also cause possible mechanical damage to samples. On the other hand, the non-contact mode works in a similar way, but the force is mainly attractive force due to the relatively large working distance. This mode is non-destructive, but also not as sensitive as the contact mode since the slope of the attractive force-distance curve is not large. The tapping mode is similar to the contact mode, but the probe is vibrating at a fixed frequency during scanning. In this mode there is only a short contact, which ensures high resolution and less damage.

In this thesis, a Bruker Dimension Icon-PT AFM was used to characterize the topography of the samples, as shown in Fig. 4.6 e. In addition, according to the ScanAsyst^{TM}, a type of tapping mode called PeakForce Tapping is used in the system. In this mode, the

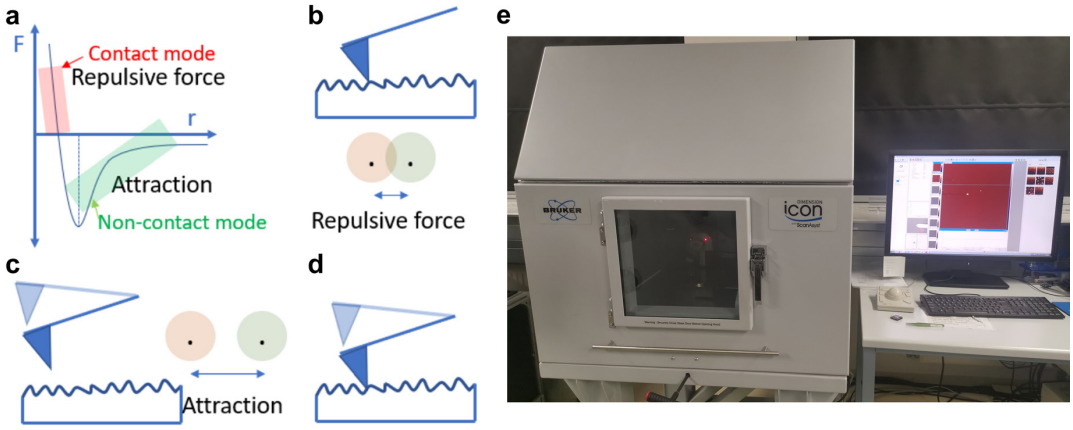

Figure 4.6: Atomic force microscopy. **a,** Atomic force versus distance curve. **b**-**d**, Three typical AFM operating modes: contact mode (**b**), non-contact mode (**c**), and tapping mode (**d**). **e,** Photograph of the Bruker Dimension Icon-PT AFM.

peak force can be kept as low as 10 pN, allowing for high quality non-destructive measurements.

4.3.3 Transport measurements

The transport properties of the samples were characterized in a Physical Property Measurement System (PPMS) (Fig. 4.7 a). PPMS is a low temperature, strong magnetic field measurement platform designed by Quantum Design to characterize magnetic, thermal and electrical properties of samples. It can operate in a wide temperature range of $1.8 \sim 400$ K and a wide magnetic field range of $0 \sim 9$ (or 14) T. Many properties can be measured in this system, such as resistivity, magnetoresistance, Hall coefficient, Seebeck coefficient, specific heat, etc. In addition, a rotator can be used in the system, which is particularly useful for characterizing the anisotropy of the sample (Fig. 4.7 b).

In this experiment, the transverse and longitudinal resistivities were measured in typical Hall devices (Fig. 4.7 c) using a four-probe method in a PPMS. A lock-in amplifier (AMETEK, 7270 DSP) was also used to obtain a better signal-to-noise ratio.

4.3.4 Superconducting quantum interference device based magnetometer

The magnetic properties of the samples were also characterized in our superconducting quantum interference device (SQUID, Quantum Design) (Fig. 4.8 a). SQUID is a sensitive magnetometer capable of detecting extremely small magnetic fields ($\sim 10^{-10}$ Oe). Its most important component is a superconducting loop that contains Josephson junctions (Fig. 4.8 b). When the magnetic flux threading the loop changes, a screening current will circulate the loop, which means that this current will have different directions in the upside and downside branches. Thus, a voltage can be generated if the current in either branch exceeds the critical current of Josephson junctions. It should be recognized that in radio frequency SQUID, only one Josephson junction is required and the resonant frequency of the tank circuit changes as the magnetic flux changes. In this thesis, magnetization

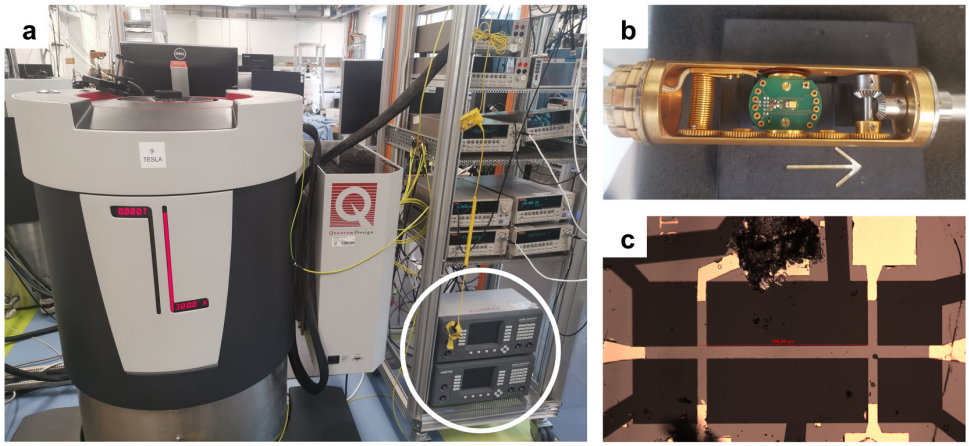

Figure 4.7: Physical Property Measurement System. **a,** Photograph of the 9 T PPMS. Right: Source Measure Units on the shelf. The white circle marks the lock-in amplifier used in the experiment. **b,** Photograph of the rotator. **c,** Optical image of a typical Hall device. Wires are bonded to the gold pads.

versus temperature (M-T) and magnetization versus field (M-H) curves were obtained by SQUID.

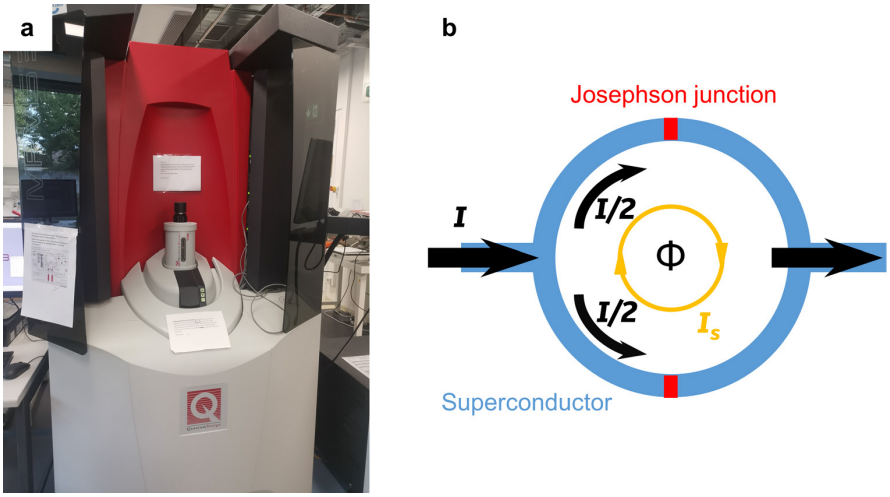

Figure 4.8: Superconducting quantum interference device based magnetometer. **a,** Photograph of the SQUID instrument. **b,** Schematic of a direct current SQUID. Φ represents the magnetic flux threading the loop. I_s is the screening current generated by the magnetic flux change.

4.3.5 Kerr microscopy

The Magneto-optic Kerr effect (MOKE) describes the changes in polarization and reflected intensity of light reflected from a magnetic surface. Similar to the Faraday effect, which describes changes in transmitted light passing through a magnetic material, the MOKE is due to the anisotropic permittivity, which can affect the speed of light in a medium. Kerr microscopy is based on the MOKE. The light first passes through a polarizer filter to produce polarized light, then reflects from the sample surface and passes through an analyzer that can convert the changes in light, such as Kerr rotation, Kerr el-

lipticity, or polarized amplitude, into changes in visible light intensity, and finally passes through a regular microscope. In addition, the direction of the sample magnetization determines the type of MOKE: when it is perpendicular to the reflecting surface, it is called polar MOKE; when it is parallel to the reflecting surface and in the incident plane, it is defined as longitudinal MOKE; when it is perpendicular to the incident plane and parallel to the reflecting surface, it is called transversal MOKE. Since the other two effects have no Kerr rotation when the light is perpendicular to the surface, near normal light is usually used to simplify the measurement for polar MOKE. The design of our Kerr microscopy setup follows the aforementioned principles, and a piezoelectric scanning stage is mounted to move the sample (Fig. 4.9 a).

Since different magnetic domains have different magnetizations, it is possible to distinguish these domains in Kerr microscopy. In our experiment, Kerr microscopy was mainly used to characterize DW behaviors, such as CIDWM. And the background images are always subtracted from the final images to get a better contrast for any magnetization change. In a typical DW motion measurement, a differential image is taken before each operation, and several nanosecond pulses of currents are injected to drive the DW, causing changes in contrast. These changes indicate the moving distance of the DW (Fig. 4.9 b). The velocity of DW is then calculated from the distances.

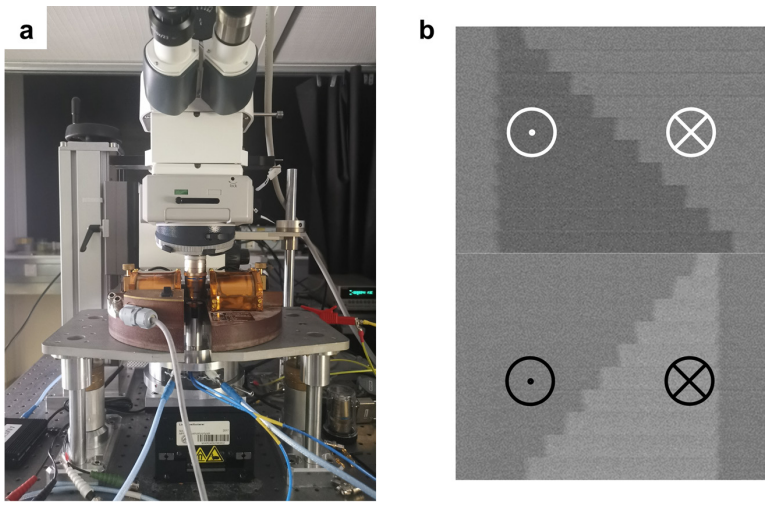

Figure 4.9: Kerr microscopy. **a,** Photograph of the Kerr microscopy setup. An in-plane magnet is used to generate the in-plane field. An out-of-plane field can be generated after changing the magnet. **b,** Typical differential Kerr images taken from a PMA sample. The bright and dark regions correspond to the down (⊗) and up (⊙) domains. The DW has moved from left to right in the top image and vice versa in the bottom image.

4.3.6 Scanning electron microscopy and focused ion beam milling

A typical SEM uses an electron beam with the energy ranging from 0.2 keV to 40 keV. The electron beam are required to be focused by condenser lenses to achieve a small spot size. The beam is then deflected by scanning coils, which allows raster scanning of the sample surface. Thus, unlike a normal camera using optics, the resolution is not limited

by the diffraction limit, but by the size of the electron spot and the size of the interaction volume in the material, and can reach ~ 1 nm. This resolution is much better than that of an optical microscope, but is still not enough to image atoms (~ 0.1 nm).

When the electron beam hits the sample surface, secondary electrons, backscattered electrons and many other signals, such as X-rays, Auger electrons, luminescent light, etc. are produced. These signals can be further detected and amplified by specific detectors to analyze the structure and properties of the material. However, it is difficult to assemble a SEM with all these detectors. The most common signal used in SEMs is secondary electrons, which are ejected from atoms in the sample by inelastic scattering with the beam electrons. Because the energy of secondary electrons is very low, often < 50 eV, they have a small mean free path in solids, i.e. only secondary electrons generated near the surface (usually a few nanometers from the top) can be ejected from the surface and then detected. Therefore, secondary electrons are commonly used to obtain surface information of samples. In addition, SEM images have a large depth of field because the beam spot is quite small. On the other hand, backscattered electrons, which are ejected by elastic scattering and are strongly related to the atomic number of the sample, and X-rays are often used to characterize the composition of the sample.

Apart from the electron beam source, high current density ion beams, such as Ar^+ or Ga^+, are often assembled in the system to form a dual-beam system. These focused ion beams (FIBs) can generate secondary electrons and secondary ions, but the most common application is etching and polishing of samples, such as for transmission electron microscopy (TEM) specimen preparation. In addition, ion beam induced deposition can also be used to deposit materials including tungsten.

In this thesis, both SEM and FIB were used (Fig. 4.10). SEM was used to image 3D structures and FIB was used to prepare cross-sectional lamellae.

Figure 4.10: Photograph of the scanning electron microscope (left, JSM-7500F) and the focused ion beam system (right, FEI) used in this thesis.

4.3.7 Transmission electron microscopy

Different from SEM, which often uses secondary electrons for imaging, TEM imaging is based on transmission electrons. While SEM can characterize samples of any size, TEM, especially high resolution TEM, requires thin samples (< 100 nm) to obtain sufficient transmission signals. Similar to SEM, these signals are then collected and converted into images. Many parameters of the sample, such as thickness, density, crystal structure, atomic number, etc., can affect the contrast of TEM images, so TEM can be used to analyze all of these information. On the other hand, TEM collects different types of signals in different working modes. For example, the energy loss of transmission electrons can be used to analyze the composition of the sample in electron energy loss spectroscopy. In addition, TEM can also operate in a scanning mode, known as scanning TEM imaging, which is particularly useful for imaging atoms. In short, TEM is a high-end microscopy technique with a spatial resolution often around 0.1 nm and capable of many in-situ experiments, such as applying current or tuning temperature with custom TEM chips. In our experiment, the cross-sectional TEM images were obtained with our TEM (JEOL, JEM-F200) at an accelerating voltage of 200 kV (Fig. 4.11).

Figure 4.11: Photograph of a transmission electron microscopy system (JEOL, JEM-F200).

4.4 Device fabrication

In general, a device fabrication process consists of the following 4 steps: spin-coating resist, exposure, development, and etching (or deposition). First, the negative or positive resist is dropped onto the surface of the sample, and then the sample is rotated at several thousand rpm to form a homogeneous thin film on the surface (Fig. 4.12 a). Besides, baking is usually required to remove additional solvents. Afterwards, an electron beam or laser is used to expose the resist film in the desired area (Fig. 4.12 b). This changes the structure and solubility of the resist, making it soluble (positive resists) or insoluble (negative resists) in the developer. In the third step, the sample is immersed in the de-

veloper for a few tens of seconds and rinsed in the stopper (Fig. 4.12 c). Sometimes, a post-baking process is added before development to facilitate the structural changes in the resist. Finally, etching or deposition is used, and after removal of residual resists, devices can be fabricated (Fig. 4.12 d). In this thesis, devices for DW motion measurements were fabricated by photolithography and Hall-bar devices were fabricated by photolithography and electron beam lithography (EBL).

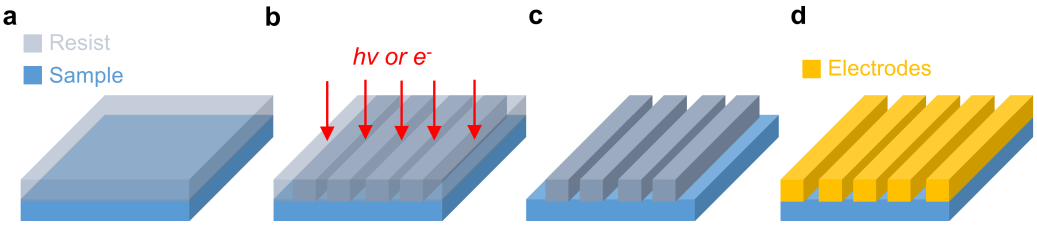

Figure 4.12: Schematic of the device fabrication process by lithography. **a,** Coating the sample with the resist. **b,** Exposure with laser or electron beam. Changes in transparency indicate the structural change. **c,** Development. **d,** Deposition of electrodes and removal of residual resists. Here, we use deposition as an example, while etching can remove the material in the area without protective capping.

Chapter 5

CIDWM in freestanding PMA multilayers

As discussed in previous chapters, RTM is a promising candidate for next-generation memory devices, and freestanding technique offers new possibilities for devices. In this chapter, I will combine these two distinct areas and present results in freestanding PMA multilayers.

It should be noted that some of the figures used in this chapter and the next chapter (Chapter 6) are reprinted from our paper [176], for which I am the first and corresponding author.

5.1 Thin film growth

We deposited SAO(200)/MgO(100) bilayer samples in our PLD chamber which is mentioned in Section 4.1 (all units in Å). The oxygen partial pressure was kept at 2×10^{-6} Torr and the laser repetition frequency was 2 Hz for the deposition of both layers. The temperature and laser fluence were 750 °C and 0.7 $\mathrm{J\,cm^{-2}}$ for SAO and 700 °C and 1.7 $\mathrm{J\,cm^{-2}}$ for MgO, respectively. MgO single crystal was used as the target, while the SAO target was prepared from stoichiometric powders of α-Al_2O_3 and $SrCO_3$. First, the powders were manually mixed with an agate mortar and pestle for 1 h and then calcinated at 1100 °C for 24 h. The calcinated powders were crushed and ground for 1 h to form a pellet. Finally, after sintering for 12 h at 1350 °C in a box furnace in air, we obtained the target. All samples were deposited on STO (001) substrates, which were annealed at 1050 °C in air to obtain better surfaces. RHEED was used to monitor the entire growth. As shown in Fig. 5.1 a and b, clear line-type RHEED patterns were observed, indicating a flat surface and good crystallinity of the as-deposited SAO/MgO thin film. In addition, RHEED oscillations were found during SAO deposition (Fig. 5.1 c), indicating that the SAO thin film was grown layer by layer. In this way, precise thickness control can be achieved. However, this kind of oscillations was not present during MgO growth, and the lines in RHEED pattern are also slightly broader for MgO. This is mainly because the lattice mismatch between MgO (4.21 Å) and SAO (1/4 SAO = 3.96 Å) is a bit large,

resulting in a large strain. Although layer-by-layer growth is difficult to achieve in MgO, 2D layer growth still dominates the growth since there is no additional dot in the RHEED pattern.

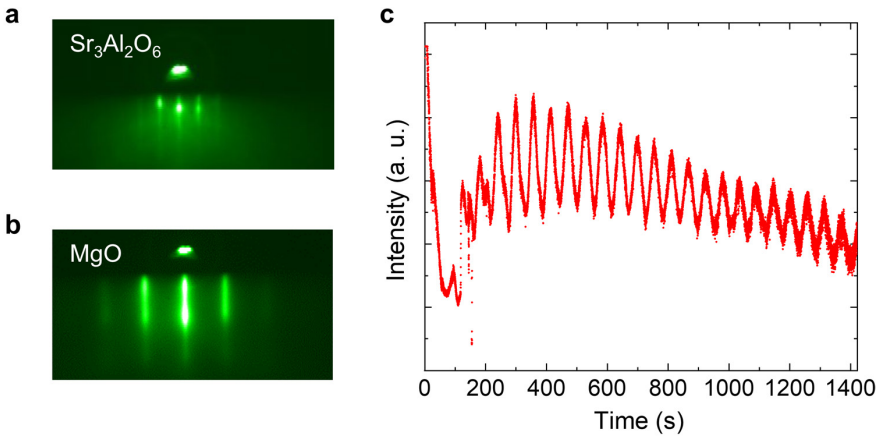

Figure 5.1: Reflection high energy electron diffraction during deposition. **a,b,** RHEED patterns taken after growth of $Sr_3Al_2O_6$ (**a**) and MgO (**b**) layers. **c,** RHEED oscillations show the entire growth of a 20 nm $Sr_3Al_2O_6$ layer on the $SrTiO_3$ (001) substrate. The laser repetition rate was 2 Hz.

The quality of the thin films was then characterized by AFM and XRD. As shown in Fig. 5.2 a and b, the root mean square (RMS) roughness of both SAO and SAO/MgO is very small, indicating that smooth surfaces were achieved in the deposition of both MgO and SAO. The surface of SAO shows a clear step-and-terrace structure, again confirming layer-by-layer growth. As shown in the XRD θ-2θ pattern of the bi-layer, clear (004), (008) and (0012) peaks of SAO and (002) peak of MgO are found without any additional peak, indicating good crystallinity of our epitaxial thin films (Fig. 5.2 c). Since the crystallinity and thickness of SAO are important for the lift-off and transfer process (Section 2.3), we further characterized the SAO layer by TEM. Cross-sectional TEM images show a sharp interface between SAO and YBCO capping, and clear lattices indicate the good crystallinity with limited defects, as shown in Fig. 5.2 d. In addition, the thickness ($\sim$ 20 nm) is consistent with that calculated from laser pulse amounts and RHEED oscillations. All these results guarantee a good quality of the as-deposited bilayers, facilitating subsequent deposition and lift-off.

We then deposited Pt(50)/Co(3)/Ni(7)/Co(3) with a TaN(30) capping layer by magnetron sputtering (Section 4.2) on our bilayer samples (all units in Å). These HM/FM heterostructures deposited on oxides are hereafter defined as the as-deposited multilayers. As discussed in Section 2.3, due to the existence of MgO capping, it was possible to transfer the bilayer samples ex-situ from our PLD chamber to the sputtering chamber. The bilayer samples were then annealed at 600 °C for 30 min in our ultra-high vacuum sputtering chamber. Finally, the HM/FM heterostructures were deposited at room temperature. Here, high vacuum and room temperature ensure good thickness and quality control. We also characterized the as-deposited multilayers by AFM and XRD. As shown in Fig. 5.3 a, a smooth surface with an RMS roughness of 0.278 nm was obtained. A

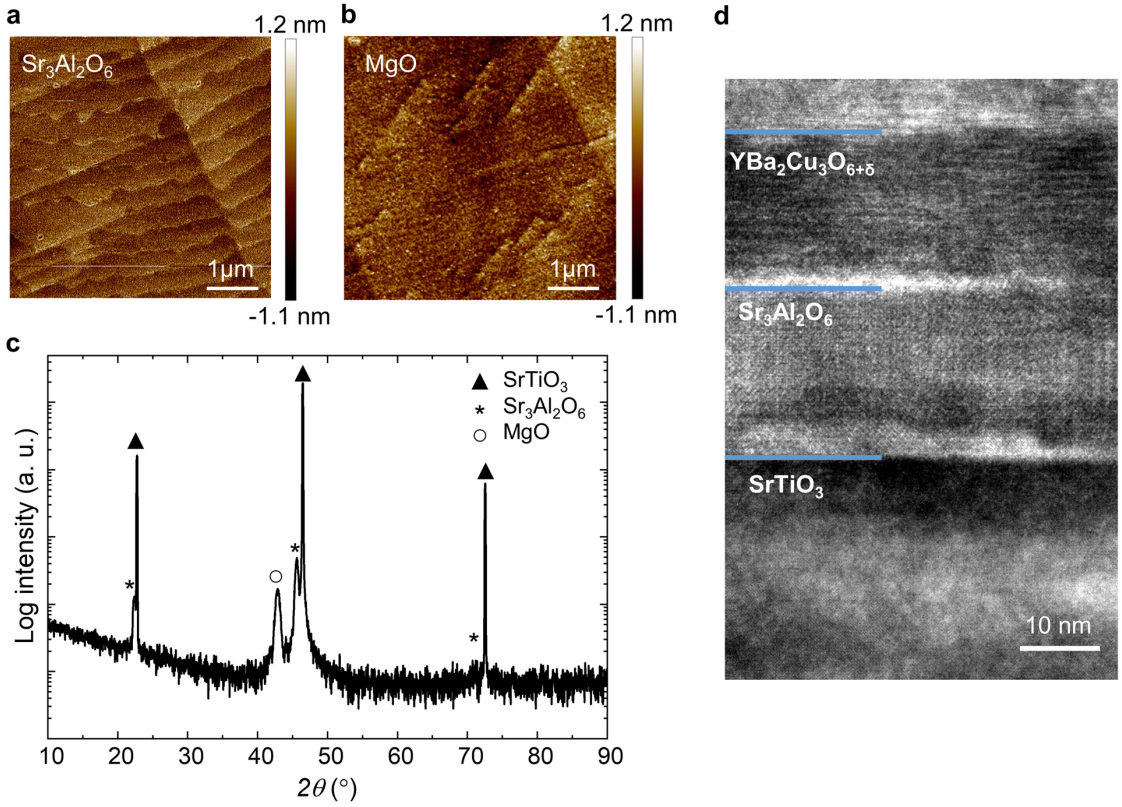

Figure 5.2: Deposition of $Sr_3Al_2O_6$ and MgO. **a,b,** AFM images of the as-deposited $Sr_3Al_2O_6$ thin film (**a**) and $Sr_3Al_2O_6$/MgO bilayer (**b**). The root mean square roughness values in **a** and **b** are 0.610 nm and 0.287 nm, respectively. **c,** Out-of-plane θ–2θ XRD pattern of SAO/MgO. **d,** Cross-sectional TEM image of SAO/YBCO deposited as a reference.

diffraction peak of the face-centered cubic (111) - oriented Pt layer can be clearly seen in the XRD pattern, while other layers are too thin to produce enough intensity to be detected by our XRD (Fig. 5.3 b). This (111) - oriented Pt layer guarantees a strong OOP magnetization of the FM layer. In short, the analysis of the surface and crystal structure of our deposited thin films indicates a high quality deposition of these layers.

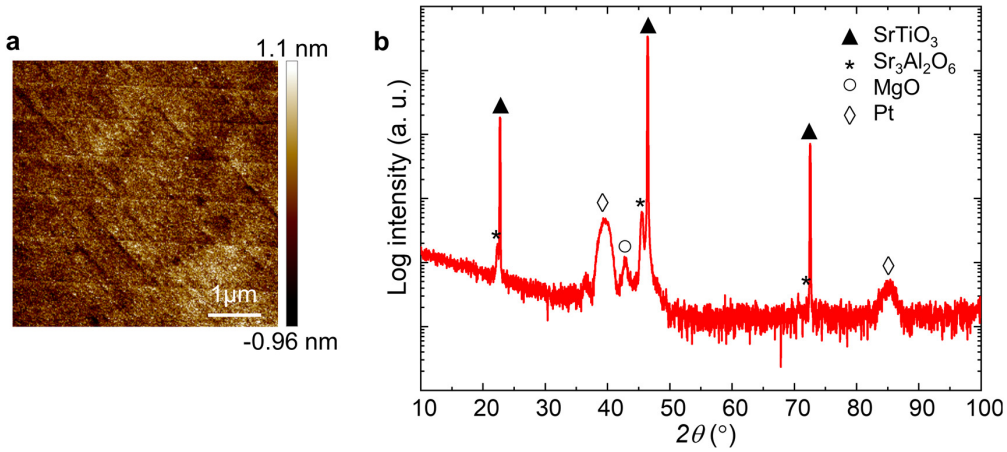

Figure 5.3: Deposition of Pt/Co/Ni/Co on $Sr_3Al_2O_6$/MgO. **a,b,** AFM image (**a**) and out-of-plane θ–2θ XRD pattern (**b**) of the as-deposited multilayer ($Sr_3Al_2O_6$/MgO/Pt/Co/Ni/Co/TaN). The root mean square roughness in **a** is 0.278 nm.

5.2 Lift-off and transfer of HM/FM heterostructures

As we discussed in Section 2.4, a water membrane based lift-off and transfer method was used to obtain freestanding heterostructures. As schematically illustrated in Fig. 5.4, a thin PMMA protection layer of about 100 nm thickness is first spin-coated onto the as-deposited multilayers. The sample is then immersed in deionized water for around 30 min to completely remove the SAO sacrificial buffer layer. The HM/FM heterostructures with MgO buffer can then be separated from the STO substrate by dipping the entire structure in water for a second time and transferred onto other bases together with water. Here, a sapphire substrate is used as the base. This transferred sample is hereafter defined as the freestanding sample. Also, we checked the surface morphology and crystallinity of the freestanding sample. As shown in Fig. 5.5 a, the diffraction peaks originating from the (111) - oriented Pt layer and MgO layer are clearly visible in the freestanding sample, while the peaks of SAO have disappeared, indicating a successful transfer of the freestanding sample with good PMA (we will confirm this again in the next section). In addition, it is possible to transfer a large-size freestanding sample whose area is more than 3×3 mm^2 (Fig. 5.5 a, inset), which is particularly useful for subsequent device fabrication and measurements, such as CIDWM measurement. On the other hand, the RMS roughness of the as-deposited and freestanding samples are found to be nearly identical (Fig. 5.3 a and 5.5 b), indicating the robustness of the multilayers throughout the process. Both XRD and AFM indicate no degradation in film quality during the lift-off and transfer

process, which is commensurate with the transport and magnetic property measurements (Section 5.3).

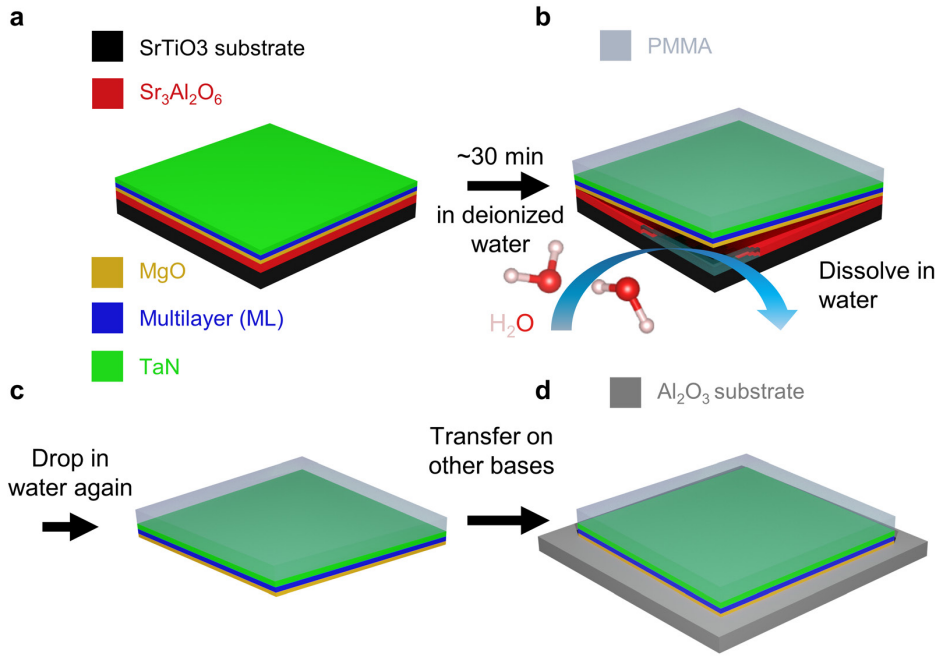

Figure 5.4: Fabrication of freestanding multilayers by the water membrane based method. **a,** Deposition of a $Sr_3Al_2O_6$/MgO/Pt/Co/Ni/Co epitaxial multilayer on a SrTiO3 (001) substrate with TaN capping. **b,** Immersion of the as-deposited film in deionized water for 30 min to remove the sacrificial layer after spin-coating PMMA. **c,** Separation of a freestanding multilayer (MgO/Pt/Co/Ni/Co/TaN). **d,** Transfer of the freestanding multilayer onto a sapphire substrate.

5.3 Transport and magnetization measurements

We then characterized the transport and magnetic properties of the freestanding samples and compared them with the as-deposited multilayers. As shown in Fig. 5.6 a and b, the *M*-*H* loops clearly show the PMA of both samples at room temperature, since the hysteresis can be clearly seen in the OOP loops and the hard axis is found to be IP. As summarized in Table 5.1, the saturation magnetization M_s and coercive field H_c of the as-deposited multilayers and freestanding samples were demermined from the OOP *M*-*H* curves, while the effective uniaxial anisotropy field H_K was determined from the IP *M*-*H* curves. It should be recognized that the curves were plotted after normalization. And the effective uniaxial magnetic anisotropy constant K_u^{eff} was calculated from Eq. 3.6, as we discussed in Section 3.1.2. In addition, it can be clearly seen from the *M*-*T* curves that the Curie temperature of both cases is above 400 °C, which facilitates further room temperature RTM applications (Fig. 5.6 c and d). All of these magnetic properties show similar values in the two samples, indicating that the magnetic properties are maintained throughout the lift-off and transfer process.

The freestanding and as-deposited multilayers were then patterned by photolithography (Secition 4.4) into Hall-bar devices with a channel width of 20 µm for transport

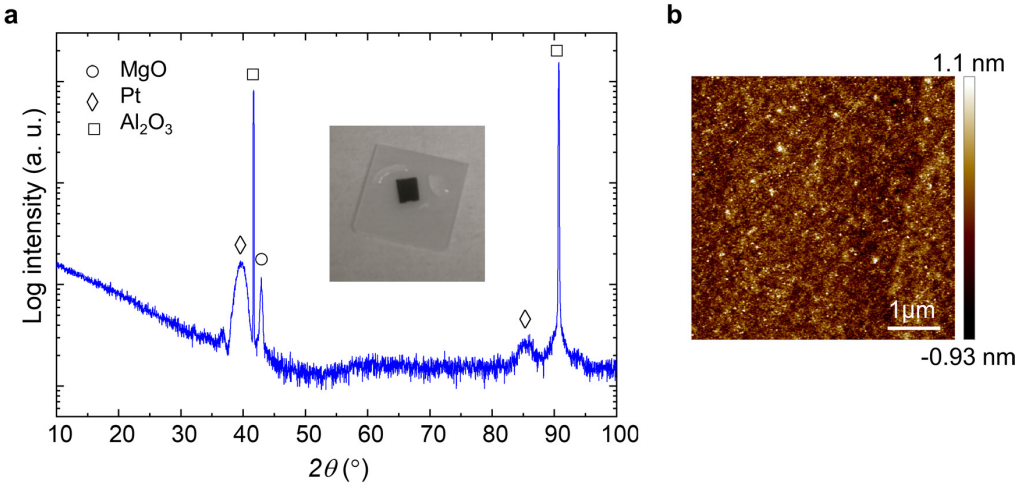

Figure 5.5: Transfer of freestanding HM/FM multilayers. **a,b,** Out-of-plane θ–2θ XRD pattern (**a**) and AFM image (**b**) of a freestanding multilayer (MgO/Pt/Co/Ni/Co/TaN) transferred onto a sapphire substrate. The root mean square roughness is 0.280 nm. The inset in **a** shows a freestanding multilayer on a 10×10 mm^2 sapphire substrate.

Table 5.1: Comparison of magnetic properties of as-deposited thin films and freestanding samples.

	H_{DMI} (Oe)	H_{c} (Oe)	H_K (Oe)	M_{s} (emu cm^{-3})	K_u^{eff} (erg cm^{-3})	Δ (nm)	D (erg cm^{-2})
As-deposited	1059.08 $\pm$ 65.96	64.86	8260	820	3.39×10^6	5.43	0.47 ± 0.03
Freestanding	1007.86 $\pm$ 28.59	77.43	8604	840	3.61×10^6	5.26	0.44 ± 0.01

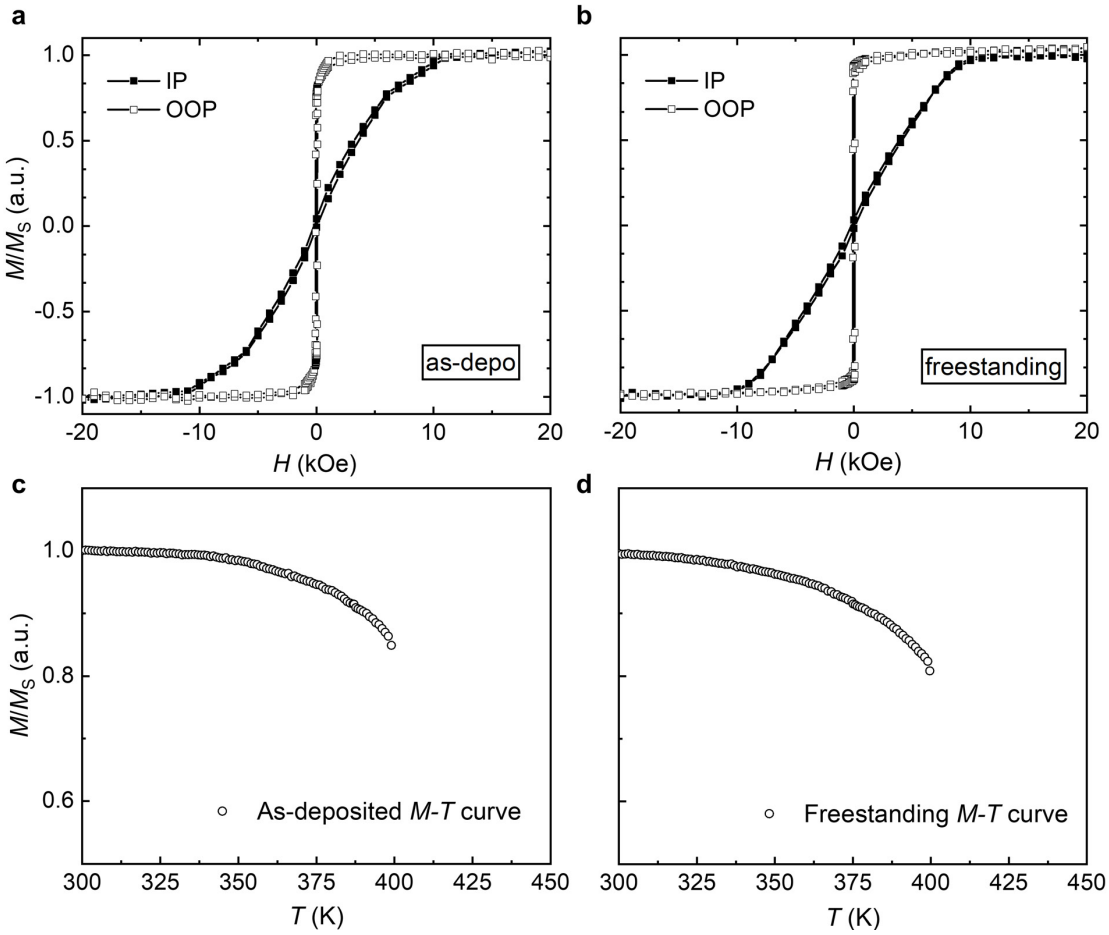

Figure 5.6: Magnetic properties of as-deposited and freestanding HM/FM heterostructures. **a,b,** In-plane (IP, filled square) and out-of-plane (OOP, open square) magnetization (M)/saturation magnetization (M_s) versus magnetic field (H) curves of an as-deposited HM/FM sample (**a**) and a freestanding HM/FM sample transferred onto a sapphire substrate (**b**) measured by SQUID at room temperature. M_s is the average magnetization at high field. **c,d,** Magnetization versus temperature (T) curves of as-deposited (**c**) and freestanding (**d**) multilayers measured by SQUID after a field cooling process ($H = 3$ T).

measurements. It is noteworthy that a 100 nm PMMA layer was spin-coated on the as-deposited multilayer as a capping layer, since the development and rinsing process involves water or a water solution, which can dissolve SAO. After exposure and development, this layer (exposed region for positive photoresist) was removed by oxygen plasma. Ar-ion milling was then used to fabricate the devices. As schematically illustrated in Fig. 5.7 a, the Hall conductance was measured with current injected along the x-axis, while the applied external magnetic field of 3 T (above M_s) was rotated in the x-y, x-z, and y-z planes. It should be noted that the signal we measured is always voltage, and then the resistivity can be determined from the voltage. The conductivity is then calculated from the resistivity as they are the inverse matrix of each other. The dependence of the Hall conductivity σ_{xy} on the applied field shows almost identical behavior in the as-deposited multilayer and freestanding sample (Fig. 5.7 b-d), which is in good agreement with the magnetization measurements. We also observed a slight difference between the two samples in the longitudinal resistivity ρ_{xx} versus temperature ($\rho - T$) curves (Fig. 5.8), which can attribute to the strain release in the freestanding sample. In addition, it can be clearly seen from the $\rho - T$ curves that ρ is proportional to T above low temperature, indicating good metallicity of both samples. We also measured hysteresis loops of σ_{xy} at different temperatures with varying OOP field, as summarized in Fig. 5.9. Similar hysteresis loops with sharp switching again demonstrate the good PMA in our samples. When the Hall conductivity σ_{xy} is plotted versus the longitudinal conductivity σ_{xx} (Fig. 5.10), we find a linear dependence, which is a typical characteristic of the extrinsic origin of the Hall signal. At low temperature (10 K), where the value of σ_{xy} is relatively high, we can clearly see a deviation from the linear fit. This is because the intrinsic contribution of the Hall conductance begins to dominate [177]. In short, all of these measurements show similar behavior in the as-deposited multilayer and in the freestanding sample, indicating that the film quality remains largely intact throughout the process, including lift-off, transfer, and device fabrication. This in turn results in almost identical CIDWM behavior in both samples.

5.4 CIDWM in freestanding HM/FM heterostructures

After the lift-off process, the freestanding sample was transferred onto a sapphire substrate and the polymer protective layer was then removed in acetone with soft ultrasonic cleaning (Fig. 5.11 a). As illustrated in Fig. 5.11 b, RTM devices were then fabricated using photolithography and Ar-ion milling in a manner similar to Hall-bar devices. A typical RTM device consists of a straight wire that is 50 μm long and 3 μm wide, and two bonding pads for connecting wires. Fig. 5.11 c shows an optical photo of an RTM device taken by an optical microscope with a 20× objective lens (Zeiss, Axiotron). The CIDWM in the RTM devices was then measured in both as-deposited multilayers and freestanding samples using Kerr microscopy (Section 4.3.5). The DW motion distance was determined by comparing the differential Kerr images before and after the injection of current pulses

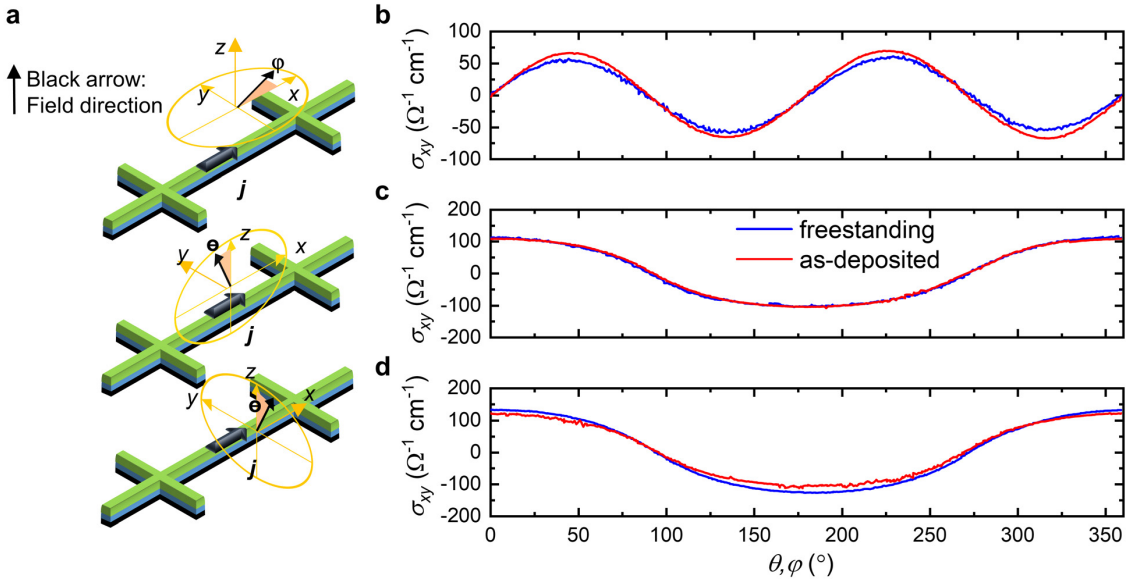

Figure 5.7: Hall conductivity of as-deposited and freestanding HM/FM heterostructures. **a,** Schematic of the transport measurement geometry. **b**-**d**, Hall conductivity (σ_{xy}) in freestanding and as-deposited multilayers as a function of magnetic field azimuthal and polar angles (φ, θ) defined in **a**, measured by PPMS at room temperature.

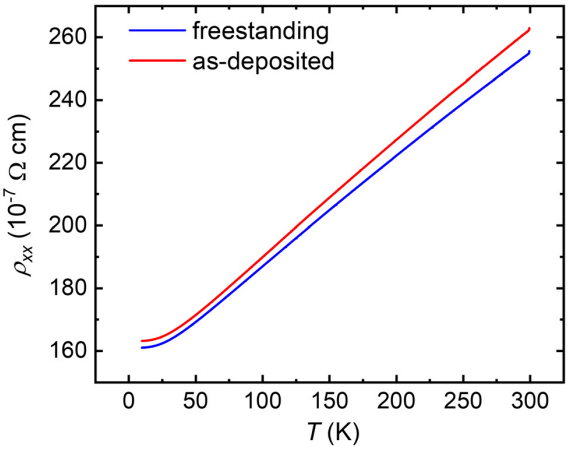

Figure 5.8: Longitudinal resistivity versus temperature of as-deposited and freestanding HM/FM heterostructures.

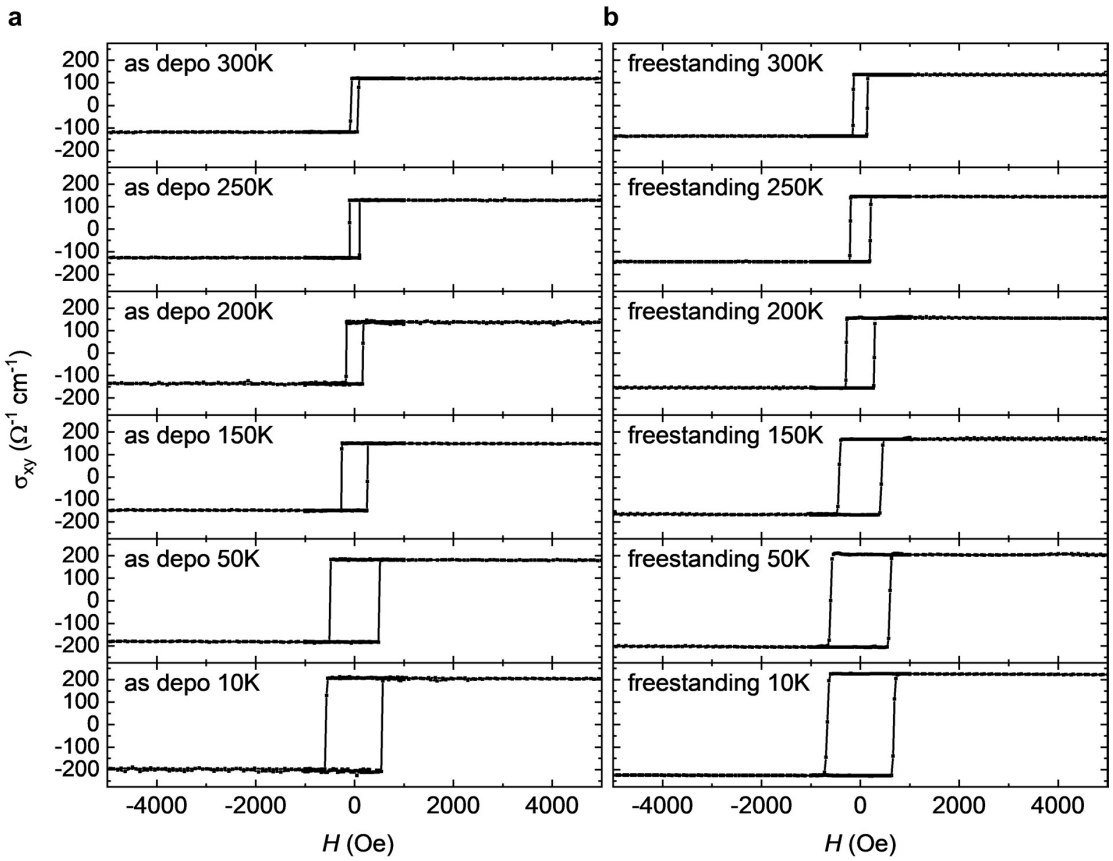

Figure 5.9: Hall conductivity of as-deposited and freestanding HM/FM heterostructures at different temperatures. **a,b,** Hall conductivity versus magnetic field, shown from top to bottom, measured at 300 K, 250 K, 200 K, 150 K, 50 K, and 10 K of as-deposited (**a**) and freestanding samples (**b**).

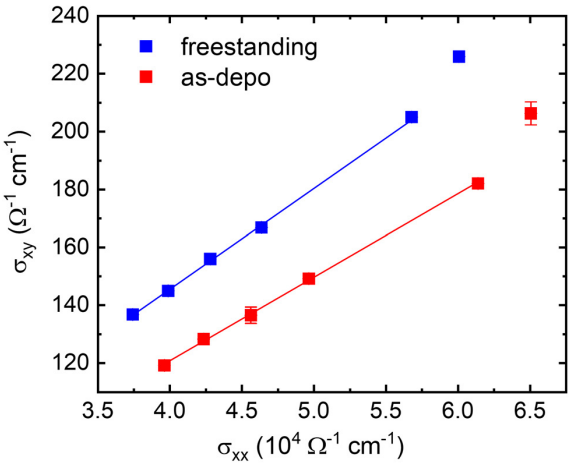

Figure 5.10: Hall conductivity versus longitudinal conductivity of freestanding and as-deposited HM/FM heterostructures. The blue and red lines here are linear fits of Hall conductivity σ_{xy} versus longitudinal conductivity σ_{xx} for freestanding and as-deposited samples, respectively. In these two cases, the fitted line has a slope equal to 0.0035 ± 0.0001 (freestanding sample) and 0.0029 ± 0.0001 (as-deposited sample). The slope is the physical coefficient related to the extrinsic contribution of the skew scattering mechanism. The low temperature (10 K) data are excluded from the fits.

with a temporal length of 10 ns. The velocity was then calculated by dividing the motion distance by the total current pulse length (10 ns multiplied by the pulse amount). Note that the interval between two pulses was set to about one hundred milliseconds to avoid overheating.

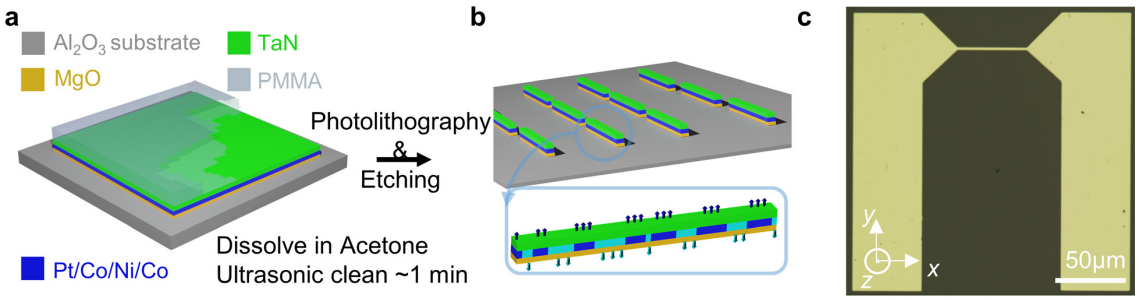

Figure 5.11: RTM device fabrication from freestanding HM/FM heterostructures. **a,** Protective PMMA is removed. **b,** Schematic of device fabrication from a freestanding HM/FM heterostructure. The cyan and blue colors correspond to down- and up-magnetized domains, respectively. **c,** Optical image of a typical racetrack. The device consists of a nanowire (length, 50 μm; width, 3 μm) and two bonding pads. DW motion and current direction are along the x-axis.

The calculated DW velocity of both cases is plotted against the injected current density (Fig. 5.12 a). Similar to the findings from the transport and magnetization measurements discussed in the previous section, almost identical CIDWM curves are observed before and after the transfer process. The only difference is found in the high-current-density region, where thermal nucleation of multi-domains takes place more readily in the as-deposited multilayers compared to the freestanding samples. This is because the oxygen plasma used to remove the capping PMMA (Section 5.3) can create more defects and increase edge roughness compared to ion milling process, and these edges can be more prone to multi-domain formation. In short, fast SOT-driven CIDWM with a velocity up to 200 m s^{-1} was realized in the freestanding sample, which is useful for the design of novel RTM devices.

We also characterized the longitudinal field dependence of the CIDWM in both samples at a given current density, which is $J = 1.82 \times 10^8$ A cm^{-2} for the as-deposited sample and $J = 2.33 \times 10^8$ A cm^{-2} for the freestanding sample, as shown in Fig. 5.12 b. As discussed in Section 3.2.2, the DMI effective field H_{DMI} can be determined from the linear fits of these curves, as summarized in Table 1. As discussed in Chapter 3, the DW width was calculated using Eq. 3.8, with the exchange stiffness A = 1.0 μerg cm^{-1} [178]. The DMI constant was then determined from [156]:

$$D = \Delta \mu_0 H_{\mathrm{DMI}} M_{\mathrm{s}} \tag{5.1}$$

All these magnetic properties of the as-deposited multilayer and the freestanding sample are compared in Table 5.1, demonstrating a high degree of consistency. This similarity explains their similar device performance. In addition, it should be noted that all given standard deviations come from multiple measurements.

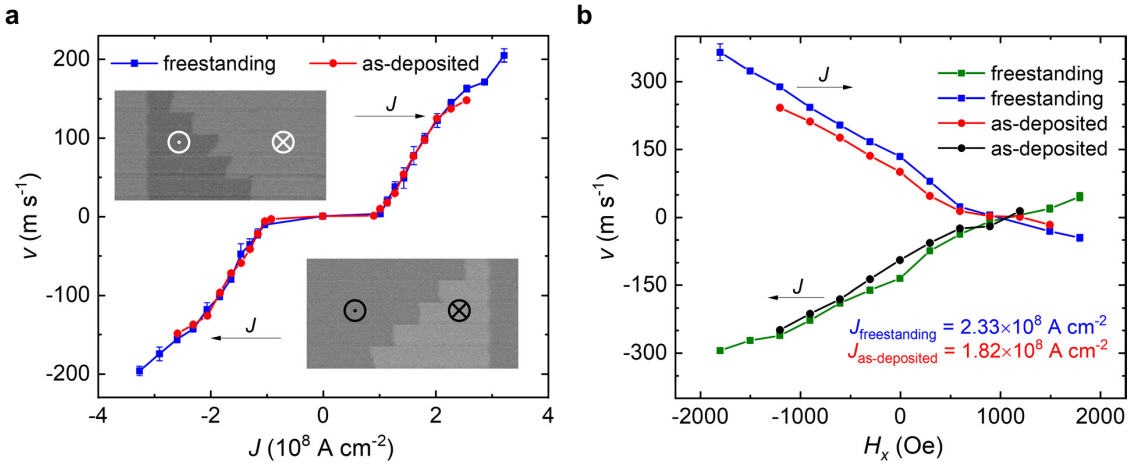

Figure 5.12: CIDWM in freestanding HM/FM heterostructures (Co/Ni/Co). **a,b,** Current-induced DW velocity in freestanding HM/FM heterostructures transferred onto a sapphire substrate (blue and olive; square) and as-deposited samples (red and black; circle) without (**a**) and with (**b**) a magnetic field applied along the x-axis. To investigate the longitudinal-field dependence of the CIDWM, a fixed current density of $J = 2.33 \times 10^8\,\mathrm{A\,cm^{-2}}$ for the freestanding racetrack and $J = 1.82 \times 10^8\,\mathrm{A\,cm^{-2}}$ for the as-deposited sample was used. The insets in **a** show typical Kerr images of DW motion in response to a series of injected 10-ns-long current pulses ($J = 2 \times 10^8\,\mathrm{A\,cm^{-2}}$) composed of three pulses in freestanding multilayers transferred onto a sapphire substrate. The bright and dark regions correspond to down ($\otimes$ or $\downarrow$) and up ($\odot$ or $\uparrow$) domains, respectively. The error bars in **a** and **b** represent the standard deviation.

5.5 Summary

In this chapter, we have demonstrated a successful transfer of large-size freestanding complex HM/FM heterostructures with MgO buffers. This is the first time that the freestanding PMA multilayer consisting of ultrathin metal thin films has been obtained. We have also fabricated Hall-bar and 2D RTM devices from the freestanding sheets transferred onto sapphire substrates and demonstrated that they exhibit comparable performance to the as-deposited films. Thus, the freestanding HM/FM heterostructures have the potential to realize functionalities that are not possible in as-deposited samples.

Chapter 6

Three-dimensional racetracks formed from freestanding heterostructures

As we discussed in Sections 3.2 and 3.3, RTM has demonstrated its ability to go beyond MRAM in the evolution from Racetrack Memory 1.0 to Racetrack Memory 4.0, and the pursuit of 3D devices would make it even more attractive due to the much higher data density. However, conventional methods used for depositing the required thin-film heterostructures, such as sputtering, hardly form homogeneous thin films on a pre-formed 3D structure [179]. In addition, the 3D structures that are made of polymer are sometimes unstable under the extreme growth conditions. On the other hand, exfoliation of 2D magnetic materials, which can also be applied in RTM, and dry transfer onto 3D structures are difficult to implement [180]. Even if the transfer is successful, the 2D materials cannot follow the underlying 3D structures very well [181]. In addition, the Curie temperatures of typical exfoliable 2D ferromagnets are far below room temperature, e.g. Fe_3GeTe_2 (205 K) [182] and $Cr_2Ge_2Te_6$ (< 61 K) [27], which impedes their application in RTM devices. Although ALD or 3D nanowires can be used to fabricate 3D devices, there are still a number of difficulties that need to be overcome before they can be used in practice (Section 3.3).

Having shown in the previous chapter that the performance of both RTM and Hall-bar devices shows no obvious degradation between the as-deposited multilayers and freestanding samples, in this chapter we will demonstrate the realization of the first 3D RTM device formed from freestanding HM/FM heterostructures. We will introduce an interesting functionality of this type of 3D RTM devices, called a '3D DW diode'. Moreover, we have fabricated 3D RTM devices formed from SAF structures, as they may have superior performance compared to 3D HM/FM RTM devices. We will also discuss the results of freestanding SAF racetracks.

It should be noted that the figures used in this chapter are reprinted from our paper [176], for which I am the first and corresponding author.

6.1 Fabrication of 3D racetracks from freestanding HM/FM heterostructures

In Chapter 5, we have demonstrated that large-size HM/FM heterostructures can be transferred onto sapphire substrates with their magnetic properties largely intact, and that the freestanding 2D racetracks formed from these transferred heterostructures exhibit almost identical performance to RTM devices fabricated from as-deposited multilayers. One of the key advantages of our water membrane based freestanding method is the versatility in the choice of transfer bases. Here, we transferred the magnetic heterostructures onto a pretreated sapphire substrate with 3D protrusions on it to form 3D RTM devices, as schematically illustrated in Fig. 6.1. The 3D protrusions are pre-etched plates with a width of approximately 3 μm, a height varying from 20 nm to 900 nm, and a length of 50 μm. These 3D protrusions were created from the sapphire substrates by photolithography and subsequent Ar-ion milling. An etching angle of 100° was used to avoid the formation of large sidewalls during milling. Since the etching rate for sapphire is around 1 μm per minute, a long-time etching is required. This involves a double layer of photoresist and a cooling process during etching. To completely remove any residual polymer resist, the sapphire substrates with arrays of 3D protrusions were then cleaned in acetone at 50 °C using ultrasonic cleaning for 1 h. It should be recognized that more sophisticated lithographic and etching methods, such as multi-photon lithography, are required to build more complex 3D structures. After the transfer process, the RTM devices were fabricated over the 3D protrusions in a similar way to the 2D case (photolithography followed by Ar-ion milling at an angle of 90°), except for a small defocus of ~ 0.6 μm during exposure in our Heidelberg MLA150 maskless optical lithography tool. The angles between the racetrack channels and the 3D protrusions were set at 45°, 90°, and 135°.

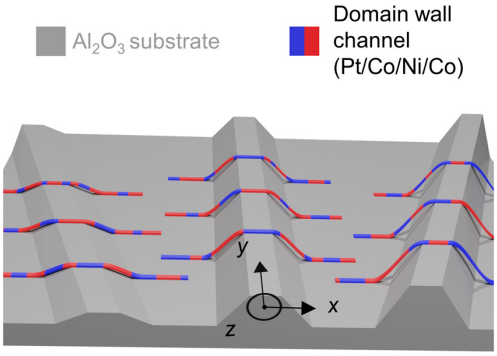

Figure 6.1: Schematic of 3D racetracks formed from freestanding HM/FM heterostructures. The 3D racetracks are formed by transferring the freestanding multilayer onto a sapphire substrate pre-patterned with protrusions. The 3D protrusions with different heights and different angles to the DW motion direction are patterned on the substrate by etching. The angle of a protrusion is defined as the angle between the protrusion and the x-axis. The blue and red parts of the racetrack correspond to down- and up-magnetized domains, respectively.

To evaluate the fabrication process, we then measured the surface morphology of samples with all different protrusion heights using AFM. The AFM images, together with an

optical image of a freestanding RTM device on a 900 nm 3D protrusion with an angle of 90°, taken by the camera inside the AFM, are summarized in Fig. 6.2. Despite the difference in height, the AFM images show a flat surface, indicating a successful lithography and etching process. The line scans in the racetrack region, marked by blue rectangles, and the bare protrusion region, marked by red rectangles, show that the RTM devices essentially follow the structures of the 3D protrusions, thus forming 3D RTM devices. For the 3D RTM devices formed on higher protrusions (700 nm and 900 nm), a slight deviation of the freestanding heterostructures from the 3D protrusion is observed, which may be attributed to the edge roughness of the protrusions and the transfer process. It should be noted that the force from an AFM tip is quite small, so the AFM characterization itself cannot affect the local geometry (Section 4.3.2).

We then carried out cross-sectional TEM on the RTM devices formed on the 700-nm-high protrusions to further determine the structure of the 3D RTM devices (Fig. 6.3). The freestanding film is found to closely follow the underlying 3D protrusion, which is in good agreement with the AFM line scans. In addition, the high-resolution TEM image shows the distinct interfaces between the different layers, and the freestanding thin film is found to adhere very well to the substrate with no obvious defects or breakages, again demonstrating successful deposition and transfer. As shown in the high-resolution TEM image, the thickness of the different layers can also be determined, indicating well-controlled growth. Moreover, we compared the cross-sectional SEM and TEM images with the line scans obtained from the AFM images, as shown in Fig. 6.4. The cross-sectional images agree well with the AFM line scans, regardless of the height of the protrusion, here 120 nm and 700 nm. It is worth noting that the difference between the line scan and the TEM image in the x-direction is caused by the AFM tip. This is particularly evident when the tip passes the high 3D protrusions. In short, all the AFM, SEM and TEM results confirm that the 3D racetracks follow the local geometry well, which has never been realized before.

6.2 CIDWM in 3D HM/FM racetracks

Following the characterizations of the 3D structures in the previous section, the effects of the 3D protrusion on the CIDWM were further investigated. It should be noted that the DW velocity can vary along the 3D racetrack due to the presence of protrusions, therefore the DW velocity in the 3D RTM devices is defined as the total length of the channel divided by the total pulse time used to drive the DW from one end of the racetrack across the protrusion to the other. In addition, the DW velocity is defined as zero if the DW is stuck in the protrusion area and therefore cannot reach the other end of the racetrack. Here, if the DW cannot pass one side of the 3D protrusion after applying a sequence of 60 10-ns-long current pulses, the DW is defined as being stuck by a 3D protrusion. For instance, the DW shown in Fig. 6.5 inset needed more than 20 but less than 30 10-ns-long current pulses to pass the right side of the protrusion, so the motion efficiency

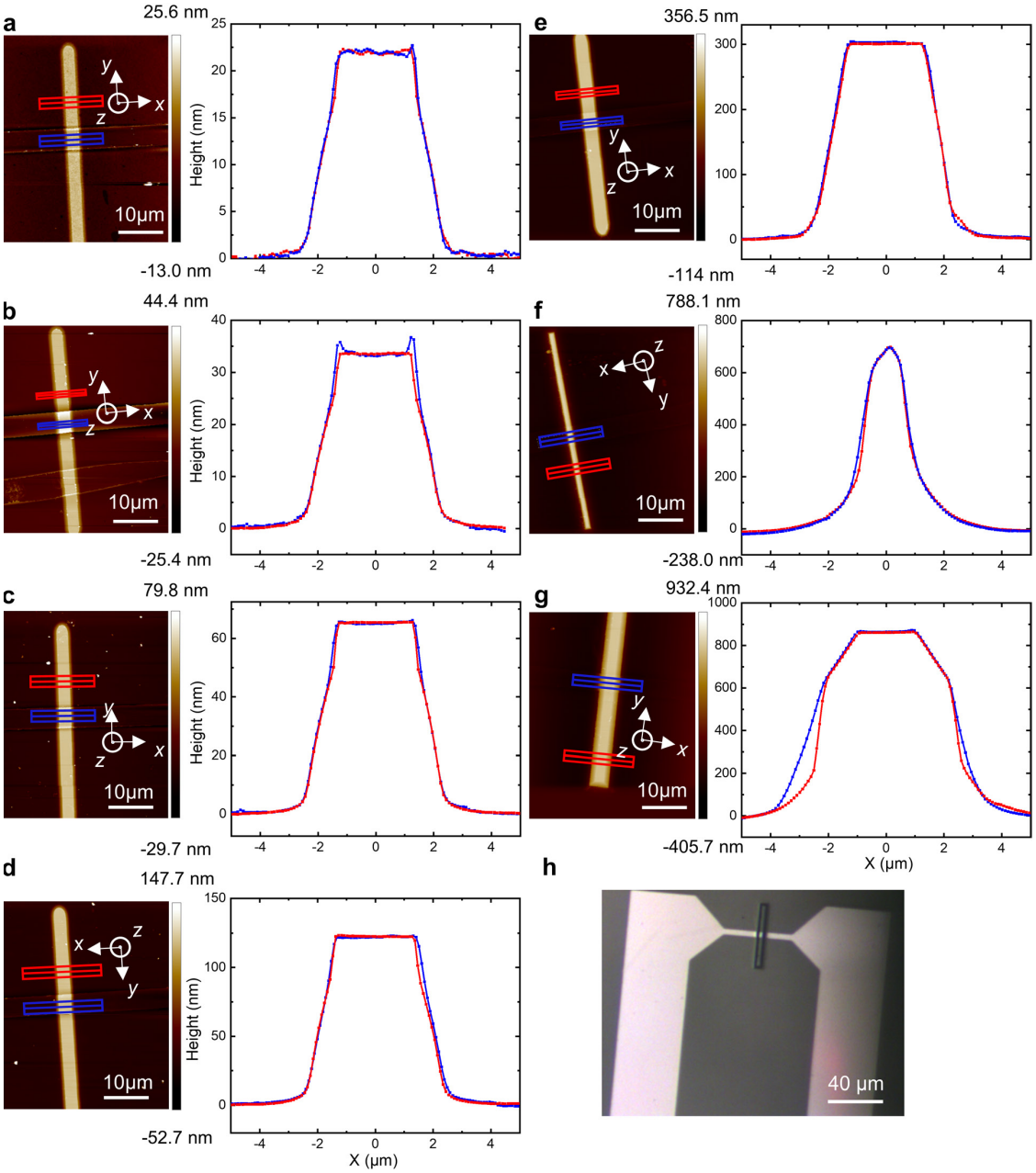

Figure 6.2: AFM images of 3D RTM devices and corresponding line scans of rectangularly marked regions. **a**-**g**, Left: AFM images of 3D protrusions with heights of 20 nm (**a**), 30 nm (**b**), 60 nm (**c**), 120 nm (**d**), 300 nm (**e**), 700 nm (**f**), 900 nm (**g**); Right: Corresponding line scans of rectangularly marked regions (red: 3D protrusions, blue: 3D racetrack). The origin is set at the center of the rectangle and the *x*-axis is perpendicular to the 3D protrusion. **h,** Optical image of a freestanding racetrack on a 3D protrusion with a height of 900 nm, width of 3 μm and angle of 90°.

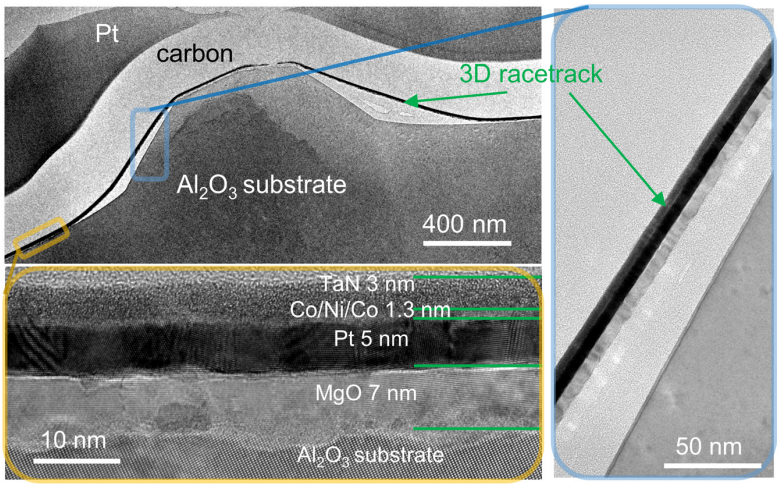

Figure 6.3: Cross-sectional TEM images of a 3D HM/FM racetrack. The freestanding HM/FM racetrack is formed on a 3D protrusion with a height of 700 nm and width of 3 µm (top left). Magnified high-resolution TEM images show individual layers in the 3D racetrack of the two regions highlighted in the top-left image as orange rectangle (bottom left) and blue rectangle (right). The horizontal green lines in the bottom-left panel indicate the interfaces between the individual layers.

decreased, but the DW was not stuck there. As shown in Fig. 6.5, the efficiency of CIDWM is lower in 3D racetracks than in 2D freestanding racetracks. It is worth noting that this degradation is almost independent of the height of the protrusion, as CIDWM shows similar behavior in racetracks with 20 nm and 900 nm protrusions. From this point of view, this degradation may result from the fabrication process of RTM devices and 3D protrusions.

Next, we focused on the threshold current density $J_{\text{threshold}}$ required to drive a DW across the 3D protrusion, which is critical for the realization of 3D RTM devices. In addition, $J_{\text{threshold}}$ for driving a DW in a device with no protrusion (defined as 0 nm high protrusion) was measured on the same wafer used for 3D racetracks, but in a different region. Again, the standard deviations are from multiple measurements, as five devices were measured to determine $J_{\text{threshold}}$ required to drive a DW across one type of 3D protrusion, i.e. a protrusion with a given angle and height. Surprisingly, $J_{\text{threshold}}$ increases as soon as the 3D protrusion is introduced, but remains almost constant as the protrusion height increases, varying from the nanometer to the micrometer range (Fig. 6.6 a). More specifically, when the 3D protrusion is perpendicular to the racetrack channel (90° protrusion), $J_{\text{threshold}}$ reaches a maximum value that is identical for up-down and down-up DWs in positive and negative current directions. On the other hand, if an oblique angle is formed between the racetrack channel and the protrusion, a different scenario occurs: $J_{\text{threshold}}$ is different for different DW types and injected current directions. In short, $J_{\text{threshold}}$ is strongly dependent on the angle between the racetrack channel and the 3D protrusion.

To illustrate this difference clearly, we selected the data measured in the 20 nm high protrusion devices and replotted the protrusion angle dependence of the threshold current density in Fig. 6.6 b. When the angle is 45°, $J_{\text{threshold}}$ is distinctly smaller for an up-

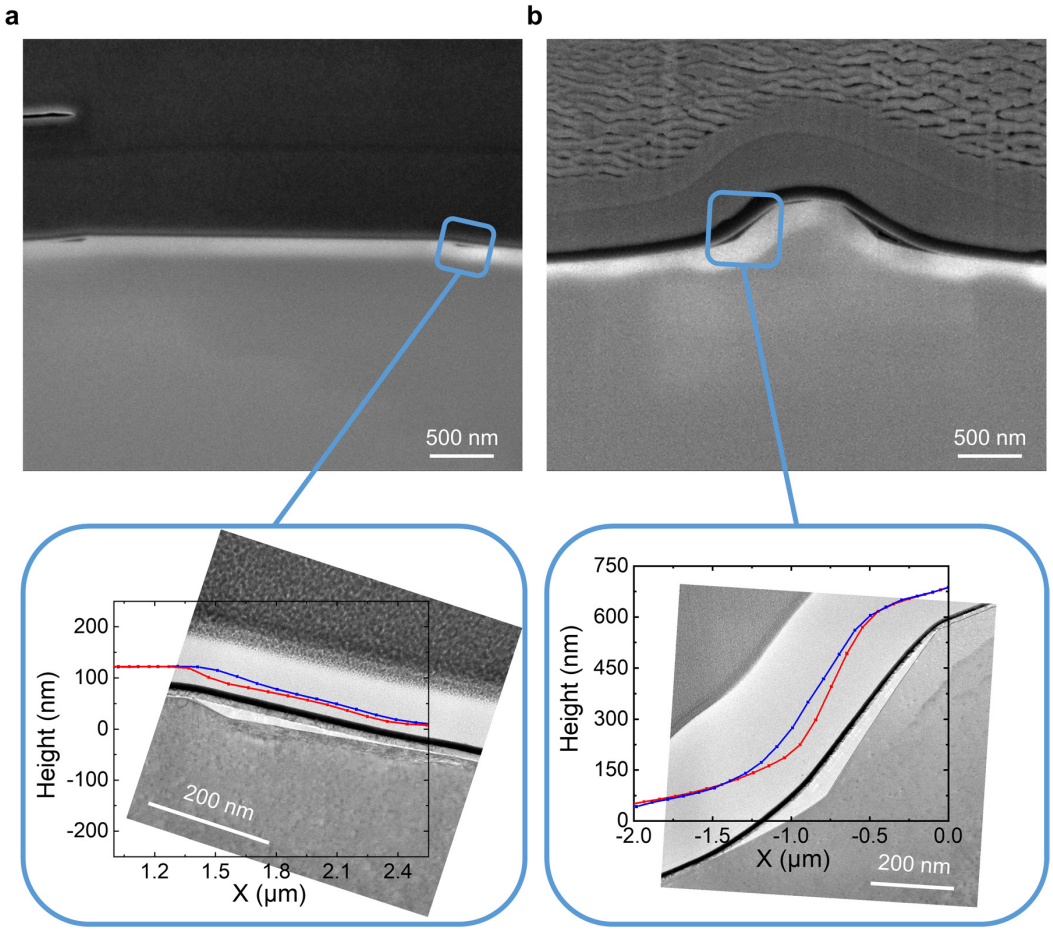

Figure 6.4: Cross-sectional SEM and TEM images of 3D racetracks formed from freestanding HM/FM heterostructures. Upper panel: cross-sectional SEM images of the 3D racetrack devices with protrusion heights of 120 nm (**a**) and 700 nm (**b**); Lower panel: magnified TEM image of the side region and corresponding line scans from the AFM images. Note that the difference between the line scan and the TEM image in the x-direction is caused by the AFM tip. This is especially evident when the tip passes over high 3D protrusions.

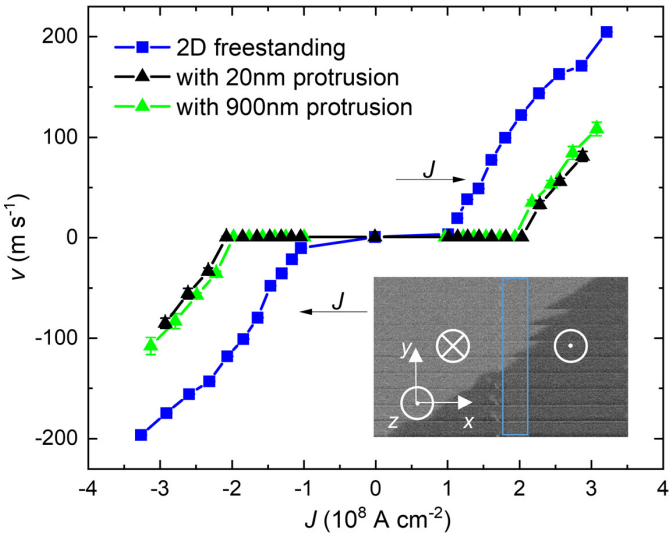

Figure 6.5: CIDWM in 3D racetracks formed from freestanding HM/FM heterostructures. DW velocity versus current density curves measured in racetracks formed from the freestanding multilayers without protrusions (blue square) and with protrusions perpendicular to the racetrack channel with heights of 20 nm (black triangle) and 900 nm (green triangle). The inset shows the typical Kerr images of the DW motion in response to a series of injected 10-ns-long current pulses ($J = -2.30 \times 10^8\,\mathrm{A\,cm^{-2}}$) composed of ten pulses in the 3D RTM device formed on a protrusion with a height of 20 nm and an angle of 90°. The bright and dark regions correspond to the down ($\otimes$ or $\downarrow$) and up ($\odot$ or $\uparrow$) domains, respectively. The tall blue box indicates the position of the protrusion.

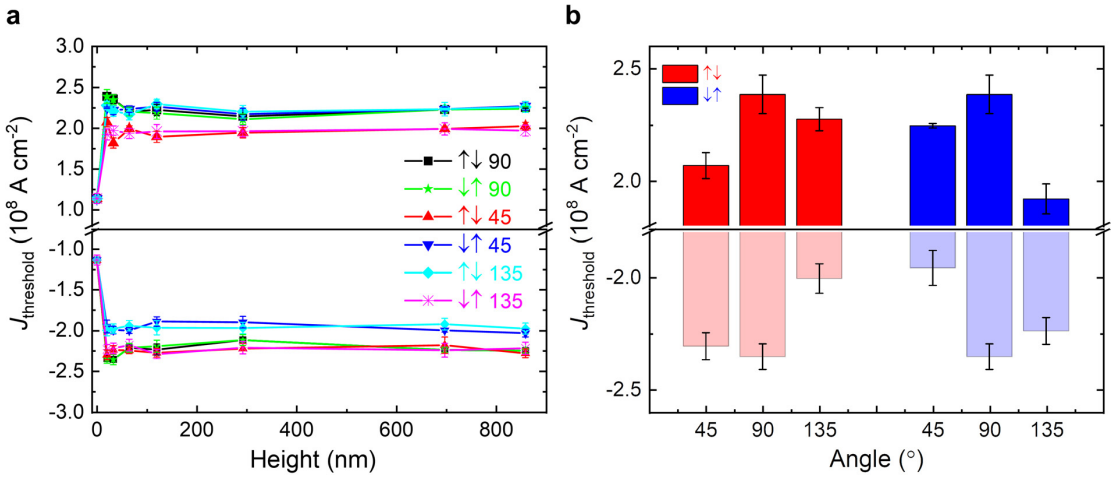

Figure 6.6: CIDWM in 3D HM/FM racetracks formed on different types of protrusions. Threshold current density $J_{\mathrm{threshold}}$ required to drive a DW across 3D protrusions with different heights (0, 20, 30, 60, 120, 300, 700 and 900 nm) (**a**) and a height of 20 nm (**b**). Two types of DW (↑↓ or up–down and ↓↑ or down–up) cross the 3D protrusions at three different angles (45°, 90° and 135°) in **a**: ↑↓ DWs cross the protrusions at an angle of 90° (black square), 45° (red triangle) and 135° (cyan diamond); ↓↑ DWs cross the protrusions at an angle of 90° (green five-pointed star), 45° (blue inverted triangle) and 135° (magenta asterisk). The red and blue bars in **b** correspond to up–down (↑↓) and down–up (↓↑) DWs, respectively. The positive and negative values are defined with respect to the $+x$ and $-x$ direction, respectively. The error bars in **a** and **b** represent the standard deviation.

down DW compared to a down-up DW for positive currents and vice versa for negative currents; on the other hand, when the angle is 135°, $J_{\text{threshold}}$ is larger for an up-down DW compared to a down-up DW for positive currents and vice versa for negative currents. And for one type of DW, $J_{\text{threshold}}$ required to drive the DW across the 45°/135° 3D protrusion differs in the directions. This non-reciprocal behavior in CIDWM can be attributed to the chirality of the Néel type DW (Section 3.2.2), as the DMI effective field is influenced by the local geometry of the protrusions [164,183,184]. Thus, for a particular combination of DW type (up-down or down-up) and protrusion angle, a lower energy barrier is realized compared to other combinations. In other words, the selective passing of DWs can be realized from the difference in $J_{\text{threshold}}$. For example, in an RTM device formed on the 45° protrusion, only the down-up DW can be moved across the protrusion at a current density of $J = -2 \times 10^8\,\text{A}\,\text{cm}^{-2}$, while the up-down DW cannot (Fig. 6.7 a and b). Fig. 6.7 summarizes the typical Kerr images of the current- and field-driven DW motion across the 3D protrusions. A 3D DW 'diode' is thus realized on the basis of the DW type in combination with the DW motion direction.

Notably, a distinct tilting of the DWs is found in the CIDWM of the 3D RTM devices, independent of protrusion height and DW type, as shown in Fig. 6.7 a-l and Fig. 6.5 inset. However, no such tilting behavior can be observed in the field-driven case (Fig. 6.7 m,n). Generally, a DW prefers to keep perpendicular to the channel in order to minimize the total energy. However, due to its chiral nature derived from the DMI, a DW can start to tilt when the injected current is applied [184]. In the absence of pinning, the relaxation process would be very fast and the DW would quickly return to its shortest length perpendicular to the channel [185]. Therefore, we cannot observe its tilting (shown in Fig. 5.12 a inset). On the other hand, if the quasi-static pinning is relatively large, the tilting of the DW becomes more pronounced, as we observed in our experiments, which is also consistent with the lower CIDWM efficiency compared to 2D devices.

In short, a non-reciprocal behavior in CIDWM has been found in the 3D RTM devices formed from freestanding HM/FM heterostructures, showing the potential to be used in next-generation DW logic devices [35].

6.3 CIDWM in 3D SAF racetracks

As we discussed in Section 3.2.2, Racetrack Memory 4.0 using SAFs is highly efficient and robust to external perturbations. Therefore, it is promising to use this type of heterostructures in 3D RTM devices. In this section, we will extend the aforementioned freestanding technique to both 2D and 3D RTM devices formed from SAFs.

6.3.1 CIDWM in freestanding SAF heterostructures

Similar to the HM/FM case, the SAF heterostructures that are composed of sputtered TaN(20.0)/Pt(30.0)/Co(3.0)/Ni(7.0)/Co(1.5)/Ru(9.5)/Co(3.0)/Ni(7.0)/Co(3.0)/TaN(30.0) were deposited on an SAO(200.0)/MgO(100.0) bilayer prepared in PLD (all units in Å).

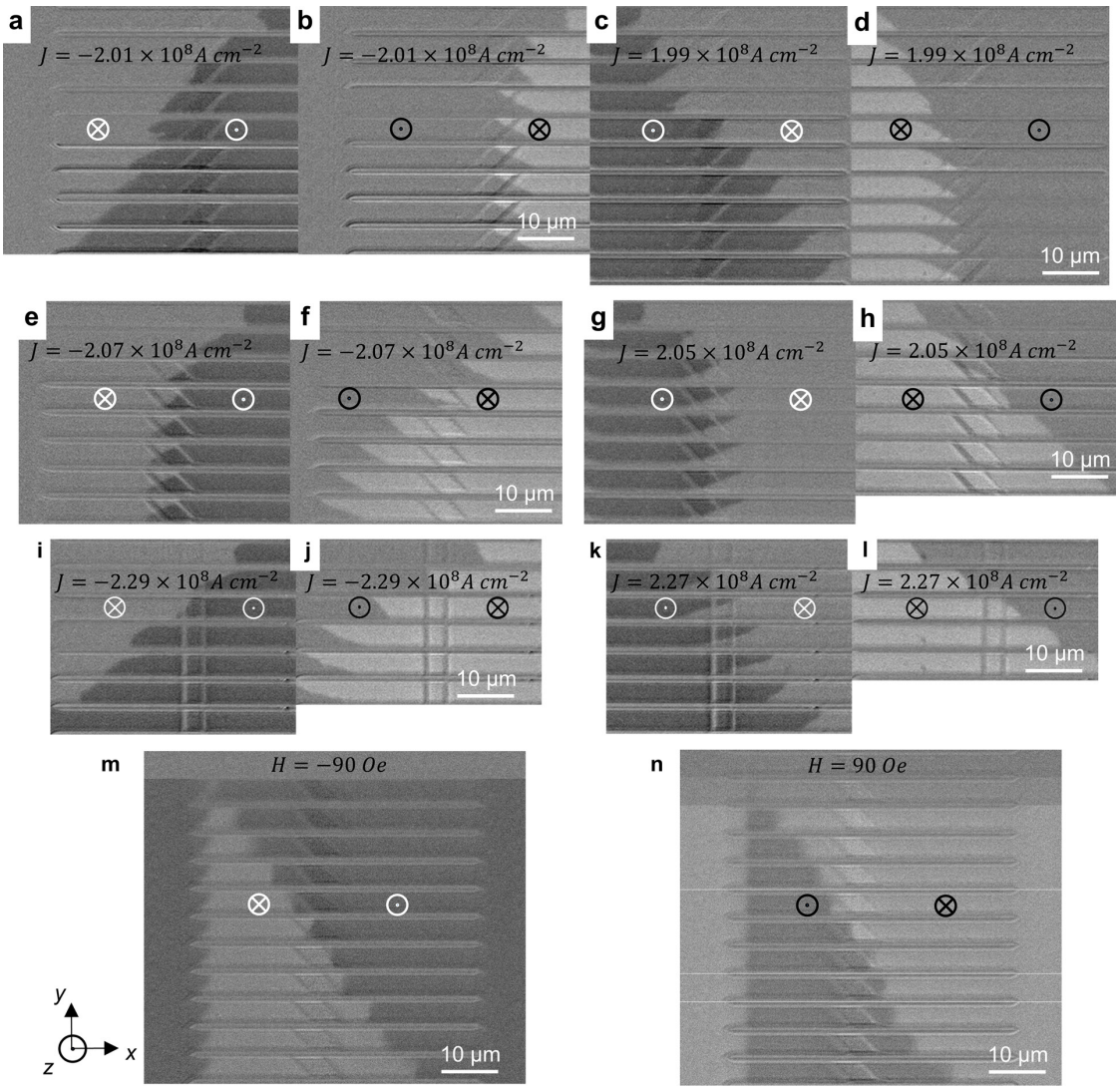

Figure 6.7: Typical Kerr images of current and field induced DW motion across 3D protrusions in HM/FM racetracks. **a**-**l**, DW motion in response to a series of injected current pulses ($J \approx 2 \times 10^8\,\mathrm{A\,cm^{-2}}$) consisting of ten × 10 ns long pulses in freestanding HM/FM racetracks across 3D protrusions at an angle of 45° (**a**-**d**), 135° (**e**-**h**) and 90° (**i**-**l**) with respect to the x-axis. **m,n,** DW motion across HM/FM 3D protrusions at an angle of 135° with respect to the x-axis in response to an out-of-plane magnetic field $H = -90$ Oe (**m**) and $H = 90$ Oe (**n**). Each photo is taken at one-second intervals. The motion of two different types of DWs (down-up or ⊗-⊙ or ↓↑ and up-down or ⊙-⊗ or ↑↓) driven by the same current density (same direction) and the same magnetic field intensity (opposite directions) are compared. The bright and dark regions correspond to down (⊗ or ↓) and up (⊙ or ↑) domains. Positive and negative values are defined with respect to $+x/+z$ and $-x/-z$ directions, respectively.

And the transfer from the PLD chamber to the sputtering chamber was carried out in air without any additional protection. For control experiments, the same SAF stacks were also deposited on MgO substrates, hereafter named as as-deposited samples. As shown in Fig. 6.8 a, the XRD patterns of the samples deposited on both MgO and an SAO/MgO bilayer clearly show the broad peak from the multilayer structure, again demonstrating successful growth. In addition, the AFM images of both samples show a flat surface (Fig. 6.8 b and c), indicating a high quality and well controlled deposition.

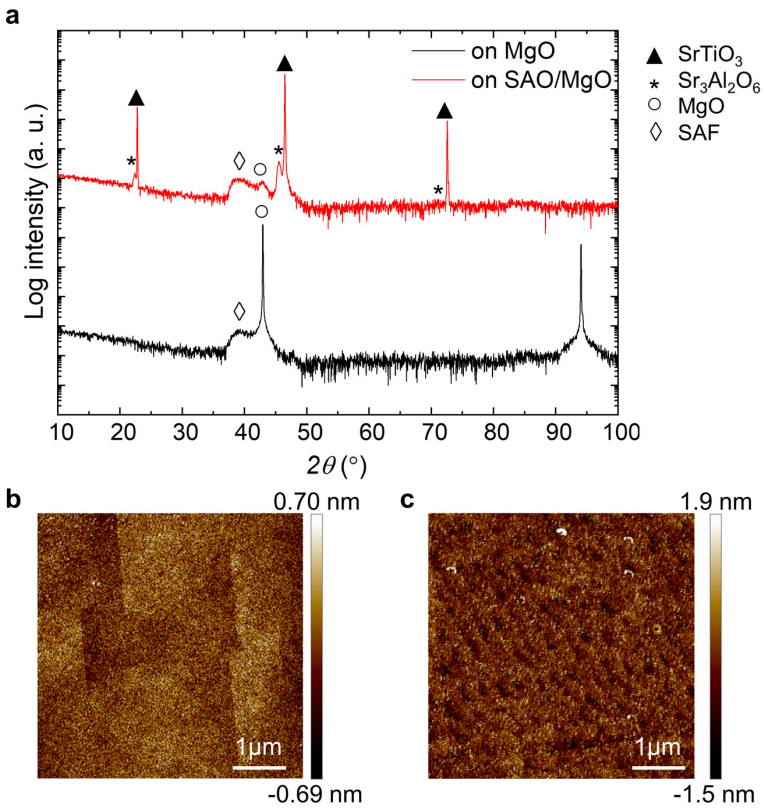

Figure 6.8: Deposition of SAF heterostructures. **a,** Out-of-plane θ–2θ XRD pattern of TaN/Pt/Co/Ni/Co/Ru/Co/Ni/Co/TaN SAF multilayers deposited on MgO and SAO/MgO. **b,c,** AFM images of the as-deposited SAF heterostructures on MgO (**b**) and SAO/MgO (**c**). The root mean square roughness values in **b** and **c** are 0.202 nm and 0.454 nm, respectively.

The water membrane based lift-off and transfer method discussed in previous chapters was also used to obtain freestanding SAF heterostructures. To evaluate the transfer process, we focused on the magnetic properties. The *M*-*H* curves of the samples before and after transfer were measured by Kerr microscopy at room temperature. After the transfer process, the freestanding SAF heterostructures show almost identical behavior to the samples before lift-off and transfer, with the upper and lower PMA layers nearly compensating for each other (Fig. 6.9). This results in a similar CIDWM behavior in both samples.

We used the same design as the RTM devices characterized in Chapter 5 and followed procedures similar to the fabrication of 2D HM/FM racetracks to fabricate 2D SAF racetracks. The CIDWM behavior was then measured in our Kerr microscope. As shown in Fig. 6.10 a, fast CIDWM of a velocity up to 600 m s^{-1} is achieved in the freestanding

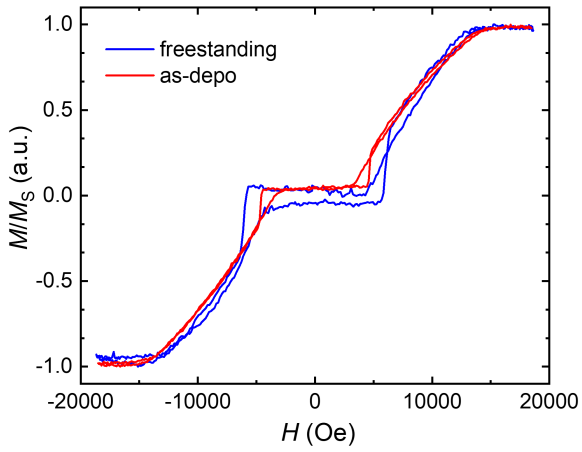

Figure 6.9: Magnetic properties of SAF heterostructures. Out-of-plane normalized magnetization (M/M_s) versus field (H) curves of the as-deposited SAF sample (red) and the freestanding SAF sample (blue) measured by MOKE at room temperature.

SAF heterostructures, which is quite close to the performance of the as-deposited sample. Furthermore, we characterized the longitudinal field dependence of the CIDWM in the as-deposited and freestanding samples at a fixed current (Fig. 6.10 b). Here, the current density is equal to $J = 1.85 \times 10^8\,\mathrm{A\,cm^{-2}}$ and $J = 1.75 \times 10^8\,\mathrm{A\,cm^{-2}}$ for the freestanding and as-deposited racetracks, respectively. Indeed, the freestanding racetrack shows similar CIDWM behavior to the as-deposited one. Considering that the longitudinal field dependence of the CIDWM for the SAF structures is extremely sensitive to variations in the magnetic properties [163, 178], our results, especially the similar response of the CIDWM to the external longitudinal field before and after transfer, provide strong evidence for the success of our approach. This provides a solid foundation for subsequent experiments, namely the fabrication of SAF-based 3D racetracks.

6.3.2 CIDWM in 3D racetracks formed from freestanding SAF heterostructures

Using the similar methods to those described in Section 6.1, 3D RTM devices formed from freestanding SAF heterostructures were also fabricated (Fig. 6.11 a). Surprisingly, unlike the 3D RTM devices based on HM/FM heterostructures, where the motion efficiency significantly degrades with a much lower DW velocity and a two times higher $J_{\mathrm{threshold}}$ as compared to the 2D case, the 3D racetracks based on SAF heterostructures show almost unchanged performance. As shown in Fig. 6.11 b, almost identical DW velocity versus current density curves are observed in the SAF-based RTM devices, with or without 3D protrusions, regardless of the protrusion height. Moreover, the DW can freely move across the 3D protrusions even at ultralow DW velocities, i.e., near the threshold current density. We further varied the angle between the racetrack channel and the 3D protrusion and found no obvious degradation in CIDWM efficiency. Fig. 6.12 shows the typical Kerr images, snipped from continuously recorded videos, of DW driven by a near-threshold-current-density current smoothly across the different types of 3D protrusions. In short, the highly efficient CIDWM in the SAF structure is very well maintained in the

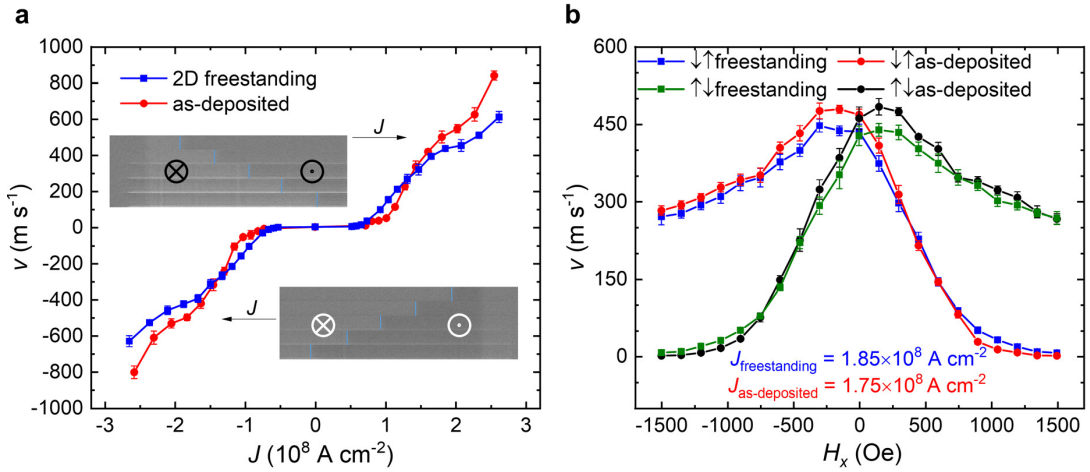

Figure 6.10: CIDWM in freestanding SAF heterostructures. **a,b,** Current-induced DW velocity in freestanding SAF heterostructures transferred onto a sapphire substrate (blue and olive; square) and as-deposited samples (red and black; circle) without (**a**) and with (**b**) a magnetic field applied along the x-axis. To investigate the longitudinal-field dependence of the CIDWM, a fixed current density of $1.85 \times 10^8\,\mathrm{A\,cm^{-2}}$ for the freestanding racetrack and $1.75 \times 10^8\,\mathrm{A\,cm^{-2}}$ for the as-deposited sample was used. The insets in **a** show typical Kerr images of DW motion in response to a series of injected 10-ns-long current pulses ($J = 2.28 \times 10^8\,\mathrm{A\,cm^{-2}}$) composed of one pulse in the as-deposited multilayers. The blue lines highlight the DW position. The bright and dark regions correspond to down ($\otimes$ or $\downarrow$) and up ($\odot$ or $\uparrow$) domains, respectively. The error bars in **a** and **b** represent the standard deviation.

3D case. As we discussed in Section 3.2.2, previous studies by our group have shown that the DW in SAFs is robust to the changes in local geometry due to the large ECT and symmetric structure of SAFs. Here, our results in 3D SAF racetracks show that this is still true in 3D geometries, which means that the SAF structure is ideal for application in next-generation highly-efficient 3D RTM devices.

6.4 Summary

In this chapter, we have successfully fabricated 3D RTM devices consisting of HM/FM or SAF heterostructures by combining our water membrane based freestanding technique with conventional 2D device fabrication processes. When utilizing freestanding HM/FM heterostructures, a non-reciprocal behavior in CIDWM is realized, which can be useful for DW logics; while when using freestanding SAF heterostructures, we find that the 3D RTM devices formed from these heterostructures exhibit highly-efficient CIDWM similar to that in 2D devices, facilitating the fabrication of efficient RTM devices with high data density. The demonstration of racetracks in the third dimension is an important milestone in the development of RTM. In conclusion, our results open up a new route for the fabrication of racetracks, which can be applied to the construction of 3D structures as well as the fabrication of flexible devices. As for the future plan, the integration of novel writing/reading elements using the third dimension may be a possible direction.

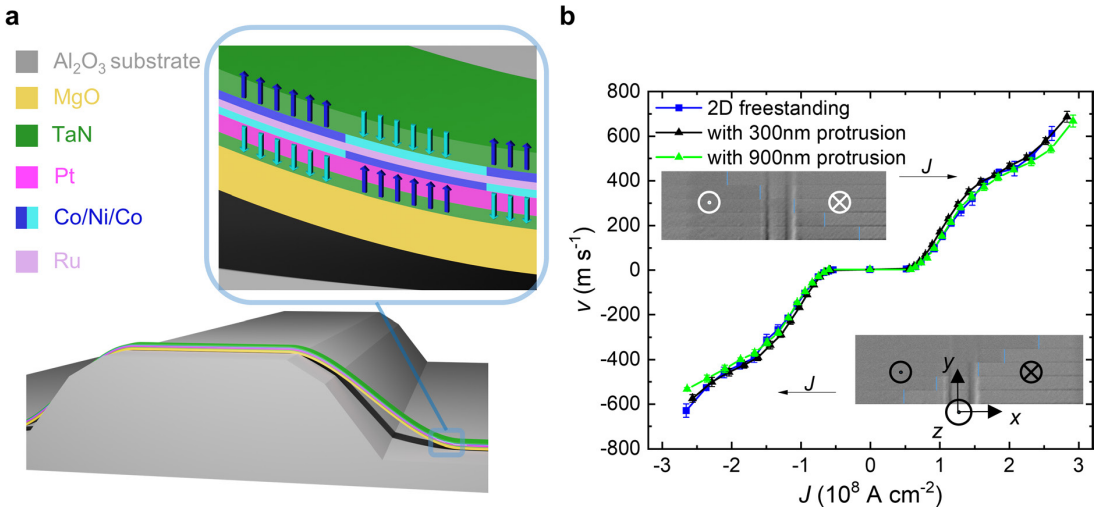

Figure 6.11: CIDWM in 3D racetracks formed from freestanding SAF heterostructures. **a,** Schematic of 3D racetracks formed from freestanding SAF heterostructures transferred onto a pre-patterned sapphire substrate. The light and dark blue arrows illustrate the magnetization in the two PMA layers, which are antiferromagnetically coupled via the Ru spacer. **b,** DW velocity versus current density in racetracks formed from the 2D freestanding SAF heterostructures without any protrusions (blue square) and with protrusions perpendicular to the racetrack channel with heights of 300 nm (black triangle) and 900 nm (green triangle). The insets in **b** show typical Kerr images of the DW motion in response to a series of injected 10-ns-long current pulses ($J = 1.42 \times 10^8\,\mathrm{A\,cm^{-2}}$) composed of two pulse in the freestanding SAF multilayers transferred onto a sapphire substrate with 300-nm-high protrusions and protrusion angle of 90°. The blue lines highlight the DW position. The bright and dark regions correspond to down ($\otimes$ or $\downarrow$) and up ($\odot$ or $\uparrow$) domains, respectively. The error bars represent the standard deviation.

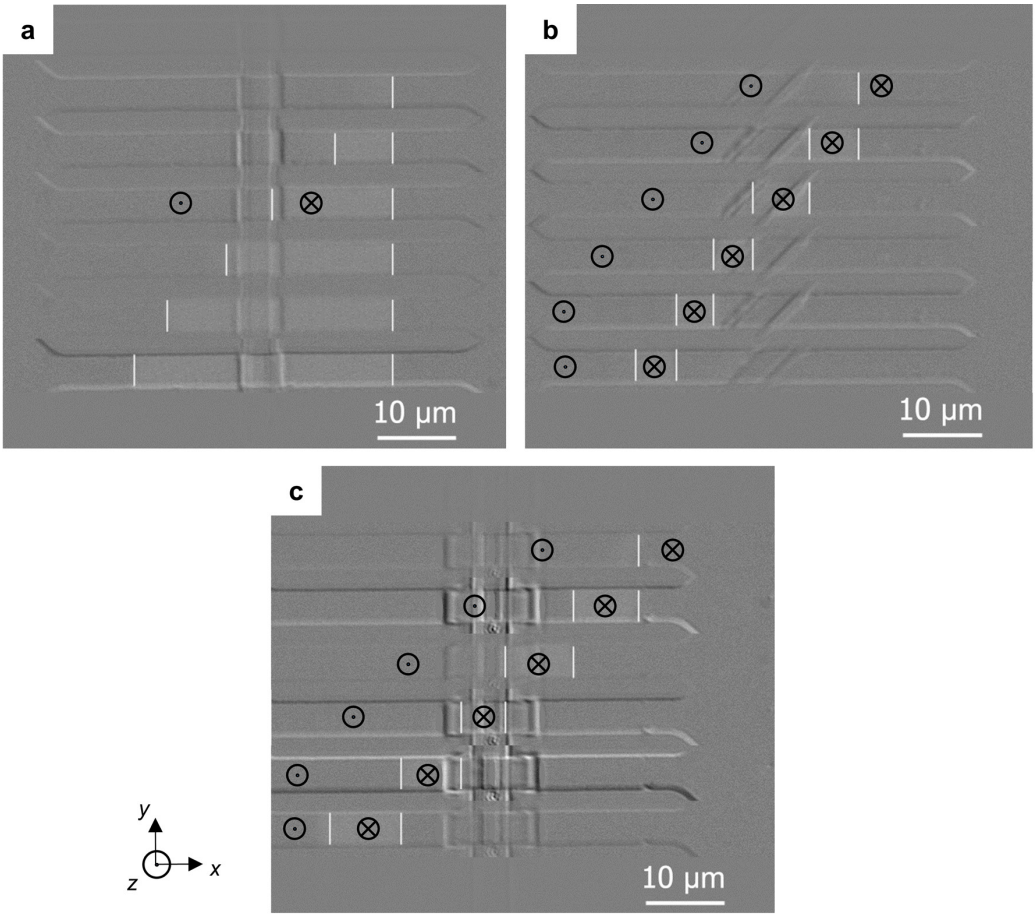

Figure 6.12: Typical Kerr images of CIDWM across 3D protrusions in SAF racetracks. **a,** DW motion in response to a series of injected current pulses ($J = 0.64 \times 10^8\,\mathrm{A\,cm^{-2}}$) consisting of 50 $\times$ 10 ns long pulses in freestanding SAF racetracks across 300-nm-high 3D protrusions at an angle of 90° with respect to the x-axis. **b,** DW motion in response to a series of injected current pulses ($J = 0.61 \times 10^8\,\mathrm{A\,cm^{-2}}$) consisting of 90 $\times$ 10 ns long pulses in freestanding SAF racetracks across 300-nm-high 3D protrusions at an angle of 45°. **c,** DW motion in response to a series of injected current pulses ($J = 0.66 \times 10^8\,\mathrm{A\,cm^{-2}}$) consisting of 60 $\times$ 10 ns long pulses in freestanding SAF racetracks across 900-nm-high 3D protrusions at an angle of 90°. Photos are taken from videos. The white lines mark the start and end position of the DWs. The bright and dark regions correspond to down ($\otimes$ or $\downarrow$) and up ($\odot$ or $\uparrow$) domains, respectively.

Chapter 7

Racetracks formed from freestanding HM/FM layers without buffer layers

In Chapter 5 and 6, the freestanding thin films transferred onto other bases always contain an MgO buffer layer. This buffer layer can not only ensure high quality growth of subsequent sputtered metal layers, but also protect the sacrificial layer SAO from moisture, thus facilitating the transfer from our PLD chamber to the sputtering chamber. Although it is possible to fabricate 3D RTM devices or flexible racetracks from the freestanding heterostructures with MgO buffer, the presence of this buffer layer prevents coupling between the PMA layer and other exotic materials, such as superconductors and ferromagnets with IP anisotropy. In this chapter, we will systematically investigate the influence of buffer layers on magnetic properties and CIDWM behavior, and demonstrate the possibility of eliminating the buffer layer in freestanding racetracks.

7.1 HM/FM heterostructures on different substrates

In general, Pt prefers to align along the (111) orientation on MgO substrates, facilitating good PMA of Co/Ni/Co deposited thereon. For this reason, we always use MgO or SAO/MgO as the substrates for deposition in the previous chapters. In addition, other buffer layers, such as TaN, can also be used to ensure the PMA of samples on other substrates, including Si wafers. To evaluate the possibility of eliminating buffers such as MgO and TaN while maintaining good PMA of as-deposited thin films, we selected four different substrates, including MgO substrate, Si wafer, STO/SAO/MgO (deposited buffer), and STO/SAO. In addition, we varied the thickness of the Pt layer to find out the minimum thickness of this layer that can stabilize the PMA of Co/Ni/Co, since through the proximity effect in HM [186, 187], the magnetic properties can be tunable. The samples were deposited by PLD and magnetron sputtering, following a process similar to that described in the previous chapters, with one difference: to reduce the possible damage from humidity, the SAO samples (without capping) were transferred into the sputtering chamber in desiccants within 1 minute.

We first examined the crystallinity and surface morphology of the as-deposited samples. As shown in Fig. 7.1 a-d, the peaks for (111) - oriented Pt can be used to determine the crystallinity of the samples, indicating that the samples deposited on MgO and SAO/MgO have the best crystallinity, while the samples deposited on Si have the worst. It can also be clearly seen that as the thickness of Pt decreases, the crystallinity also deteriorates. Only when the thickness of Pt reaches 40 Å, we can see a peak for Pt from the thin film deposited on Si. This is mainly due to increased discontinuities and defects in the thin films, which we will demonstrate in the next section. On the other hand, all the AFM images show that the surfaces of the samples are very flat (Fig. 7.2 a-d). We can see some high points in the thin films deposited on MgO and SAO/MgO, while these high points can hardly affect the CIDWM behavior and the magnetic properties of the sample. Thin films deposited on Si wafers show the best surface quality, but the crystallinity of these samples is not good.

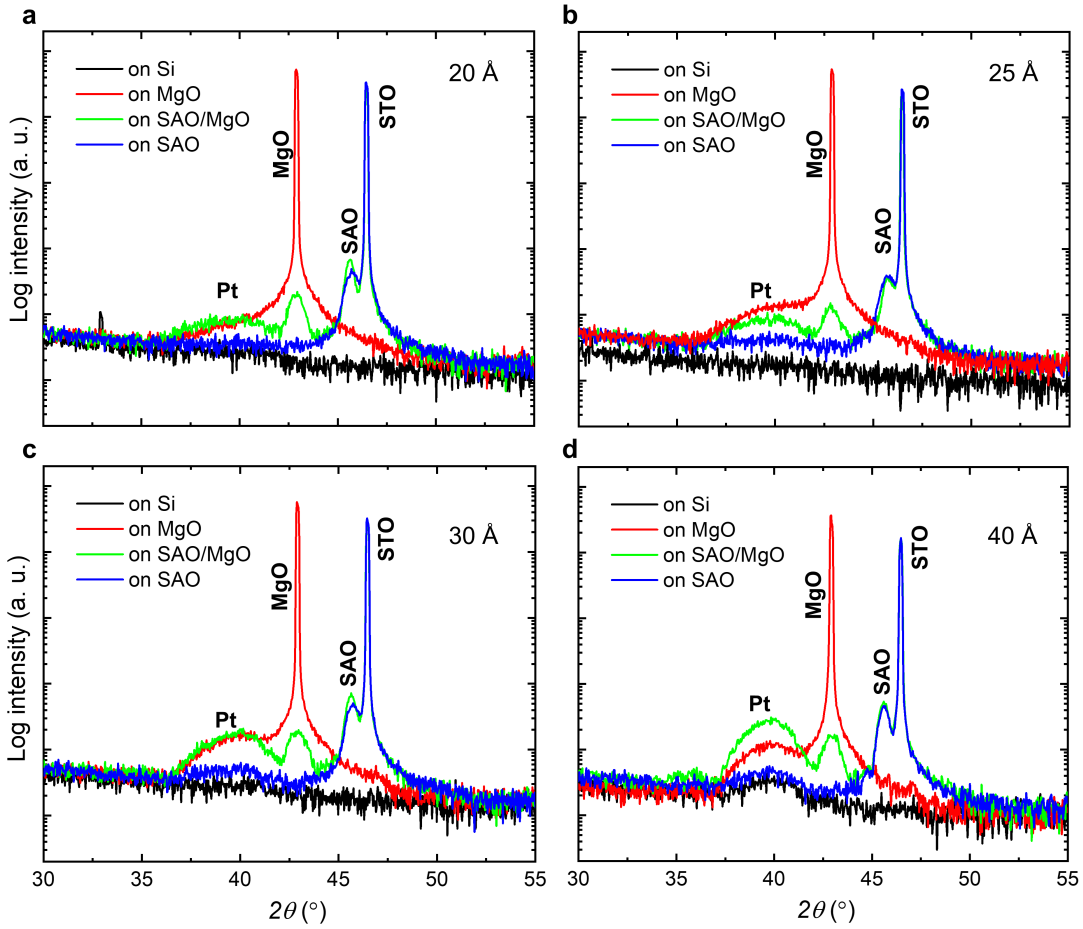

Figure 7.1: Limited range out-of-plane θ–2θ XRD pattern of HM/FM heterostructures deposited on different substrates. The thickness of the Pt layers is set to be 20 Å (**a**), 25 Å (**b**), 30 Å (**c**) and 40 Å (**d**). Different colors represent different substrates: black for Si wafer, red for MgO substrate, green for SAO/MgO bilayer, and blue for SAO thin film.

We then characterized the as-deposited samples at room temperature using our vibrating-sample magnetometer (VSM) to assess their magnetic anisotropy. Fig. 7.3 a-d summarize the OOP VSM results, which indicate a strong dependence of PMA on the

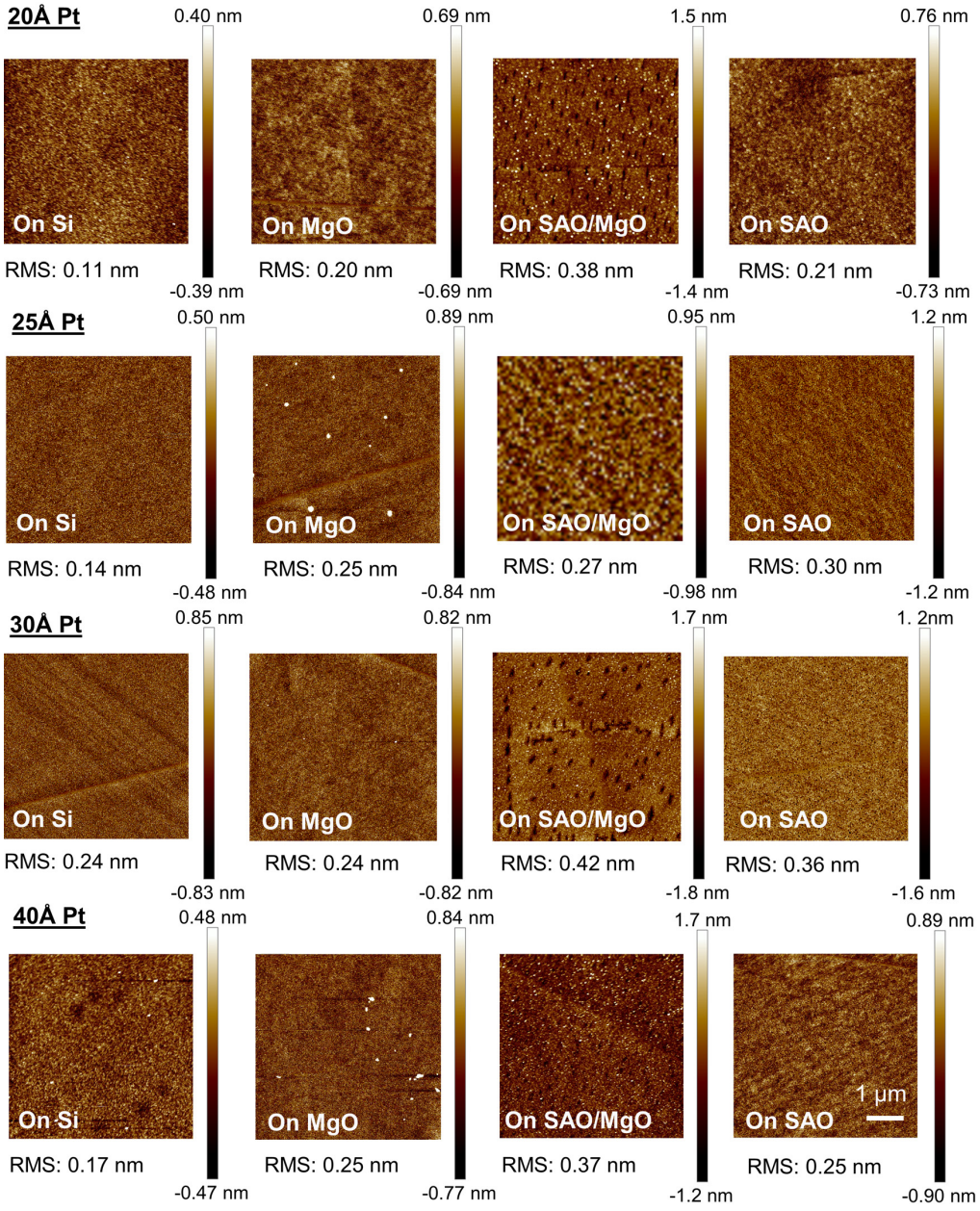

Figure 7.2: AFM images of HM/FM heterostructures deposited on different substrates. The root mean square roughness value of different samples is shown below each figure.

substrate and the thickness of Pt. As shown in Fig. 7.3 a-c and highlighted in Fig. 7.3 d, the PMA becomes stronger with increasing the thickness of Pt layer. The inset in Fig. 7.3 d shows a typical VSM IP measurement of our samples, again showing the PMA of our sample (deposited on MgO with 30 Å Pt), i.e. no IP magnetic easy-axis. According to the substrates, samples deposited on SAO show the strongest PMA, while all the samples deposited on Si show almost no PMA (the sample with 30 Å Pt exhibits very weak PMA) (Fig. 7.3 a-c). Samples deposited on MgO and SAO/MgO show similar behavior: when the Pt layer is less than 30 Å, the samples show weak or no PMA; on the other hand, when the thickness of the Pt layer reaches 30 Å, the samples show a good PMA and the coercive field of them is comparable to that of the samples deposited directly on SAO. Although the samples deposited on SAO show the PMA even with very thin Pt down to 20 Å, the coercive field of the sample becomes larger (from $\sim$ 45 Oe to $\sim$ 70 Oe) and the rectangularity of the hystreresis becomes better with increasing Pt thickness, indicating that the PMA can be improved with thicker Pt layer. In short, 30 Å Pt is sufficient to obtain a good PMA in most cases except direct deposition on Si wafers, and SAO can act as a good buffer for the deposition of Co/Ni/Co with a strong PMA.

In addition, the crystallinity and surface morphology do not appear to have a strong relationship with the PMA of the samples. Kerr microscopy is required to further confirm that we can eliminate buffer layers and still maintain the PMA and therefore the CIDWM performance of the samples.

7.2 CIDWM in freestanding HM/FM heterostructures without buffer layers

The HM/FM multilayers deposited on STO/SAO and STO/SAO/MgO with different Pt thicknesses were then transferred onto sapphire substrates using the water membrane based freestanding technique, as schematically illustrated in Fig. 7.4 a. Following a similar process of photolithography and ion milling as described in the previous chapters, the racetrack devices were fabricated. To evaluate the transfer process, we performed cross-sectional TEM measurements on a device fabricated from the sample deposited directly on SAO with 30 Å Pt. As shown in Fig. 7.4 b, different layers with sharp interfaces and clear lattice stripes are clearly visible, indicating a successful transfer process and good quality of the freestanding HM/FM heterostructures even without any buffer layer. This again demonstrates the robustness of our method.

We then measured the current density dependence of the DW velocity in the freestanding racetracks and compared it with devices fabricated from thin films deposited on other substrates. As shown in Fig. 7.5 a, some samples, including the 20 Å Pt freestanding thin films without buffer and the 25 Å Pt freestanding thin films with MgO buffer, show PMA but also contain many defects and multi-domains, indicating that the samples are not quite homogeneous, which is consistent with our XRD results. Due to the discontinuity, some multi-domains can be easily switched by small external magnetic fields (smaller

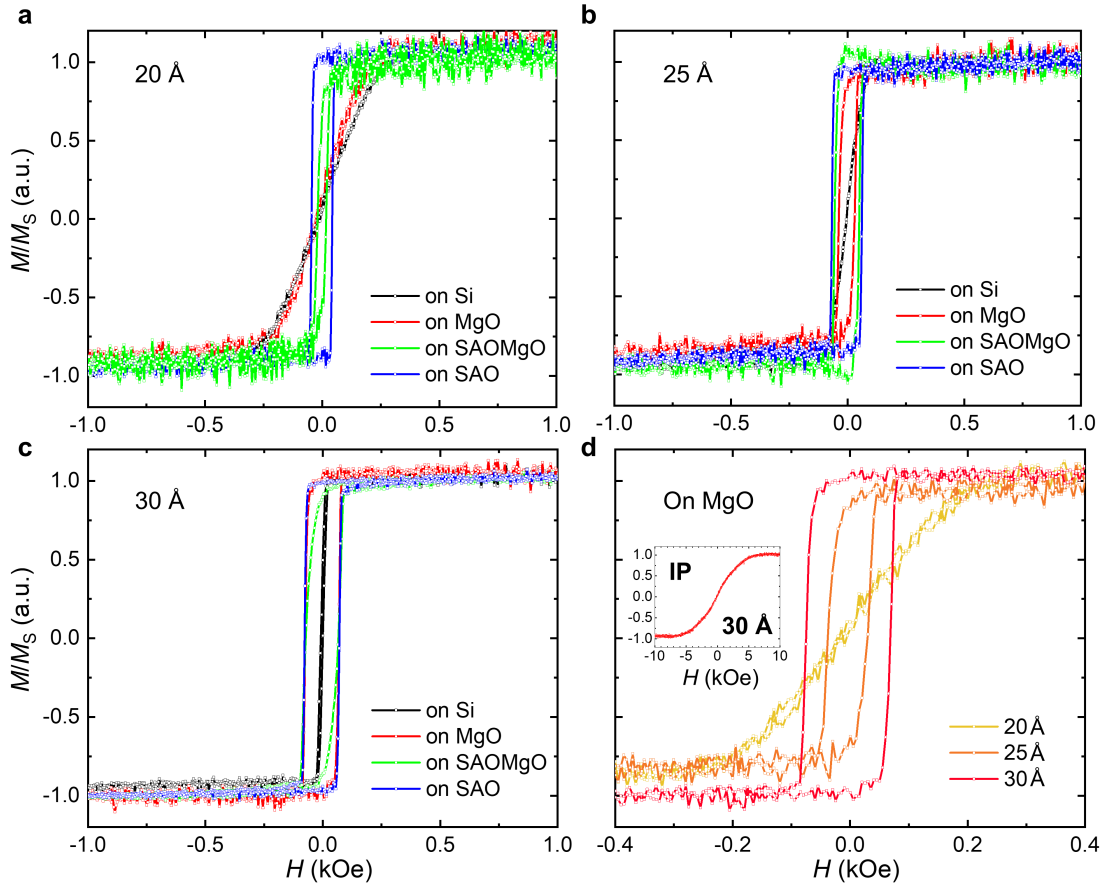

Figure 7.3: Magnetic properties of HM/FM heterostructures deposited on different substrates. **a,b,c,** Out-of-plane normalized magnetization (M/M_s) versus magnetic field (H) curves of as-deposited HM/FM heterostructures with 20 Å (**a**), 25 Å (**b**) and 30 Å (**c**) Pt layers. Different colors represent different substrates: black for Si wafer, red for MgO substrate, green for SAO/MgO bilayer, and blue for SAO thin film. **d,** Enlarged M/M_s-H curves of as-deposited HM/FM heterostructures on MgO substrates with different Pt layer thicknesses. The inset shows a typical in-plane M/M_s-H curve measured with the 30 Å Pt sample deposited on MgO.

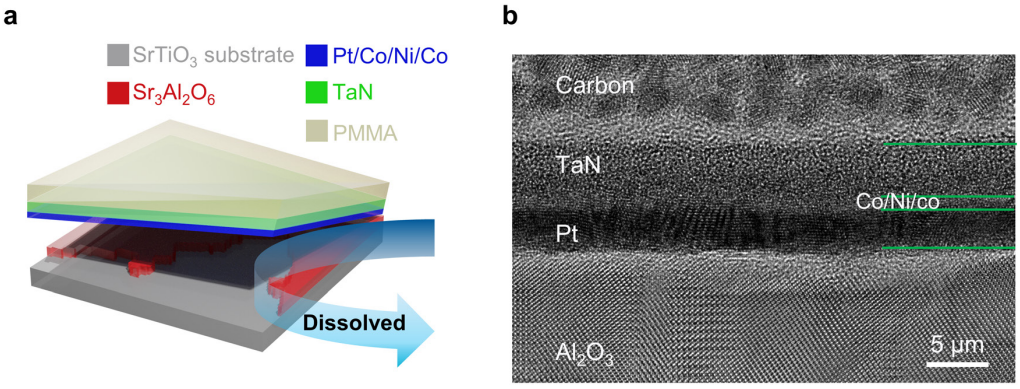

Figure 7.4: Transfer of freestanding HM/FM heterostructures without buffer layers. **a,** Schematic of the lift-off of the freestanding multilayers without MgO buffer. **b,** High-resolution cross-sectional TEM image of the freestanding HM/FM heterostructure transferred onto a sapphire substrate. Individual layers in the racetrack are clearly visible. The horizontal green lines indicate the sharp interfaces between the individual layers.

than samples' coercive fields), preventing a sharp switching of the magnetization, which is in good agreement with our VSM results. In these cases, it is difficult to create a single DW or to move a DW by current pulses, since multi-domains can be easily created by currents and the DW motion can be pinned by local defects. Interestingly, the velocity of the DW is strongly related to the rectangularity of the hysteresis loops: only when the rectangularity is good, the DW can be driven at high speeds (Fig. 7.5 b). On the other hand, when the rectangularity of the hysteresis loop is good, the thickness of the Pt layer cannot significantly affect the CIDWM behavior of the samples: freestanding racetracks without MgO buffer but with different Pt layer thicknesses show similar CIDWM behavior, which is also comparable to what we demonstrated in Chapter 5. When the Pt layer thickness is above 25 Å, the freestanding samples without any buffer layer show a fast CIDWM, which is better than the samples deposited directly on MgO or lifted off with MgO buffer. This again shows that the SAO layer can be used to stabilize the PMA of the samples and that a very thin Pt layer down to 25 Å is sufficient to protect the Co/Ni/Co heterostructures throughout the transfer and device fabrication process.

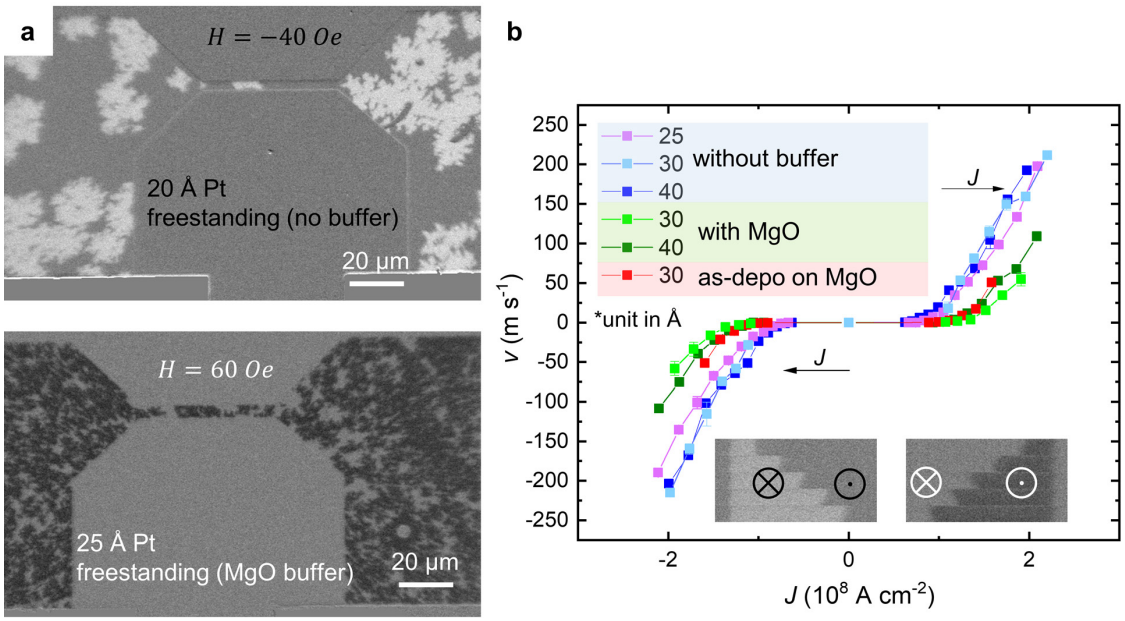

Figure 7.5: Field and current induced DW behavior in freestanding HM/FM heterostructures. **a,** Typical Kerr images of multi-domain formation in freestanding HM/FM heterostructures with (bottom) and without (top) MgO buffer driven by the external magnetic fields. The small external magnetic fields are close to their coercive fields. **b,** Current-induced DW velocity versus current density curves of freestanding HM/FM heterostructures with different Pt layer thicknesses transferred onto sapphire substrates with (purple: 25 Å Pt, light blue: 30 Å Pt, and blue: 35 Å Pt) and without MgO buffer (green: 30 Å Pt and olive: 40 Å Pt) and of as-deposited thin films on MgO with 30 Å Pt (red). The insets show typical Kerr images of DW motion in response to a series of injected 10-ns-long current pulses ($J = 1.87 \times 10^8\,\mathrm{A\,cm^{-2}}$) composed of two pulses in freestanding HM/FM multilayers with 25 Å Pt and without MgO buffer transferred onto a sapphire substrate. The bright and dark regions correspond to down ($\otimes$ or $\downarrow$) and up ($\odot$ or $\uparrow$) domains, respectively. The error bars represent the standard deviation.

To be concluded, it is possible to fabricate freestanding racetracks formed from HM/FM heterostructures even without a buffer layer.

7.3 Summary

In this chapter, we have successfully fabricated freestanding racetracks without any buffer and demonstrated fast CIDWM up to ~ 200 m s^{-1} in these racetracks. The samples deposited on SAO have a good PMA and also a comparable CIDWM behavior to the reported HM/FM thin films, which means that SAO itself can act as an effective buffer for the deposition of PMA Co/Ni/Co heterostructures. Moreover, the minimum thickness of the Pt layer can reach 25 Å, facilitating further coupling from the bottom substrates, which is promising for DW logic. On the other hand, the relationship between the crystallinity and magnetic anisotropy remains unclear and may require further investigation. In short, our results open up a new route to fabricate HM/FM racetracks directly on various kinds of bases. Next steps can be integration with patterned substrates with exotic properties, such as IP magnetic anisotropy or superconductivity.

Chapter 8

Twisted freestanding correlated oxide bi-layers

As discussed in Chapter 1, Moiré lattices have attracted much attention for their rich physical properties, such as superconductivity [2, 188, 189], which originate from non-trivial electronic correlations. Given the strong interaction between different degrees of freedom, i.e. charge, orbital, spin, and lattice, correlated oxides, which exhibit many fascinating properties, are promising for the creation of twisted structures with various novel physics (Fig. 8.1). The interface created between two stacked twisted oxide layers would lead to a spatially periodic variation of adjacent atoms across the interface, resulting in interfacial spin coupling via Moiré lattices, orbital hybridization, and charge transfer in bilayers. This complexity of Moiré lattices in correlated oxides facilitates the discovery of new phenomena and physics far beyond what can be found in epitaxial bilayers.

However, unlike 2D vdW materials, which are exfoliable and can therefore be easily used to fabricate twisted heterostructures, correlated oxide thin films, which are usually deposited by heteroepitaxy, tend to follow the in-plane structure of the substrates and are relatively difficult to form twisted structures. Thanks to the recent development of freestanding techniques (Chapter 2), the lift-off and transfer method opens up a new route to obtain twisted heterostructures. However, to date, very few reports have focused on the twisted freestanding layers, and recent investigations of twisted freestanding bi-layers have mainly focused on their structures [29, 30]. In this chapter, we will present our results on the twisted freestanding correlated oxide, LSMO ($x = 0.67$), bilayers. We will first show the realization of controllable twisted bi-layers, followed by a systematic study on their magnetic properties. We will also propose a model to explain our results.

It should be noted that the figures used in this chapter are taken from our manuscript (in preparation), for which I am the co-first author.

8.1 Controllable twisted bilayers formed from freestanding LSMO

We created a twisted LSMO bilayer by transferring a freestanding LSMO layer onto an as-deposited LSMO layer with a fixed IP angle, as schematically illustrated in Fig. 8.2 a.

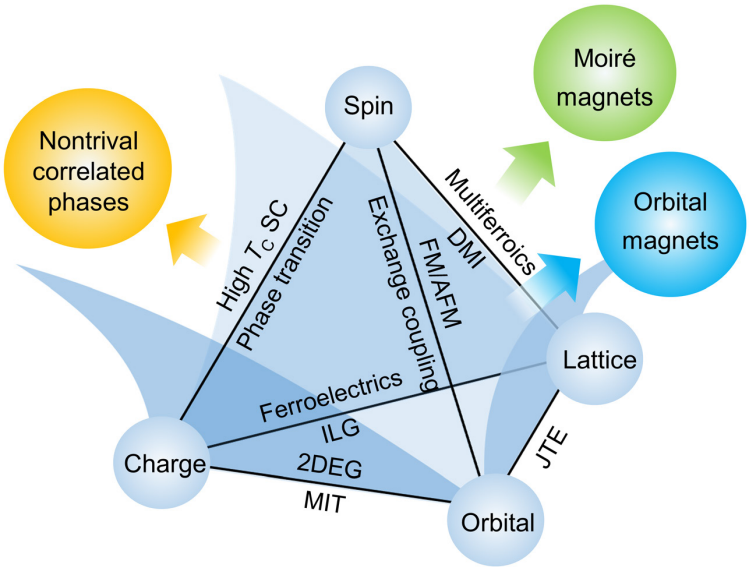

Figure 8.1: Coupling between different degrees of freedom in correlated oxides. Due to the coupling between spin, charge, orbital and lattice, correlated oxides are an intriguing family of materials that host diverse physical phenomena, such as ferromagnetic/antiferromagnetic (FM/AFM) exchange coupling, superconductivity (SC), two-dimensional electron gas (2DEG), Dzyaloshinskii-Moriya interaction (DMI), metal-insulator transition (MIT), Jahn-Teller effect (JTE), and ionic liquid gating effect (ILG).

We selected LSMO as our target material because it is half-metallic, ferromagnetic, and quite sensitive to strain and lattice reconstructions. First of all, LSMO thin films and SAO/LSMO bilayers were deposited on (110) - oriented $(La_{0.18}Sr_{0.82})(Al_{0.59}Ta_{0.41})O_3$ (LSAT) (a/2 = 3.868 Å) and STO substrates by PLD. These two types of substrates were selected for their comparable lattice parameters to LSMO (a = 3.876 Å). Due to the tensile (compressive) strain generated by STO (LSAT) substrates, an IP magnetic anisotropy of LSMO can be obtained, with an easy axis along [001] ([1-10]) and a hard axis along [1-10] ([001]), as confirmed by SQUID measurements at 10 K (Fig. 8.3 a-c). It should be noted that the magnetic anisotropy of samples deposited on SAO is weaker compared to those deposited on STO or LSAT for smaller strain from the SAO layer, as confirmed by the peak shift in the XRD θ-2θ patterns (Fig. 8.4 a). In addition, a twofold IP symmetry is formed, facilitating twisting over a wide range from 0° to 180°. Deposition of SAO was performed using the same parameters as in the previous experiments, and LSMO thin films were deposited at 750 °C, with an oxygen partial pressure of 0.2 Torr, a laser fluence of 1.1 Jcm^{-2} and a laser frequency of 6 Hz. After deposition, the samples were annealed at 600 °C in 400 Torr oxygen to eliminate oxygen vacancies. Next, using the water membrane based freestanding technique similar to that described in previous chapters, freestanding LSMO layers were transferred onto the as-deposited LSMO thin films to form twisted bilayers with controllable relative rotation between the top freestanding and bottom as-deposited LSMO layers. It should be noted that LSMO bilayers consist of LSMO layers deposited on the same substrate, e.g., freestanding LSMO released from STO was then transferred onto STO/LSMO. Fig. 8.2 a inset shows a typical 80° twisted

bilayer (STO/LSMO/twisted-LSMO), and the black and gray arrows indicate the easy axes of the freestanding and as-deposited LSMO, respectively.

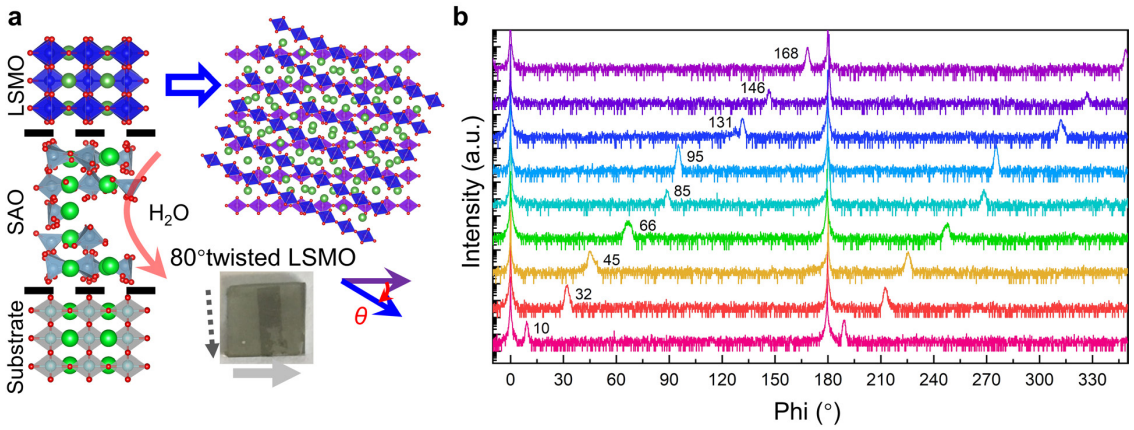

Figure 8.2: Controlled twist in LSMO bilayers fabricated from freestanding thin films. **a,** Schematic of the lift-off and transfer process. The oxygen octahedrons in purple and blue colors represent the upper freestanding and lower as-deposited LSMO layers, respectively. The twist angle θ is defined as the in-plane rotation angle between them. By controlling the relative alignment during the transfer process, twisted bilayers with different twist angles can be obtained. **b,** XRD phi scan of LSMO (002) diffraction peaks of LSMO bilayers with different twist angles. Both the lower as-deposited LSMO and the substrate contribute to the high intensity of the peaks at 0° and 180°, while additional peaks are from the upper freestanding LSMO. The different Phi peaks, marked as 10° to 168°, show the relative angle, i.e. the twist angle θ. The inset in **a** shows a typical 80° twisted bilayer LSMO and the arrows indicated the easy axes of the upper and lower LSMO layers.

The twist angle was then confirmed by XRD phi scans of the (002) diffraction peak of LSMO, which has an angle of 45° to the normal direction. As shown in Fig. 8.2 b, strong peaks at 0° and 180° correspond to the as-deposited samples, while other peaks stand for the freestanding layers. It should be noted that the substrates also contribute to the strong intensity of the peaks of the as-deposited samples due to the small lattice mismatch. We observed two peaks in one scan due to the twofold symmetry of the thin films. In short, it can be clearly seen that we have successfully realized a controllable twist from 10° to 170°.

To evaluate our deposition and transfer process, we also characterized the as-deposited thin films, twisted bilayers, and a freestanding LSMO sample transferred onto a sapphire substrate as a control experiment by OOP XRD θ-2θ scan and AFM. As shown in Fig. 8.4 a and b, peaks of SAO and LSMO can be clearly observed before transfer without any additional peaks, while only LSMO peaks exist after transfer to a sapphire substrate, indicating a successful transfer process. On the other hand, a smooth surface was achieved in the as-deposited LSMO, SAO/LSMO bilayer, and twisted bilayer with RMS roughness of 0.15, 0.37, and 0.44 nm, respectively (Fig. 8.4 c-e). The surfaces of the different layers are important for the bilayers, as they can directly affect the quality of the interface between the freestanding and as-deposited LSMO. More specifically, the top surface of the SAO layer shown in Chapter 5 (Fig. 5.2 a) will act as the bottom surface of the

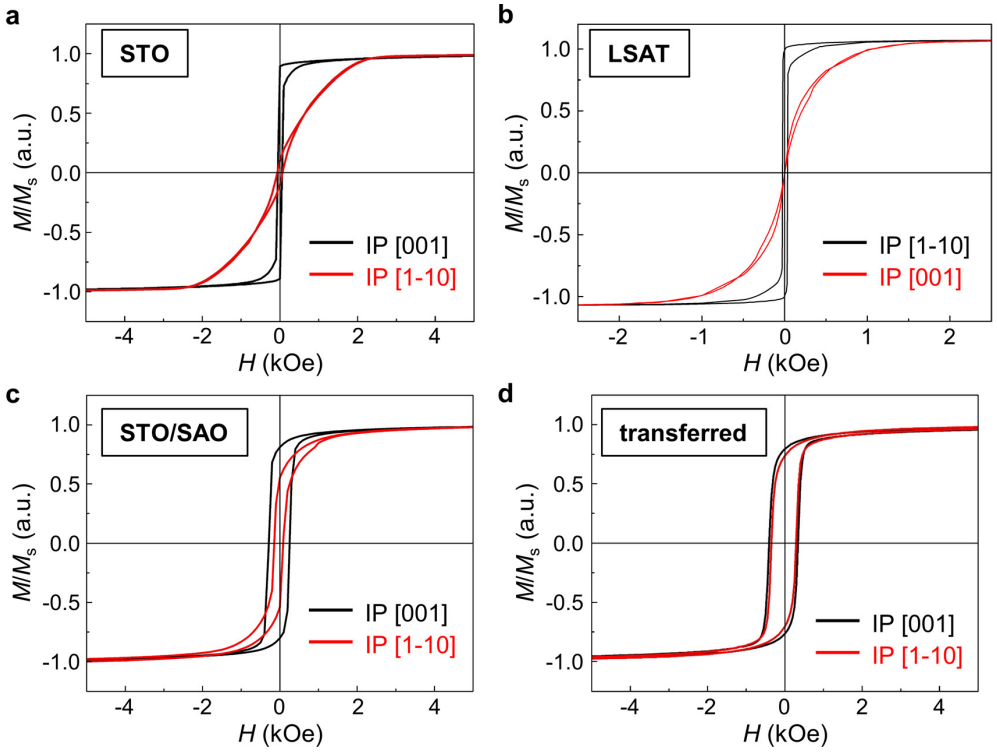

Figure 8.3: Normalized magnetization versus magnetic field loops of as-deposited LSMO on STO (110) substrate (**a**), LSAT (110) substrate (**b**) and STO/SAO bilayer (**c**), and freestanding LSMO transferred onto a sapphire substrate (**d**). The thickness of LSMO layer is 20 nm. The black and red lines represent the in-plane measurements with the magnetic field applied along the easy and hard axes of each sample, respectively.

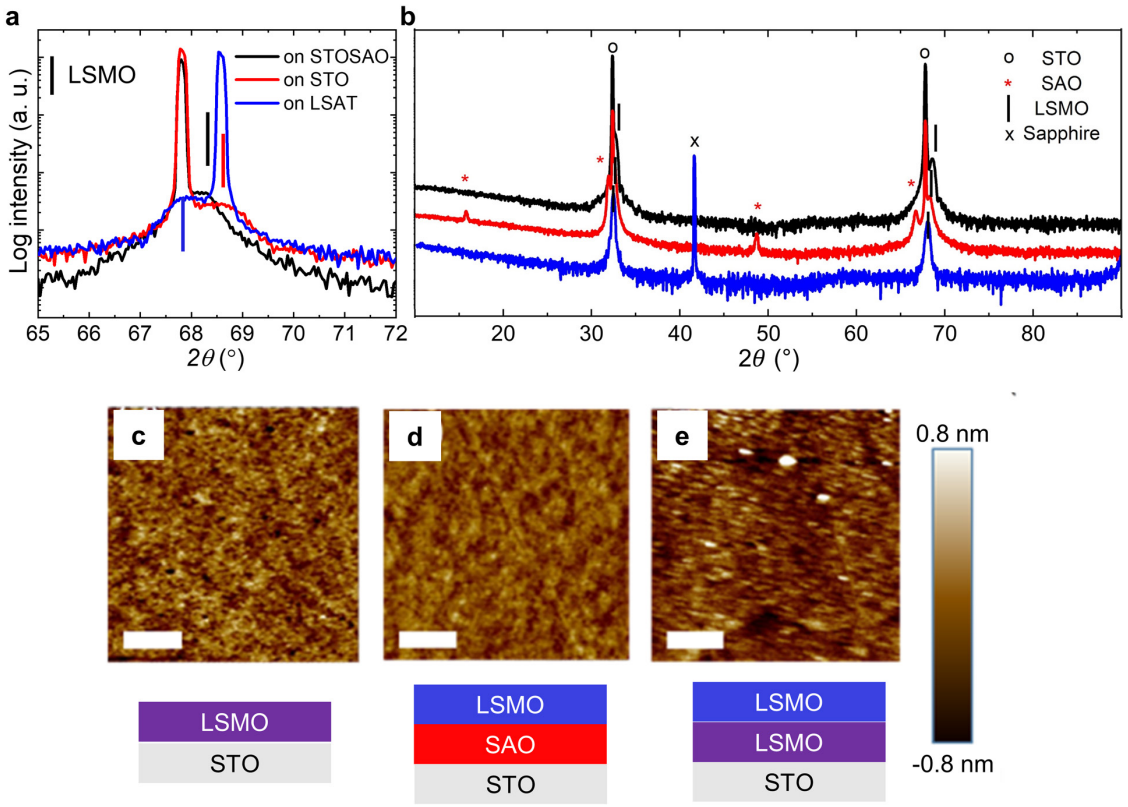

Figure 8.4: Evaluation of the lift-off and transfer process. **a,** Limited range out-of-plane θ–2θ XRD scans of LSMO deposited on different bases, including STO/SAO, STO substrate, and LSAT substrate. **b,** Full-range out-of-plane θ–2θ XRD patterns of LSMO thin films deposited on STO and STO/SAO, and a freestanding LSMO thin film transferred onto a sapphire substrate. **c**-**e**, AFM images of LSMO thin film deposited on STO, LSMO thin film deposited on STO/SAO, and twisted LSMO bilayer. Their root mean square roughness is 0.15, 0.37, and 0.44 nm, respectively. The scale bar is 1 µm.

freestanding LSMO and attach onto the top surface of the as-deposited LSMO, forming the interface. Our results on flat surfaces suggest that a high quality interface can be achieved.

Since the interface of the twisted bilayer is crucial for modulating the physical properties, we characterized the interface by cross-sectional TEM. As shown in Fig. 8.5, the interface between the upper freestanding and the lower as-deposited LSMO is continuous, indicating its good quality. The enlarged images show that the lower LSMO follows the structure and thus the orientation of the STO substrate, while the upper LSMO shows only horizontal stripes with the same OOP spacing as the lower LSMO, again confirming the relative IP rotation.

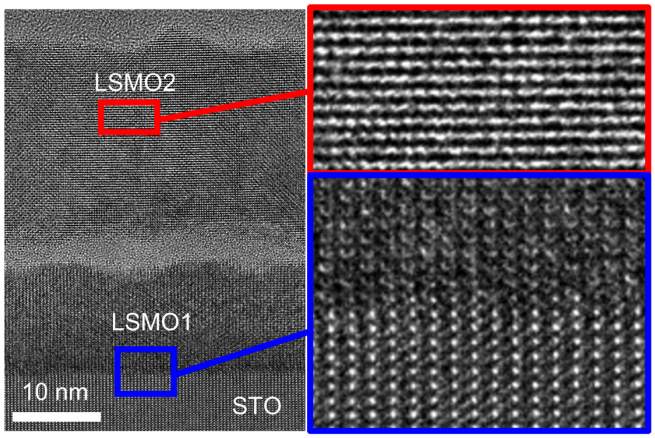

Figure 8.5: Cross-sectional TEM images of 85° twisted LSMO bilayers on STO. The right panels show magnified images. The lower layer LSMO retains the crystalline orientation of the STO substrate and shows clear lattice stripes, while the upper layer LSMO exhibits only out-of-plane spacing stripes owing to the relative rotation.

We further compared the magnetic properties of the LSMOs before and after transfer. As shown in Fig. 8.3 d, the IP magnetic anisotropy becomes weaker after transfer, which may be attributed to strain release, while the Curie temperature, which is still above room temperature, remains almost unchanged (Fig. 8.6), indicating that the ferromagnetism is well preserved after transfer.

In short, from the above characterizations, we can conclude that a twisted bilayer consisting of two LSMO layers with controllable twist angle, high-quality interface, and stable ferromagnetism has been fabricated by our freestanding technique.

8.2 Anomalous magnetization hysteresis loop of twisted LSMO bilayers

Having demonstrated the fabrication of twisted LSMO bilayers, we then focused on their magnetic properties. This is because each magnetic layer in the bilayers has a different IP orientation and thus a different magnetic anisotropy, resulting in localized interlayer magnetic coupling at the interface. A spatial distribution of local spin textures is thus

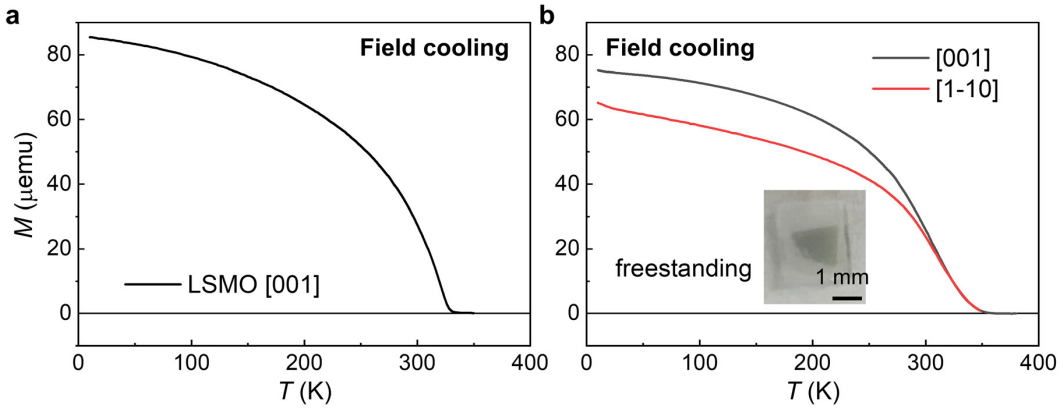

Figure 8.6: Magnetization versus temperature curves of as-deposited (**a**) and freestanding (**b**) LSMO thin films. The freestanding LSMO was transferred onto a sapphire substrate, as shown in the inset in **b**. The black and red lines represent the in-plane measurements after field cooling with the magnetic field applied along the easy and hard axes of each sample, respectively. The saturation magnetization of the freestanding thin film is smaller than that of the as-deposited one due to its smaller area compared to the as-deposited sample.

formed by localized coupling, which is either antiferromagnetic or FM coupling. First, we measured the magnetization versus field loops of twisted LSMO (12 nm)/LSMO (24 nm) bilayers on LSAT with different twist angles ranging from 10° to 90° at different temperatures. During the measurement, the magnetic field was applied along the hard axis of the lower as-deposited LSMO, i.e. [001] of the LSAT substrate, as shown in Fig. 8.3 b. Surprisingly, an anomalous diamagnetic signal is found in the hysteresis loop of each sample, showing a decrease in $|M|$ as $|H|$ increases from 0 (Fig. 8.7). The insets focus on this anomalous behavior: lines with triangular symbols show the diamagnetic phases as H decreases from 0 to -5 kOe, and solid lines show the normal behavior as H increases from -5 to 0 kOe. To illustrate this anomalous behavior more clearly, we take the anomalous hysteresis loop of the 10° twisted LSMO bilayer as an example. As shown in Fig. 8.7 a inset, as H increases in the negative direction from 1.3 to 1.5 kOe, $|M|$ also increases overall, indicating that the moments can be aligned by the external magnetic field. However, as H increases to about 1.32 kOe and 1.43 kOe in the negative direction, $|M|$ decreases with increasing $|H|$ (highlighted by red arrows), which is quite anomalous, indicating an antiparallel alignment of the moments.

Such an anomalous behavior is also found in twisted bilayers with different twist angles, but the behavior is not exactly the same. As shown in the insets of Fig. 8.7 a and b, the anomalous decrease in $|M|$ occurs only once at 45° or 90° twist, when H increases to about 0.87 kOe (45° twist) or 1.86 kOe (90° twist) in the negative direction (highlighted by red arrows). Moreover, this anomalous behavior occurs over a wide temperature range from 10 K to 100 K, while the $|H|$ of the appearance decreases with higher temperature. These results suggest that the diamagnetic phase resulting from the interlayer magnetic coupling is strongly dependent on the twist angle and temperature.

To explain this anomalous magnetization behavior, we propose that there are two types of domains with FM or antiferromagnetic coupling stabilized at the interface between the

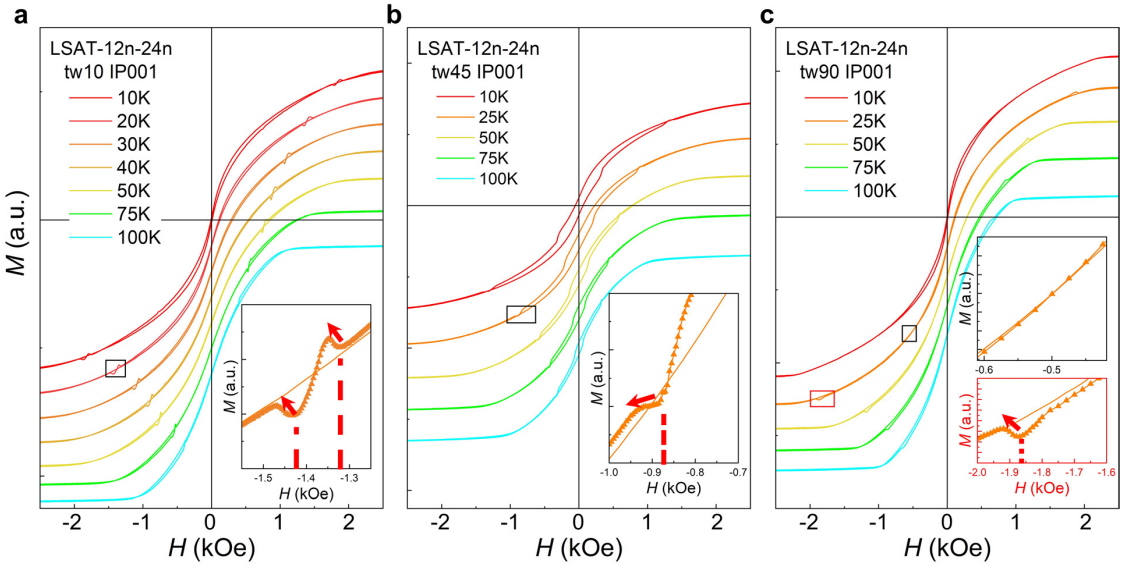

Figure 8.7: Anomalous magnetic hysteresis loops of twisted LSMO bilayers at temperatures from 10 to 100 K with different twist angles: (**a**) 10°, (**b**) 45°, (**c**) 90°. The magnetic field is applied along the hard axis of the lower as-deposited LSMO. The insets focus on the anomalous behavior. The diamagnetic signals are indicated by the red arrows, while the upper inset in **c** shows part of the hysteresis without any anomalous signal. The thickness of the upper freestanding and lower as-deposited LSMO is 24 nm and 12 nm, respectively.

upper freestanding and lower as-deposited LSMO, and the struggle between these two types of domains leads to the anomalous diamagnetic response to an external magnetic field. Here, we take the 10° twisted LSMO bilayer as an example. As shown in Fig. 8.8 a, the different states in the anomalous loops are labelled 1 (1') to 4 (4'), while the magnetic fields H_1, H_2 and H_3 correspond to the states of 1, 2 and 3. The analysis yields four effective moments $M_1 \approx M_2 < M_3 < M_4$, and the coupling effects of M_1, M_2, M_3, M_4 are schematically illustrated in the right panel of Fig. 8.7 a. As H increases to H_1, the state 1 is reached, where $+M_1$//$+M_2$ and -M_3//$+M_4$. Here, we define M_1 and M_2 as domain 1, which has FM coupling, and M_3 and M_4 as domain 2, which has antiferromagnetic coupling. As H increases to H_2, $+M_1$//-M_2 and -M_3//$+M_4$, where domain 1 is switched to antiferromagnetic coupling and thus both domain 1 and 2 have antiferromagnetic coupling, i.e. antiferromagnetic coupling is favored, leading to the decrease of magnetization and the anomalous diamagnetic behavior. As H increases to H_3, domain 2 is switched to FM coupling, leading to an increase of magnetization. In the end, as H increases to H_s, both domain 1 and 2 are switched to FM coupling, but are antiferromagnetically coupled with each other. In short, the evolution of the interlayer and intralayer antiferromagnetic coupling results in the anomalous diamagnetic behavior that is impossible in normal ferromagnetically coupled bilayers.

Since the minor loops between different fields (H_s, H_1, H_2, H_3) can reach different states with different non-volatile magnetic remanences (M_R), the twisted bilayers are promising for further applications in logic devices and multi-value memories. Therefore, we further investigated the states of M_R. By applying an external magnetic field with

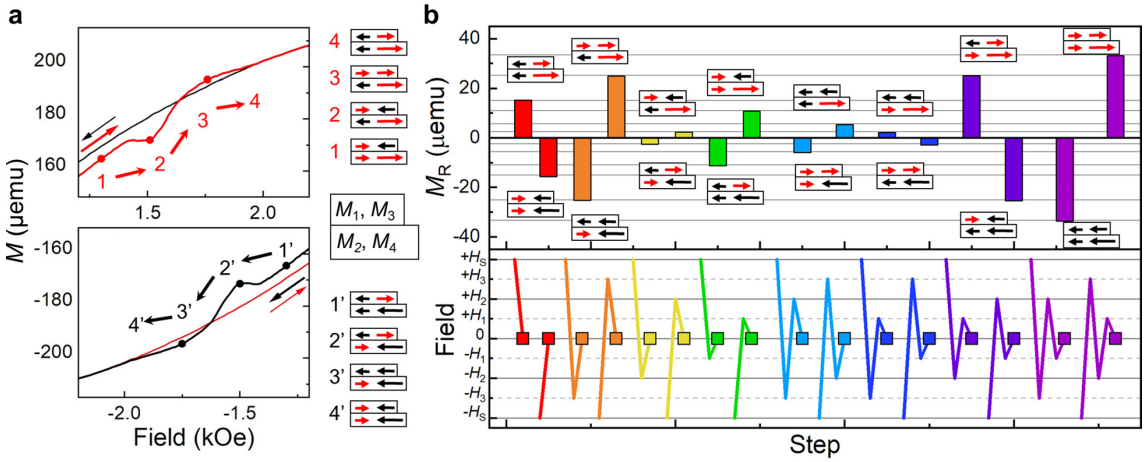

Figure 8.8: Different domain states in twisted LSMO bilayers. **a,** Magnified M-H hysteresis loops of a 10° twisted LSMO bilayer on LSAT in the positive (upper) and negative (lower) H range (1.3 kOe $< |H| <$ 2 kOe). The thickness of the upper freestanding and lower as-deposited LSMO is 24 nm and 12 nm, respectively. The scan directions are indicated by the black and red arrows. As $|H|$ sweeps from 0, the hysteresis loop undergoes different states from 1 (1') to 4 (4'). According to the different magnetic remanences (M_R) achieved at the different states 1 (1') to 4 (4'), four effective moments are given out with a relative magnitude: $M_1 \approx M_2 < M_3 < M_4$. These moments represent different domains. The coupling between these domains changes at different states, as schematically illustrated in the right panel. **b,** 2^4 states of M_R ($\pm M_1$, $\pm M_2$, $\pm M_3$, $\pm M_4$) realized by the anomalies in the hysteresis loops. The field sweeping processes between different fields (H_s, H_1, H_2, H_3) to achieve different states are shown in the lower panel. H_s is the magnetic field for saturation, corresponding to state 4 (4'), while H_1, H_2 and H_3 denote the fields corresponding to the states 1 (1'), 2 (2'), 3 (3') in **a**.

different sequences, as illustrated in Fig. 8.8 b, different states can be obtained, indicated by square symbols of different colors. The corresponding M_R values are summarized in the upper panel. It is noteworthy that 2^4 states can be obtained, resulting from different coupling effects between M_1, M_2, M_3 and M_4. The multi-value states obtained in these twisted bilayers are more than those obtained by normal coupling between two ferromagnetic layers, facilitating advanced logic devices.

8.3 Anomalous anisotropic magnetoresistance of twisted LSMO bilayers

For the magnetization to field measurements in SQUID, the entire twisted bilayer was characterized. Therefore, to exclude other contributions to the anomalous signal from the freestanding layer, we performed magnetoresistance measurements in the EBL fabricated devices in the twisted bilayer region. Fig. 8.9 a and b shows the design and an optical image of the Hall-bar device in an 85° twisted LSMO bilayer. A continuous thin film can be clearly seen in the optical image, facilitating further transport measurements. The current is applied along the Hall-bar channel fabricated along the easy axis of the lower as-deposited LSMO, i.e. the [1-10] of the LSAT substrate. The applied magnetic field is rotated in the sample plane and out of the sample plane, as shown in Fig. 8.9 c and d, respectively. The angle between the magnetic field and the current direction is defined as ω. As shown in Fig. 8.9 c and d, when the magnetic field is applied parallel to the current direction ($\omega = 0°$), a typical easy axis anisotropic magnetoresistance is found, where the magnetoresistance peaks appear at the corresponding coercive fields and the magnetoresistance generally decreases with increasing field. This is normal for ferromagnetic oxides. Interestingly, when the magnetic field is rotated to the hard axis of the lower LSMO ($\omega = 90°$), anomalous magnetoresistance responses appear in both IP and OOP cases. An additional magnetoresistance peak is found at $H = 4$ kOe with OOP magnetic field, as shown in Fig. 8.9 d. In addition, an abrupt decrease is found in both IP and OOP cases at $H = 0.6$ and 1.8 kOe, respectively. This magnetoresistance anomaly can also be attributed to the domain switching in the twisted LSMO bilayers. In short, the anomalous anisotropic magnetoresistance is again an indication of the unusual coupling effects in the twisted bilayers.

8.4 Total energy of shifted LSMO bilayers

To understand the origin of the unusual coupling effects in the twisted LSMO bilayers, we performed first-principle calculations to show the changes in the total energy of the system under different interlayer coupling conditions. To simplify the calculation, we considered a simple model: two (110) - oriented LSMO layers with a relative shift between their lattices. The lattice shift was considered along both the *a*- and *b*-axis. As schematically illustrated in Fig. 8.10 a, the shift between two lattices along the IP *b*-axis varies from 0

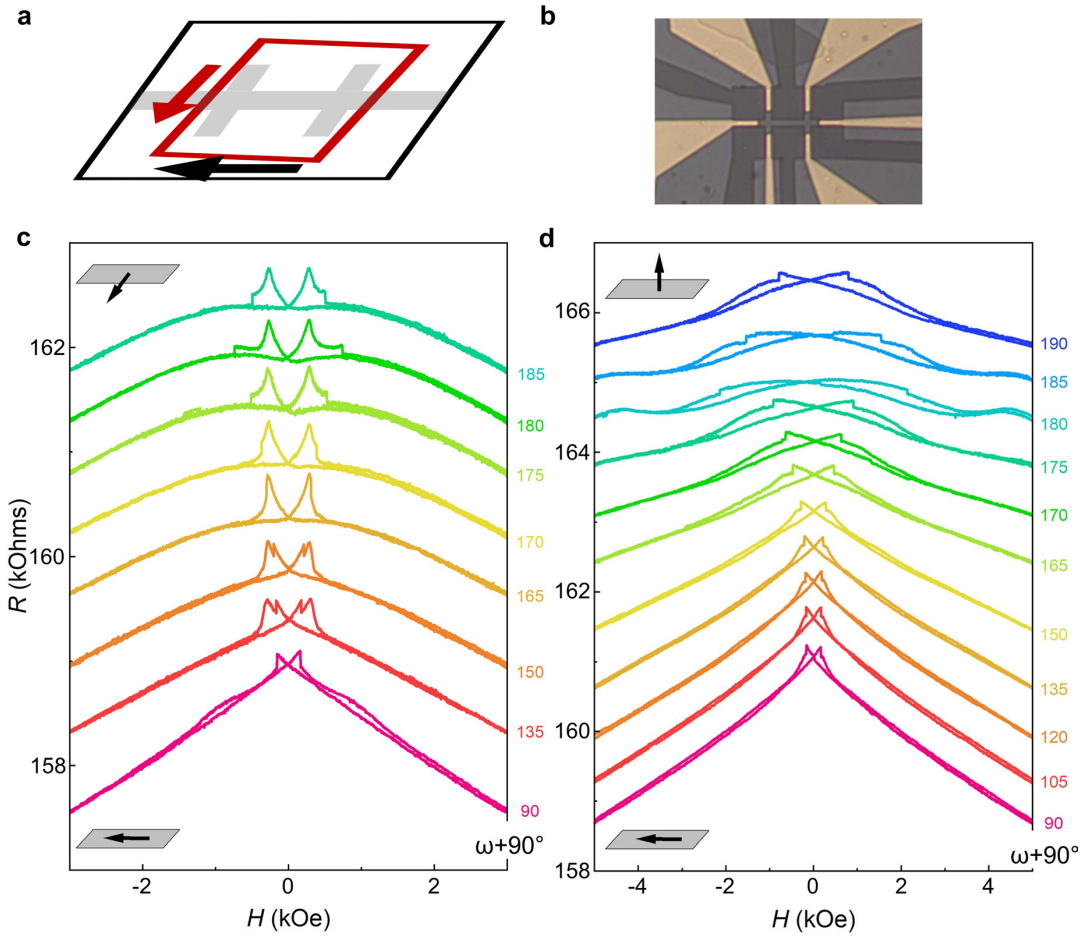

Figure 8.9: Anomalous magnetoresistance of twisted LSMO bilayers. **a,b,** Schematic (**a**) and optical image (**b**) of the Hall-bar device fabricated from a twisted LSMO bilayer (on LSAT) with a twist angle of 85°. The black and red arrows in **a** indicate the directions of the in-plane [1-10] axes of the lower and upper LSMO, respectively. Hall-bar channels were fabricated along the [1-10] axis of the lower as-deposited LSMO (easy axis of it), i.e., the direction indicated by the black arrow. **c,d,** Field dependence of magnetoresistance of 85° twisted LSMO bilayers. The external magnetic field rotates in the sample plane (**c**) and out of the sample plane (**d**). The angle between the magnetic field and the Hall-bar channel is defined as ω. The rotation of the magnetic field is shown schematically in the insets.

to 1 u.c. The oxygen octahedrons in purple and blue colors represent the upper and lower LSMO layers, respectively. For different lattice shifts, the energy of the system with interlayer FM or antiferromagnetic coupling was calculated, as shown in Fig. 8.10 b. The energy of the system with interlayer FM coupling is lower than with antiferromagnetic coupling when the lattice shift is 0 u.c. and 1 u.c., whereas antiferromagnetic coupling becomes energetically favored compared to FM coupling when the lattice shift is 0.5 u.c. (Fig. 8.10 b insets). To show the energetically favored coupling more clearly, the energy difference between antiferromagnetic and FM coupling ($dE = E_{\text{Antiferromagnetic}} - E_{\text{FM}}$) is plotted against the lattice shift from 0 to 1 u.c. along the *b*-axis (Fig. 8.10 c) and the *a*-axis (Fig. 8.10 d). As shown in Fig. 8.10 c, when the lattice shift is 0 u.c., i.e. the initial state, dE reaches the maximum and generally decreases with increasing lattice shift until the lattice shift reaches 0.38 u.c., indicating that FM coupling is favored at lattice shifts smaller than 0.38 u.c. dE becomes negative as the lattice shift varies from 0.38 - 0.62 u.c., indicating that antiferromagnetic coupling is favored at lattice shifts in this range. As the lattice shift is further increased, dE becomes positive again. In contrast, when the lattice shift is along the *a*-axis, dE is always positive when the lattice shift varies from 0 to 1 u.c. (Fig. 8.10 d), indicating that FM coupling is always favored in this case. From the above calculations, we suggest that antiferromagnetic coupling at the interface between the freestanding LSMO and the as-deposited LSMO could be energetically favored in some regions due to lattice shifts. Considering that the formation of the Moiré lattice in twisted bilayers would induce periodic lattice shifts, antiferromagnetic coupling could dominate in some domains, leading to the anomalous diamagnetic behavior; on the other hand, FM coupling dominates in most domains, contributing to the large FM responses.

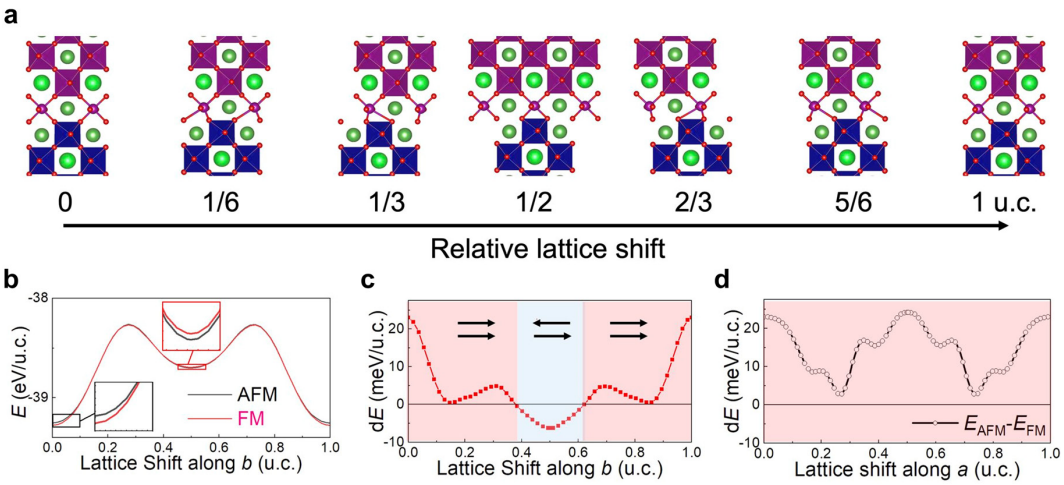

Figure 8.10: Antiferromagnetic and FM coupling in shifted LSMO bilayers. **a,** Schematic of the interface between two (110) - oriented LSMO layers with different lattice shifts along the *b*-axis. **b,** Dependence of total energy on the lattice shift along the *b*-axis for the cases with interlayer antiferromagnetic (AFM) and FM coupling. **c,d,** Energy difference between the calculated total energies of the bilayer with interlayer AFM coupling and the bilayer with interlayer FM coupling as a function of the lattice shift along the *b*-axis (**c**) and *a*-axis (**d**).

8.5 Summary

In this chapter, we have successfully fabricated twisted magnetic LSMO bilayers with controllable twist angles from freestanding LSMO layers using our water membrane based freestanding technique. The spin dependent magnetic coupling in the twisted bilayers is investigated by magnetization and magnetoresistance measurements. Anomalous diamagnetic behavior is found in the twisted bilayers, which can be attributed to the interlayer antiferromagnetic coupling. A simple lattice shift model can be used to explain the energetically favored antiferromagnetic coupling. In addition, multi-value states can be achieved in the twisted bilayers, facilitating further applications in novel memory devices. Given the large family of correlated oxides, twisted oxides remain a largely unexplored field, in which various kinds of interfacial couplings between superconductivity, magnetism, polarization, etc. can be studied.

Chapter 9

Conclusion and outlook

In this thesis, I have summarized our studies on several different types of freestanding heterostructures prepared by our water membrane based freestanding technique, including freestanding HM/FM and SAF heterostructures for magnetic RTM devices and twisted LSMO bilayers that exhibit anomalous magnetization hysteresis.

First, we demonstrated a successful deposition and transfer of freestanding HM/FM heterostructures by dissolving the water-soluble SAO sacrificial layer, as confirmed by our structural characterizations including AFM, XRD, and cross-sectional TEM. The magnetic and transport properties of the freestanding thin films remain almost unchanged after the lift-off and device fabrication, which is consistent with the CIDWM behavior in 2D racetracks formed from these structures.

Based on the above results, we took advantage of the freestanding thin films, which can be transferred onto various kinds of bases, to first demonstrate that the freestanding membranes follow closely the underlying structures formed on the bases to thereby form 3D racetracks. These racetracks were created by covering 3D protrusions created on a substrate with the freestanding HM/FM heterostructures. The height of the protrusions was varied from the nanometer to the micrometer scale. It was shown that the CIDWM can be controlled by the local geometry of these protrusions. By changing the angle between the racetrack channel and the protrusion, different types of chiral DWs can be selectively moved across the protrusion, thus realizing a DW 'diode' device. We further investigated 3D racetracks formed from freestanding SAF structures. Due to the symmetry and large ECT of SAFs, fast CIDWM can be realized in such SAF structures. The maximum DW velocity of up to 600 m s^{-1} is similar to that of racetracks formed from the as-deposited SAFs.

We then eliminated the MgO buffer layer used to support the HM/FM heterostructures and reduced the thickness of the bottom HM, Pt. We have shown that the SAO layer itself can act as an effective buffer to support the PMA of the HM/FM heterostructures and that the PMA remains intact after the lift-off and transfer process. Comparable device performance to that of conventional HM/FM racetracks was found in racetracks formed from HM/FM heterostructures with a very thin Pt layer down to 25 Å and without the MgO buffer.

We also utilized the water membrane based freestanding technique to create twisted LSMO bilayers with a controllable twist angle as confirmed by XRD measurements. The twisted bilayers exhibit an anomalous diamagnetic behavior, which is a result of the antiferromagnetic coupling at the twisted interface. We proposed a model to explain the energetically favored antiferromagnetic coupling. Furthermore, multivalued magnetization states can be realized in twisted bilayers.

In conclusion, we have demonstrated the versatility of our method to fabricate freestanding membranes. The freestanding racetracks show great potential for the realization of spintronic memories and DW logics. The demonstration of racetracks in the third dimension is an important milestone in the advancement of RTM. Moreover, twisted oxides as demonstrated here are intriguing not only for their applications such as multivalued memory, but also for their emergent phenomena owing to abundant interfacial couplings.

Since the freestanding heterostructures can be integrated with many other material systems or patterned structures, the next step could be to integrate freestanding racetracks with patterned thin films to create more complex functionalities. In addition, considering the rich properties revealed so far in 2D vdW Moiré lattices, the rarely explored twisted correlated oxides hold great promise for stimulating new scientific and engineering discoveries. Twisted freestanding layers consisting of superconducting or antiferromagnetic oxides are also of interest. On the other hand, the uptake of freestanding membranes in applications may not occur in the short term, as fabrication methods need to be further improved to obtain wafer-size crack-free freestanding membranes. The exploration of freestanding heterostructures continues apace, leading to a growing family of novel structures with the emergence of intriguing properties.

Appendix A

List of Materials

List of Material Abbreviations	
BAO	$Ba_3Al_2O_6$
BFO	$BiFeO_3$
BTO	$BaTiO_3$
CFO	$CoFe_2O_4$
LAO	$LaAlO_3$
LiPON	Lithium phosphorus oxynitride
LSAT	$(La_{0.18}Sr_{0.82})(Al_{0.59}Ta_{0.41})O_3$
LSMO	$La_xSr_{1-x}MnO_3$
PDMS	Poly(dimethylsiloxane)
PET	Poly(ethylene terephthalate)
PI	Polyimide
PLZT	$(Pb, La)(Zr, Ti)O_3$
PMMA	Polymethyl-methacrylate
PTO	$PbTiO_3$
PZT	$Pb(Zr_{0.2}Ti_{0.8})O_3$
SAO	$Sr_3Al_2O_6$
SCO	$SrCoO_{2.5}$
SRO	$SrRuO_3$
STO	$SrTiO_3$
SVO	$SrVO_3$
YBCO	$YBa_2Cu_3O_{6+\delta}$

List of Figures

List of Tables

Bibliography

[1] Feynman, R.P. An invitation to enter a new field of physics. *International Journal of Engineering Science* **23**(8) (1960).

[2] Cao, Y., Fatemi, V., Fang, S., Watanabe, K., Taniguchi, T., Kaxiras, E., and Jarillo-Herrero, P. Unconventional superconductivity in magic-angle graphene superlattices. *Nature* **556**(7699), 43–50 (2018).

[3] Bednorz, J.G. and Müller, K.A. Possible high T_c superconductivity in the Ba−La−Cu−O system. *Zeitschrift für Physik B Condensed Matter* **64**(2), 189–193 (1986).

[4] Li, L., Richter, C., Mannhart, J., and Ashoori, R. Coexistence of magnetic order and two-dimensional superconductivity at $LaAlO_3/SrTiO_3$ interfaces. *Nature Physics* **7**(10), 762–766 (2011).

[5] Lu, H., Bark, C.W., Esque De Los Ojos, D., Alcala, J., Eom, C.B., Catalan, G., and Gruverman, A. Mechanical writing of ferroelectric polarization. *Science* **336**(6077), 59–61 (2012).

[6] Iijima, K., Terashima, T., Yamamoto, K., Hirata, K., and Bando, Y. Preparation of ferroelectric $BaTiO_3$ thin films by activated reactive evaporation. *Applied Physics Letters* **56**(6), 527–529 (1990).

[7] Singh, D.J. Electronic and magnetic properties of the 4d itinerant ferromagnet $SrRuO_3$. *Journal of Applied Physics* **79**(8), 4818–4820 (1996).

[8] Liu, S., Yuan, X., Zou, Y., Sheng, Y., Huang, C., Zhang, E., Ling, J., Liu, Y., Wang, W., Zhang, C., et al. Wafer-scale two-dimensional ferromagnetic Fe_3GeTe_2 thin films grown by molecular beam epitaxy. *npj 2D Materials and Applications* **1**(1), 30 (2017).

[9] Zhao, T., Scholl, A., Zavaliche, F., Lee, K., Barry, M., Doran, A., Cruz, M., Chu, Y., Ederer, C., Spaldin, N., et al. Electrical control of antiferromagnetic domains in multiferroic $BiFeO_3$ films at room temperature. *Nature Materials* **5**(10), 823–829 (2006).

[10] Venkatesan, T. Pulsed laser deposition—invention or discovery? *Journal of Physics D: Applied Physics* **47**(3), 034001 (2013).

[11] Yang, A.J., Han, K., Huang, K., Ye, C., Wen, W., Zhu, R., Zhu, R., Xu, J., Yu, T., Gao, P., et al. Van der Waals integration of high-κ perovskite oxides and two-dimensional semiconductors. *Nature Electronics* **5**(4), 233–240 (2022).

[12] Faber, K.T., Asefa, T., Backhaus-Ricoult, M., Brow, R., Chan, J.Y., Dillon, S., Fahrenholtz, W.G., Finnis, M.W., Garay, J.E., García, R.E., et al. The role of ceramic and glass science research in meeting societal challenges: Report from an NSF-sponsored workshop. *Journal of the American Ceramic Society* **100**(5), 1777–1803 (2017).

[13] Koma, A. Van der Waals epitaxy—a new epitaxial growth method for a highly lattice-mismatched system. *Thin Solid Films* **216**(1), 72–76 (1992).

[14] Kum, H.S., Lee, H., Kim, S., Lindemann, S., Kong, W., Qiao, K., Chen, P., Irwin, J., Lee, J.H., Xie, S., et al. Heterogeneous integration of single-crystalline complex-oxide membranes. *Nature* **578**(7793), 75–81 (2020).

[15] Lipomi, D.J., Vosgueritchian, M., Tee, B.C., Hellstrom, S.L., Lee, J.A., Fox, C.H., and Bao, Z. Skin-like pressure and strain sensors based on transparent elastic films of carbon nanotubes. *Nature Nanotechnology* **6**(12), 788–792 (2011).

[16] Hammock, M.L., Chortos, A., Tee, B.C.K., Tok, J.B.H., and Bao, Z. 25th anniversary article: The evolution of electronic skin (e-skin): A brief history, design considerations, and recent progress. *Advanced Materials* **25**(42), 5997–6038 (2013).

[17] Hall, P., Morabito, J., and Panousis, N. Interdiffusion in the Cu – Au thin film system at 25 °C to 250 °C. *Thin Solid Films* **41**(3), 341–361 (1977).

[18] Chambers, S.A. Understanding the mechanism of conductivity at the $LaAlO_3/SrTiO_3$ (001) interface. *Surface Science* **605**(13-14), 1133–1140 (2011).

[19] Dho, J., Kim, Y., Hwang, Y., Kim, J., and Hur, N. Strain-induced magnetic stripe domains in $La_{0.7}Sr_{0.3}MnO_3$ thin films. *Applied Physics Letters* **82**(9), 1434–1436 (2003).

[20] Sato, H. and Naito, M. Increase in the superconducting transition temperature by anisotropic strain effect in (001) $La_{1.85}Sr_{0.15}CuO_4$ thin films on $LaSrAlO_4$ substrates. *Physica C: Superconductivity* **274**(3-4), 221–226 (1997).

[21] Liang, S.J., Cheng, B., Cui, X., and Miao, F. Van der Waals heterostructures for high-performance device applications: Challenges and opportunities. *Advanced Materials* **32**(27), 1903800 (2020).

[22] Cao, Y., Fatemi, V., Demir, A., Fang, S., Tomarken, S.L., Luo, J.Y., Sanchez-Yamagishi, J.D., Watanabe, K., Taniguchi, T., Kaxiras, E., et al. Correlated insulator behaviour at half-filling in magic-angle graphene superlattices. *Nature* **556**(7699), 80–84 (2018).

[23] Chen, S., He, M., Zhang, Y.H., Hsieh, V., Fei, Z., Watanabe, K., Taniguchi, T., Cobden, D.H., Xu, X., Dean, C.R., et al. Electrically tunable correlated and topological states in twisted monolayer–bilayer graphene. *Nature Physics* **17**(3), 374–380 (2021).

[24] Regan, E.C., Wang, D., Paik, E.Y., Zeng, Y., Zhang, L., Zhu, J., MacDonald, A.H., Deng, H., and Wang, F. Emerging exciton physics in transition metal dichalcogenide heterobilayers. *Nature Reviews Materials* **7**(10), 778–795 (2022).

[25] Wang, L., Shih, E.M., Ghiotto, A., Xian, L., Rhodes, D.A., Tan, C., Claassen, M., Kennes, D.M., Bai, Y., Kim, B., et al. Correlated electronic phases in twisted bilayer transition metal dichalcogenides. *Nature Materials* **19**(8), 861–866 (2020).

[26] Telford, E.J., Dismukes, A.H., Dudley, R.L., Wiscons, R.A., Lee, K., Chica, D.G., Ziebel, M.E., Han, M.G., Yu, J., Shabani, S., et al. Coupling between magnetic order and charge transport in a two-dimensional magnetic semiconductor. *Nature Materials* **21**(7), 754–760 (2022).

[27] Gong, C., Li, L., Li, Z., Ji, H., Stern, A., Xia, Y., Cao, T., Bao, W., Wang, C., Wang, Y., et al. Discovery of intrinsic ferromagnetism in two-dimensional van der Waals crystals. *Nature* **546**(7657), 265–269 (2017).

[28] Ji, D., Cai, S., Paudel, T.R., Sun, H., Zhang, C., Han, L., Wei, Y., Zang, Y., Gu, M., Zhang, Y., et al. Freestanding crystalline oxide perovskites down to the monolayer limit. *Nature* **570**(7759), 87–90 (2019).

[29] Shen, J., Dong, Z., Qi, M., Zhang, Y., Zhu, C., Wu, Z., and Li, D. Observation of Moiré patterns in twisted stacks of bilayer perovskite oxide nanomembranes with various lattice symmetries. *ACS Applied Materials & Interfaces* **14**(44), 50386–50392 (2022).

[30] Li, Y., Xiang, C., Chiabrera, F.M., Yun, S., Zhang, H., Kelly, D.J., Dahm, R.T., Kirchert, C.K., Cozannet, T.E.L., Trier, F., et al. Stacking and twisting of freestanding complex oxide thin films. *Advanced Materials* **34**(38), 2203187 (2022).

[31] Luo, Z.D., Peters, J.J., Sanchez, A.M., and Alexe, M. Flexible memristors based on single-crystalline ferroelectric tunnel junctions. *ACS Applied Materials & Interfaces* **11**(26), 23313–23319 (2019).

[32] Huang, J.K., Wan, Y., Shi, J., Zhang, J., Wang, Z., Wang, W., Yang, N., Liu, Y., Lin, C.H., Guan, X., et al. High-κ perovskite membranes as insulators for two-dimensional transistors. *Nature* **605**(7909), 262–267 (2022).

[33] Guo, R., You, L., Lin, W., Abdelsamie, A., Shu, X., Zhou, G., Chen, S., Liu, L., Yan, X., Wang, J., et al. Continuously controllable photoconductance in freestanding $BiFeO_3$ by the macroscopic flexoelectric effect. *Nature Communications* **11**(1), 2571 (2020).

[34] Cai, S., Lun, Y., Ji, D., Lv, P., Han, L., Guo, C., Zang, Y., Gao, S., Wei, Y., Gu, M., et al. Enhanced polarization and abnormal flexural deformation in bent freestanding perovskite oxides. *Nature Communications* **13**(1), 5116 (2022).

[35] Luo, Z., Hrabec, A., Dao, T.P., Sala, G., Finizio, S., Feng, J., Mayr, S., Raabe, J., Gambardella, P., and Heyderman, L.J. Current-driven magnetic domain-wall logic. *Nature* **579**(7798), 214–218 (2020).

[36] Tsakalakos, L. and Sands, T. Epitaxial ferroelectric $(Pb, La)(Zr, Ti)O_3$ thin films on stainless steel by excimer laser liftoff. *Applied Physics Letters* **76**(2), 227–229 (2000).

[37] Ghoneim, M.T., Zidan, M.A., Alnassar, M.Y., Hanna, A.N., Kosel, J., Salama, K.N., and Hussain, M.M. Thin PZT-based ferroelectric capacitors on flexible silicon for nonvolatile memory applications. *Advanced Electronic Materials* **1**(6), 1500045 (2015).

[38] Chu, Y.H. Van der Waals oxide heteroepitaxy. *npj Quantum Materials* **2**(1), 67 (2017).

[39] Bitla, Y. and Chu, Y.H. MICAtronics: A new platform for flexible X-tronics. *FlatChem* **3**, 26–42 (2017).

[40] Bitla, Y. and Chu, Y.H. van der Waals oxide heteroepitaxy for soft transparent electronics. *Nanoscale* **12**(36), 18523–18544 (2020).

[41] Konagai, M., Sugimoto, M., and Takahashi, K. High efficiency GaAs thin film solar cells by peeled film technology. *Journal of Crystal Growth* **45**, 277–280 (1978).

[42] Gan, Q., Rao, R., Eom, C., Garrett, J., and Lee, M. Direct measurement of strain effects on magnetic and electrical properties of epitaxial $SrRuO_3$ thin films. *Applied Physics Letters* **72**(8), 978–980 (1998).

[43] Paskiewicz, D.M., Sichel-Tissot, R., Karapetrova, E., Stan, L., and Fong, D.D. Single-crystalline $SrRuO_3$ nanomembranes: A platform for flexible oxide electronics. *Nano Letters* **16**(1), 534–542 (2016).

[44] Bakaul, S.R., Serrao, C.R., Lee, M., Yeung, C.W., Sarker, A., Hsu, S.L., Yadav, A.K., Dedon, L., You, L., Khan, A.I., et al. Single crystal functional oxides on silicon. *Nature Communications* **7**(1), 10547 (2016).

[45] Lin, Y., Zeng, T., Xu, H., Wang, Z., Zhao, X., Liu, W., Ma, J., and Liu, Y. Transferable and flexible artificial memristive synapse based on WO_x schottky junction on arbitrary substrates. *Advanced Electronic Materials* **4**(12), 1800373 (2018).

[46] Shen, L., Wu, L., Sheng, Q., Ma, C., Zhang, Y., Lu, L., Ma, J., Ma, J., Bian, J., Yang, Y., et al. Epitaxial lift-off of centimeter-scaled spinel ferrite oxide thin films for flexible electronics. *Advanced Materials* **29**(33), 1702411 (2017).

[47] Bakaul, S.R., Kim, J., Hong, S., Cherukara, M.J., Zhou, T., Stan, L., Serrao, C.R., Salahuddin, S., Petford-Long, A.K., Fong, D.D., et al. Ferroelectric domain wall motion in freestanding single-crystal complex oxide thin film. *Advanced Materials* **32**(4), 1907036 (2020).

[48] Bakaul, S.R., Prokhorenko, S., Zhang, Q., Nahas, Y., Hu, Y., Petford-Long, A., Bellaiche, L., and Valanoor, N. Freestanding ferroelectric bubble domains. *Advanced Materials* **33**(45), 2105432 (2021).

[49] Pesquera, D., Parsonnet, E., Qualls, A., Xu, R., Gubser, A.J., Kim, J., Jiang, Y., Velarde, G., Huang, Y.L., Hwang, H.Y., et al. Beyond substrates: Strain engineering of ferroelectric membranes. *Advanced Materials* **32**(43), 2003780 (2020).

[50] Elangovan, H., Barzilay, M., Seremi, S., Cohen, N., Jiang, Y., Martin, L.W., and Ivry, Y. Giant superelastic piezoelectricity in flexible ferroelectric $BaTiO_3$ membranes. *ACS Nano* **14**(4), 5053–5060 (2020).

[51] Bakaul, S.R., Serrao, C.R., Lee, O., Lu, Z., Yadav, A., Carraro, C., Maboudian, R., Ramesh, R., and Salahuddin, S. High speed epitaxial perovskite memory on flexible substrates. *Advanced Materials* **29**(11) (2017).

[52] Pesquera, D., Khestanova, E., Ghidini, M., Zhang, S., Rooney, A.P., Maccherozzi, F., Riego, P., Farokhipoor, S., Kim, J., Moya, X., et al. Large magnetoelectric coupling in multiferroic oxide heterostructures assembled via epitaxial lift-off. *Nature Communications* **11**(1), 3190 (2020).

[53] Eom, K., Yu, M., Seo, J., Yang, D., Lee, H., Lee, J.W., Irvin, P., Oh, S.H., Levy, J., and Eom, C.B. Electronically reconfigurable complex oxide heterostructure freestanding membranes. *Science Advances* **7**(33), eabh1284 (2021).

[54] Kim, S.I., Choi, H.J., Lee, G., Roh, C.J., Jung, I., Jung, S.Y., Ning, R., Won, S.O., Chang, H.J., Lee, J.S., et al. 3d architectures of single-crystalline complex oxides. *Materials Horizons* **7**(6), 1552–1557 (2020).

[55] Peng, H., Lu, N., Yang, S., Lyu, Y., Liu, Z., Bu, Y., Shen, S., Li, M., Li, Z., Gao, L., et al. A generic sacrificial layer for wide-range freestanding oxides with modulated magnetic anisotropy. *Advanced Functional Materials* **32**(28), 2111907 (2022).

[56] Takahashi, R. and Lippmaa, M. Sacrificial water-soluble BaO layer for fabricating free-standing piezoelectric membranes. *ACS Applied Materials & Interfaces* **12**(22), 25042–25049 (2020).

[57] Harada, T. and Tsukazaki, A. A versatile patterning process based on easily soluble sacrificial bilayers. *AIP Advances* **7**(8) (2017).

[58] Zhang, Y., Shen, L., Liu, M., Li, X., Lu, X., Lu, L., Ma, C., You, C., Chen, A., Huang, C., et al. Flexible quasi-two-dimensional $CoFe_2O_4$ epitaxial thin films

for continuous strain tuning of magnetic properties. *ACS Nano* **11**(8), 8002–8009 (2017).

[59] Shen, L., Liu, M., Ma, C., Lu, L., Fu, H., You, C., Lu, X., and Jia, C.L. Enhanced bending-tuned magnetic properties in epitaxial cobalt ferrite nanopillar arrays on flexible substrates. *Materials Horizons* **5**(2), 230–239 (2018).

[60] Banerjee, N., Houwman, E.P., Koster, G., and Rijnders, G. Fabrication of piezo-driven, free-standing, all-oxide heteroepitaxial cantilevers on silicon. *APL Materials* **2**(9) (2014).

[61] Banerjee, N., Huijben, M., Koster, G., and Rijnders, G. Direct patterning of functional interfaces in oxide heterostructures. *Applied Physics Letters* **100**(4) (2012).

[62] Li, X., Yin, Z., Zhang, X., Wang, Y., Wang, D., Gao, M., Meng, J., Wu, J., and You, J. Epitaxial liftoff of wafer-scale VO_2 nanomembranes for flexible, ultrasensitive tactile sensors. *Advanced Materials Technologies* **4**(7), 1800695 (2019).

[63] Rogers, D., Hosseini Teherani, F., Ougazzaden, A., Gautier, S., Divay, L., Lusson, A., Durand, O., Wyczisk, F., Garry, G., Monteiro, T., et al. Use of ZnO thin films as sacrificial templates for metal organic vapor phase epitaxy and chemical lift-off of GaN. *Applied Physics Letters* **91**(7) (2007).

[64] Lee, D.K., Park, Y., Sim, H., Park, J., Kim, Y., Kim, G.Y., Eom, C.B., Choi, S.Y., and Son, J. Heterogeneous integration of single-crystalline rutile nanomembranes with steep phase transition on silicon substrates. *Nature Communications* **12**(1), 5019 (2021).

[65] Bakaul, S.R. Electrical characterization of freestanding complex oxide ferroelectrics: Artifacts and experimental precautions. *AIP Advances* **11**(11) (2021).

[66] Lu, D., Baek, D.J., Hong, S.S., Kourkoutis, L.F., Hikita, Y., and Hwang, H.Y. Synthesis of freestanding single-crystal perovskite films and heterostructures by etching of sacrificial water-soluble layers. *Nature Materials* **15**(12), 1255–1260 (2016).

[67] Hong, S.S., Yu, J.H., Lu, D., Marshall, A.F., Hikita, Y., Cui, Y., and Hwang, H.Y. Two-dimensional limit of crystalline order in perovskite membrane films. *Science Advances* **3**(11), eaao5173 (2017).

[68] Han, L., Fang, Y., Zhao, Y., Zang, Y., Gu, Z., Nie, Y., and Pan, X. Giant uniaxial strain ferroelectric domain tuning in freestanding $PbTiO_3$ films. *Advanced Materials Interfaces* **7**(7), 1901604 (2020).

[69] Dong, G., Li, S., Yao, M., Zhou, Z., Zhang, Y.Q., Han, X., Luo, Z., Yao, J., Peng, B., Hu, Z., et al. Super-elastic ferroelectric single-crystal membrane with continuous electric dipole rotation. *Science* **366**(6464), 475–479 (2019).

[70] Han, K., Wu, L., Cao, Y., Wang, H., Ye, C., Huang, K., Motapothula, M., Xing, H., Li, X., Qi, D.C., et al. Enhanced metal–insulator transition in freestanding VO_2 down to 5 nm thickness. *ACS Applied Materials & Interfaces* **13**(14), 16688–16693 (2021).

[71] An, F., Qu, K., Zhong, G., Dong, Y., Ming, W., Zi, M., Liu, Z., Wang, Y., Qi, B., Ding, Z., et al. Highly flexible and twistable freestanding single crystalline magnetite film with robust magnetism. *Advanced Functional Materials* **30**(31), 2003495 (2020).

[72] Chen, Z., Wang, B.Y., Goodge, B.H., Lu, D., Hong, S.S., Li, D., Kourkoutis, L.F., Hikita, Y., and Hwang, H.Y. Freestanding crystalline $YBa_2Cu_3O_{7-x}$ heterostructure membranes. *Physical Review Materials* **3**(6), 060801 (2019).

[73] Singh, P., Swartz, A., Lu, D., Hong, S.S., Lee, K., Marshall, A.F., Nishio, K., Hikita, Y., and Hwang, H.Y. Large-area crystalline $BaSnO_3$ membranes with high electron mobilities. *ACS Applied Electronic Materials* **1**(7), 1269–1274 (2019).

[74] Bourlier, Y., Bérini, B., Frégnaux, M., Fouchet, A., Aureau, D., and Dumont, Y. Transfer of epitaxial $SrTiO_3$ nanothick layers using water-soluble sacrificial perovskite oxides. *ACS Applied Materials & Interfaces* **12**(7), 8466–8474 (2020).

[75] Chang, Y.W., Wu, P.C., Yi, J.B., Liu, Y.C., Chou, Y., Chou, Y.C., and Yang, J.C. A fast route towards freestanding single-crystalline oxide thin films by using $YBa_2Cu_3O_{7-x}$ as a sacrificial layer. *Nanoscale Research Letters* **15**, 1–8 (2020).

[76] Chiu, C.C., Chang, Y.W., Shao, Y.C., Liu, Y.C., Lee, J.M., Huang, S.W., Yang, W., Guo, J., de Groot, F.M., Yang, J.C., et al. Spectroscopic characterization of electronic structures of ultra-thin single crystal $La_{0.7}Sr_{0.3}MnO_3$. *Scientific Reports* **11**(1), 5250 (2021).

[77] Lin, B., Zhang, Y., Zhang, H., Wu, H., Shao, J., Shao, J., Liu, K., Chen, S., Zhou, C., Cheng, X., et al. Centimeter-scale two-dimensional metallenes for high-efficiency electrocatalysis and sensing. *ACS Materials Letters* **5**(2), 397–405 (2023).

[78] Tue, P.T., Shimoda, T., and Takamura, Y. Lift-off process for fine-patterned PZT film using metal oxide as a sacrificial layer. *Journal of Micromechanics and Microengineering* **27**(1), 014004 (2016).

[79] Cheng, D., Wynn, T., Lu, B., Marple, M., Han, B., Shimizu, R., Sreenarayanan, B., Bickel, J., Hosemann, P., Yang, Y., et al. A free-standing lithium phosphorus oxynitride thin film electrolyte promotes uniformly dense lithium metal deposition with no external pressure. *Nature Nanotechnology* pages 1–8 (2023).

[80] Schlom, D.G., Chen, L.Q., Fennie, C.J., Gopalan, V., Muller, D.A., Pan, X., Ramesh, R., and Uecker, R. Elastic strain engineering of ferroic oxides. *MRS Bulletin* **39**(2), 118–130 (2014).

[81] Han, L., Addiego, C., Prokhorenko, S., Wang, M., Fu, H., Nahas, Y., Yan, X., Cai, S., Wei, T., Fang, Y., et al. High-density switchable skyrmion-like polar nanodomains integrated on silicon. *Nature* **603**(7899), 63–67 (2022).

[82] Dong, G., Li, S., Li, T., Wu, H., Nan, T., Wang, X., Liu, H., Cheng, Y., Zhou, Y., Qu, W., et al. Periodic wrinkle-patterned single-crystalline ferroelectric oxide membranes with enhanced piezoelectricity. *Advanced Materials* **32**(50), 2004477 (2020).

[83] Zhou, Y., Guo, C., Dong, G., Liu, H., Zhou, Z., Niu, B., Wu, D., Li, T., Huang, H., Liu, M., et al. Tip-induced in-plane ferroelectric superstructure in zigzag-wrinkled $BaTiO_3$ thin films. *Nano Letters* **22**(7), 2859–2866 (2022).

[84] Dagotto, E., Hotta, T., and Moreo, A. Colossal magnetoresistant materials: The key role of phase separation. *Physics Reports* **344**(1-3), 1–153 (2001).

[85] Majumdar, S. and van Dijken, S. Pulsed laser deposition of $La_{1-x}Sr_xMnO_3$: Thin-film properties and spintronic applications. *Journal of Physics D: Applied Physics* **47**(3), 034010 (2013).

[86] Izumi, M., Ogimoto, Y., Manako, T., Kawasaki, M., and Tokura, Y. Interface effect and its doping dependence in $La_{1-x}Sr_xMnO_3/SrTiO_3$ superlattices. *Journal of the Physical Society of Japan* **71**(11), 2621–2624 (2002).

[87] Lu, Z., Liu, J., Feng, J., Zheng, X., Yang, L.h., Ge, C., Jin, K.j., Wang, Z., and Li, R.W. Synthesis of single-crystal $La_{0.67}Sr_{0.33}MnO_3$ freestanding films with different crystal-orientation. *APL Materials* **8**(5) (2020).

[88] Takamura, Y., Chopdekar, R., Arenholz, E., and Suzuki, Y. Control of the magnetic and magnetotransport properties of $La_{0.67}Sr_{0.33}MnO_3$ thin films through epitaxial strain. *Applied Physics Letters* **92**(16) (2008).

[89] Thiele, C., Dörr, K., Bilani, O., Rödel, J., and Schultz, L. Influence of strain on the magnetization and magnetoelectric effect in $La_{0.7}A_{0.3}MnO_3$/PMN-PT (001)(A = Sr, Ca). *Physical Review B* **75**(5), 054408 (2007).

[90] Wang, H., Shen, L., Duan, T., Ma, C., Cao, C., Jiang, C., Lu, X., Sun, H., and Liu, M. Integration of both invariable and tunable microwave magnetisms in a single flexible $La_{0.67}Sr_{0.33}MnO_3$ thin film. *ACS Applied Materials & Interfaces* **11**(25), 22677–22683 (2019).

[91] Yao, M., Li, Y., Tian, B., Mao, Q., Dong, G., Cheng, Y., Hou, W., Zhao, Y., Wang, T., Zhao, Y., et al. Freestanding single-crystal $Ni_{0.5}Zn_{0.5}Fe_2O_4$ ferrite membranes

with controllable enhanced magnetic properties for flexible RF/microwave applications. *Journal of Materials Chemistry C* **8**(47), 17099–17106 (2020).

[92] Duan, D., Yu, H., Xie, H., and Cui, T. Ab initio approach and its impact on superconductivity. *Journal of Superconductivity and Novel Magnetism* **32**, 53–60 (2019).

[93] Schilling, A., Cantoni, M., Guo, J., and Ott, H. Superconductivity above 130 K in the Hg–Ba–Ca–Cu–O system. *Nature* **363**(6424), 56–58 (1993).

[94] Yu, Y., Ma, L., Cai, P., Zhong, R., Ye, C., Shen, J., Gu, G.D., Chen, X.H., and Zhang, Y. High-temperature superconductivity in monolayer $Bi_2Sr_2CaCu_2O_{8+\delta}$. *Nature* **575**(7781), 156–163 (2019).

[95] Saito, Y., Nojima, T., and Iwasa, Y. Highly crystalline 2D superconductors. *Nature Reviews Materials* **2**(1), 1–18 (2016).

[96] Liang, R., Dosanjh, P., Bonn, D., Baar, D., Carolan, J., and Hardy, W. Growth and properties of superconducting YBCO single crystals. *Physica C: Superconductivity* **195**(1-2), 51–58 (1992).

[97] Jia, Z., Tang, C.S., Wu, J., Li, C., Xu, W., Wu, K., Zhou, D., Yang, P., Zeng, S., Zeng, Z., Zhang, D., Ariando, A., Breese, M.B.H., Cai, C., and Yin, X. Self-passivated freestanding superconducting oxide film for flexible electronics. *Applied Physics Reviews* **10**(3), 031401 (2023).

[98] Qiao, J. and Yang, C.Y. High-T_c superconductors on buffered silicon: Materials properties and device applications. *Materials Science and Engineering: R: Reports* **14**(4), 157–201 (1995).

[99] Zubko, P., Catalan, G., and Tagantsev, A.K. Flexoelectric effect in solids. *Annual Review of Materials Research* **43**, 387–421 (2013).

[100] Kogan, S.M. Piezoelectric effect during inhomogeneous deformation and acoustic scattering of carriers in crystals. *Soviet Physics Solid State* **5**(10), 2069–2070 (1964).

[101] Das, S., Wang, B., Paudel, T.R., Park, S.M., Tsymbal, E.Y., Chen, L.Q., Lee, D., and Noh, T.W. Enhanced flexoelectricity at reduced dimensions revealed by mechanically tunable quantum tunnelling. *Nature Communications* **10**(1), 537 (2019).

[102] Yang, M.M., Kim, D.J., and Alexe, M. Flexo-photovoltaic effect. *Science* **360**(6391), 904–907 (2018).

[103] Lee, D., Jeon, B.C., Yoon, A., Shin, Y.J., Lee, M.H., Song, T.K., Bu, S.D., Kim, M., Chung, J.S., Yoon, J.G., et al. Flexoelectric control of defect formation in ferroelectric epitaxial thin films. *Advanced Materials* **26**(29), 5005–5011 (2014).

[104] Tang, Y., Zhu, Y., Liu, Y., Wang, Y., and Ma, X. Giant linear strain gradient with extremely low elastic energy in a perovskite nanostructure array. *Nature Communications* **8**(1), 15994 (2017).

[105] Zhong, G., An, F., Qu, K., Dong, Y., Yang, Z., Dai, L., Xie, S., Huang, R., Luo, Z., and Li, J. Highly flexible freestanding $BaTiO_3$-$CoFe_2O_4$ heteroepitaxial nanostructure self-assembled with room-temperature multiferroicity. *Small* **18**(3), 2104213 (2022).

[106] Chiu, C.C., Ho, S.Z., Lee, J.M., Shao, Y.C., Shen, Y., Liu, Y.C., Chang, Y.W., Zheng, Y.Z., Huang, R., Chang, C.F., et al. Presence of delocalized Ti 3d electrons in ultrathin single-crystal $SrTiO_3$. *Nano Letters* **22**(4), 1580–1586 (2022).

[107] Garcia, V., Fusil, S., Bouzehouane, K., Enouz-Vedrenne, S., Mathur, N.D., Barthelemy, A., and Bibes, M. Giant tunnel electroresistance for non-destructive readout of ferroelectric states. *Nature* **460**(7251), 81–84 (2009).

[108] Chanthbouala, A., Crassous, A., Garcia, V., Bouzehouane, K., Fusil, S., Moya, X., Allibe, J., Dlubak, B., Grollier, J., Xavier, S., et al. Solid-state memories based on ferroelectric tunnel junctions. *Nature Nanotechnology* **7**(2), 101–104 (2012).

[109] Chanthbouala, A., Garcia, V., Cherifi, R.O., Bouzehouane, K., Fusil, S., Moya, X., Xavier, S., Yamada, H., Deranlot, C., Mathur, N.D., et al. A ferroelectric memristor. *Nature Materials* **11**(10), 860–864 (2012).

[110] Lu, D., Crossley, S., Xu, R., Hikita, Y., and Hwang, H.Y. Freestanding oxide ferroelectric tunnel junction memories transferred onto silicon. *Nano Letters* **19**(6), 3999–4003 (2019).

[111] Du, C., Cai, F., Zidan, M.A., Ma, W., Lee, S.H., and Lu, W.D. Reservoir computing using dynamic memristors for temporal information processing. *Nature Communications* **8**(1), 2204 (2017).

[112] Lee, H.S., Chung, J., Hwang, G.T., Jeong, C.K., Jung, Y., Kwak, J.H., Kang, H., Byun, M., Kim, W.D., Hur, S., et al. Flexible inorganic piezoelectric acoustic nanosensors for biomimetic artificial hair cells. *Advanced Functional Materials* **24**(44), 6914–6921 (2014).

[113] Gregg, J. and Bowman, R. The effect of applied strain on the resistance of VO_2 thin films. *Applied Physics Letters* **71**(25), 3649–3651 (1997).

[114] Han, J.H., Bae, K.M., Hong, S.K., Park, H., Kwak, J.H., Wang, H.S., Joe, D.J., Park, J.H., Jung, Y.H., Hur, S., et al. Machine learning-based self-powered acoustic sensor for speaker recognition. *Nano Energy* **53**, 658–665 (2018).

[115] Song, K., Ma, N., Mishra, Y.K., Adelung, R., and Yang, Y. Achieving light-induced ultrahigh pyroelectric charge density toward self-powered UV light detection. *Advanced Electronic Materials* **5**(1), 1800413 (2019).

[116] Park, K.I., Son, J.H., Hwang, G.T., Jeong, C.K., Ryu, J., Koo, M., Choi, I., Lee, S.H., Byun, M., Wang, Z.L., et al. Highly-efficient, flexible piezoelectric PZT thin film nanogenerator on plastic substrates. *Advanced Materials* **26**(16), 2514–2520 (2014).

[117] Wang, D., He, G., Hao, L., Gao, J., and Zhang, M. Comparative passivation effect of ALD-driven HfO_2 and Al_2O_3 buffer layers on the interface chemistry and electrical characteristics of Dy-based gate dielectrics. *Journal of Materials Chemistry C* **7**(7), 1955–1965 (2019).

[118] Lee, S., Luan, H., Bai, W., Lee, C., Jeon, T., Senzaki, Y., Roberts, D., and Kwong, D. High quality ultra thin CVD HfO/sub 2/gate stack with poly-Si gate electrode. In *International Electron Devices Meeting 2000. Technical Digest. IEDM (Cat. No. 00CH37138)*, pages 31–34. IEEE (2000).

[119] Siddiqui, A., Khosa, R.Y., and Usman, M. High-κ dielectrics for 4H-silicon carbide: Present status and future perspectives. *Journal of Materials Chemistry C* **9**(15), 5055–5081 (2021).

[120] Chen, L., Wang, H., Hou, B., Liu, M., Shen, L., Lu, X., Ma, X., and Hao, Y. Heterointegration of quasi two-dimensional $PbZr_{0.2}Ti_{0.8}O_3$ on AlGaN/GaN HEMT and non-volatile modulation of two-dimensional electron gas. *Applied Physics Letters* **115**(19) (2019).

[121] Chen, X., Dong, J., He, C., He, L., Chen, Z., Li, S., Zhang, K., Wang, X., and Wang, Z.L. Epitaxial lift-off of flexible GaN-based HEMT arrays with performances optimization by the piezotronic effect. *Nano-Micro Letters* **13**, 1–13 (2021).

[122] Lu, Z., Yang, Y., Wen, L., Feng, J., Lao, B., Zheng, X., Li, S., Zhao, K., Cao, B., Ren, Z., et al. Cooperative control of perpendicular magnetic anisotropy via crystal structure and orientation in freestanding $SrRuO_3$ membranes. *npj Flexible Electronics* **6**(1), 9 (2022).

[123] Alonso, J., Rasines, I., and Soubeyroux, J. Tristrontium dialuminum hexaoxide: An intricate superstructure of perovskite. *Inorganic Chemistry* **29**(23), 4768–4771 (1990).

[124] Le, P.T., Ten Elshof, J.E., and Koster, G. Epitaxial lift-off of freestanding (011) and (111) $SrRuO_3$ thin films using a water sacrificial layer. *Scientific Reports* **11**(1), 12435 (2021).

[125] Chiabrera, F.M., Yun, S., Li, Y., Dahm, R.T., Zhang, H., Kirchert, C.K., Christensen, D.V., Trier, F., Jespersen, T.S., and Pryds, N. Freestanding perovskite oxide films: Synthesis, challenges, and properties. *Annalen der Physik* **534**(9), 2200084 (2022).

[126] Mohamed, B. and Sharp, J. Kinetics and mechanism of formation of tricalcium aluminate, $Ca_3Al_2O_6$. *Thermochimica Acta* **388**(1-2), 105–114 (2002).

[127] Lazic, B., Kahlenberg, V., Kaindl, R., and Kremenović, A. On the symmetry of $Ba_3Al_2O_6$–X-ray diffraction and Raman spectroscopy studies. *Solid State Sciences* **11**(1), 77–84 (2009).

[128] Hong, S.S., Gu, M., Verma, M., Harbola, V., Wang, B.Y., Lu, D., Vailionis, A., Hikita, Y., Pentcheva, R., Rondinelli, J.M., et al. Extreme tensile strain states in $La_{0.7}Ca_{0.3}MnO_3$ membranes. *Science* **368**(6486), 71–76 (2020).

[129] Xu, R., Huang, J., Barnard, E.S., Hong, S.S., Singh, P., Wong, E.K., Jansen, T., Harbola, V., Xiao, J., Wang, B.Y., et al. Strain-induced room-temperature ferroelectricity in $SrTiO_3$ membranes. *Nature Communications* **11**(1), 3141 (2020).

[130] Shao, Y.T., Das, S., Hong, Z., Xu, R., Chandrika, S., Gómez-Ortiz, F., García-Fernández, P., Chen, L.Q., Hwang, H.Y., Junquera, J., et al. Emergent chirality in a polar meron to skyrmion phase transition. *Nature Communications* **14**(1), 1355 (2023).

[131] Bullard, J.W., Jennings, H.M., Livingston, R.A., Nonat, A., Scherer, G.W., Schweitzer, J.S., Scrivener, K.L., and Thomas, J.J. Mechanisms of cement hydration. *Cement and Concrete Research* **41**(12), 1208–1223 (2011).

[132] Barns, R. and Laudise, R. Stability of superconducting $YBa_2Cu_3O_7$ in the presence of water. *Applied Physics Letters* **51**(17), 1373–1375 (1987).

[133] Nian, L., Sun, H., Wang, Z., Xu, D., Bo, H., Li, Y., Zhou, J., Deng, Y., Hao, Y., Nie, Y., et al. $Sr_4Al_2O_7$: A new sacrificial layer with high water dissolution rate for the synthesis of freestanding oxide membranes. *arXiv preprint arXiv:2307.14584* (2023).

[134] Baek, D.J., Lu, D., Hikita, Y., Hwang, H.Y., and Kourkoutis, L.F. Mapping cation diffusion through lattice defects in epitaxial oxide thin films on the water-soluble buffer layer $Sr_3Al_2O_6$ using atomic resolution electron microscopy. *APL Materials* **5**(9) (2017).

[135] Baek, D.J., Lu, D., Hikita, Y., Hwang, H.Y., and Kourkoutis, L.F. Ultrathin epitaxial barrier layer to avoid thermally induced phase transformation in oxide heterostructures. *ACS Applied Materials & Interfaces* **9**(1), 54–59 (2017).

[136] Li, D., Adamo, C., Wang, B.Y., Yoon, H., Chen, Z., Hong, S.S., Lu, D., Cui, Y., Hikita, Y., and Hwang, H.Y. Stabilization of $Sr_3Al_2O_6$ growth templates for ex situ synthesis of freestanding crystalline oxide membranes. *Nano Letters* **21**(10), 4454–4460 (2021).

[137] Zhang, B., Yun, C., and MacManus-Driscoll, J.L. High yield transfer of clean large-area epitaxial oxide thin films. *Nano-Micro Letters* **13**, 1–14 (2021).

[138] Suk, J.W., Kitt, A., Magnuson, C.W., Hao, Y., Ahmed, S., An, J., Swan, A.K., Goldberg, B.B., and Ruoff, R.S. Transfer of CVD-grown monolayer graphene onto arbitrary substrates. *ACS Nano* **5**(9), 6916–6924 (2011).

[139] Wang, Q., Fang, H., Wang, D., Wang, J., Zhang, N., He, B., and Lü, W. Towards a large-area freestanding single-crystal ferroelectric $BaTiO_3$ membrane. *Crystals* **10**(9), 733 (2020).

[140] Gu, K., Katayama, T., Yasui, S., Chikamatsu, A., Yasuhara, S., Itoh, M., and Hasegawa, T. Simple method to obtain large-size single-crystalline oxide sheets. *Advanced Functional Materials* **30**(28), 2001236 (2020).

[141] Prinz, G.A. Magnetoelectronics. *Science* **282**(5394), 1660–1663 (1998).

[142] Song, Y.J., Lee, J.H., Shin, H., Lee, K., Suh, K., Kang, J., Pyo, S., Jung, H., Hwang, S., Koh, G., et al. Highly functional and reliable 8Mb STT-MRAM embedded in 28nm logic. In *2016 IEEE International Electron Devices Meeting (IEDM)*, pages 27–2. IEEE (2016).

[143] Parkin, S.S., Hayashi, M., and Thomas, L. Magnetic domain-wall racetrack memory. *Science* **320**(5873), 190–194 (2008).

[144] Stöhr, J. and Siegmann, H.C. Magnetism. *Solid-State Sciences* **5**, 236 (2006).

[145] Heisenberg, W. Mehrkörperproblem und resonanz in der quantenmechanik. *Zeitschrift für Physik* **38**(6-7), 411–426 (1926).

[146] Stoner, E.C. Collective electron ferromagnetism. *Proceedings of the Royal Society of London. Series A. Mathematical and Physical Sciences* **165**(922), 372–414 (1938).

[147] Pauli Jr, W. Über gasentartung und paramagnetismus. *Zeitschrift für Physik A Hadrons and nuclei* **41**(2-3), 81–102 (1927).

[148] Moriya, T. Anisotropic superexchange interaction and weak ferromagnetism. *Physical Review* **120**(1), 91 (1960).

[149] Dzyaloshinsky, I. A thermodynamic theory of "weak" ferromagnetism of antiferromagnetics. *Journal of Physics and Chemistry of Solids* **4**(4), 241–255 (1958).

[150] Néel, L. L'anisotropie superficielle des substances ferromagnétiques. *Comptes Rendus Hebdomadaires Des Seances De L Academie Des Sciences* **237**(23), 1468–1470 (1953).

[151] Skomski, R. Nanomagnetics. *Journal of Physics: Condensed Matter* **15**(20), R841 (2003).

[152] Wilts, C. and Humphrey, F. Magnetic anisotropy in flat ferromagnetic films: A review. *Journal of Applied Physics* **39**(2), 1191–1196 (1968).

[153] Malozemoff, A.P. and Slonczewski, J.C. *Magnetic domain walls in bubble materials:* A*dvances in materials and device research*, volume 1. Academic press (2013).

[154] Landau, L.D. and Lifshitz, E. On the theory of the dispersion of magnetic permeability in ferromagnetic bodies. *Physikalische Zeitschrift der Sowjetunion* **8**, 153 (1935).

[155] Gilbert, T.L. A Lagrangian formulation of the gyromagnetic equation of the magnetization field. *Physical Review* **100**, 1243 (1955).

[156] Thiaville, A., Rohart, S., Jué, É., Cros, V., and Fert, A. Dynamics of Dzyaloshinskii domain walls in ultrathin magnetic films. *Europhysics Letters* **100**(5), 57002 (2012).

[157] Hayashi, M., Thomas, L., Moriya, R., Rettner, C., and Parkin, S.S. Current-controlled magnetic domain-wall nanowire shift register. *Science* **320**(5873), 209–211 (2008).

[158] Hayashi, M., Thomas, L., Rettner, C., Moriya, R., Bazaliy, Y.B., and Parkin, S.S. Current driven domain wall velocities exceeding the spin angular momentum transfer rate in permalloy nanowires. *Physical Review Letters* **98**(3), 037204 (2007).

[159] Parkin, S. and Yang, S.H. Memory on the racetrack. *Nature Nanotechnology* **10**(3), 195–198 (2015).

[160] Chiba, D., Yamada, G., Koyama, T., Ueda, K., Tanigawa, H., Fukami, S., Suzuki, T., Ohshima, N., Ishiwata, N., Nakatani, Y., et al. Control of multiple magnetic domain walls by current in a Co/Ni nano-wire. *Applied Physics Express* **3**(7), 073004 (2010).

[161] Miron, I.M., Moore, T., Szambolics, H., Buda-Prejbeanu, L.D., Auffret, S., Rodmacq, B., Pizzini, S., Vogel, J., Bonfim, M., Schuhl, A., et al. Fast current-induced domain-wall motion controlled by the Rashba effect. *Nature Materials* **10**(6), 419–423 (2011).

[162] Ryu, K.S., Thomas, L., Yang, S.H., and Parkin, S. Chiral spin torque at magnetic domain walls. *Nature Nanotechnology* **8**(7), 527–533 (2013).

[163] Yang, S.H., Ryu, K.S., and Parkin, S. Domain-wall velocities of up to 750 m s^{-1} driven by exchange-coupling torque in synthetic antiferromagnets. *Nature Nanotechnology* **10**(3), 221–226 (2015).

[164] Garg, C., Yang, S.H., Phung, T., Pushp, A., and Parkin, S.S. Dramatic influence of curvature of nanowire on chiral domain wall velocity. *Science Advances* **3**(5), e1602804 (2017).

[165] Guan, Y., Zhou, X., Li, F., Ma, T., Yang, S.H., and Parkin, S.S. Ionitronic manipulation of current-induced domain wall motion in synthetic antiferromagnets. *Nature Communications* **12**(1), 5002 (2021).

[166] Kado, M., Tokuda, Y., Ootera, Y., Umetsu, N., Quinsat, M., Fukumizu, H., and Kondo, T. Atomic layer deposition of perpendicularly magnetized Co layers showing current-induced domain wall motion. *IEEE Transactions on Magnetics* (2023).

[167] Schöbitz, M., De Riz, A., Martin, S., Bochmann, S., Thirion, C., Vogel, J., Foerster, M., Aballe, L., Menteş, T., Locatelli, A., et al. Fast domain wall motion governed by topology and œrsted fields in cylindrical magnetic nanowires. *Physical Review Letters* **123**(21), 217201 (2019).

[168] Sanz-Hernández, D., Hamans, R.F., Liao, J.W., Welbourne, A., Lavrijsen, R., and Fernández-Pacheco, A. Fabrication, detection, and operation of a three-dimensional nanomagnetic conduit. *ACS Nano* **11**(11), 11066–11073 (2017).

[169] Bochmann, S., Fernandez-Pacheco, A., Mačković, M., Neff, A., Siefermann, K., Spiecker, E., Cowburn, R., and Bachmann, J. Systematic tuning of segmented magnetic nanowires into three-dimensional arrays of 'bits'. *RSC Advances* **7**(60), 37627–37635 (2017).

[170] Horwitz, J., Grabowski, K., Chrisey, D., and Leuchtner, R. In situ deposition of epitaxial $PbZr_xTi_{(1-x)}O_3$ thin films by pulsed laser deposition. *Applied Physics Letters* **59**(13), 1565–1567 (1991).

[171] Bonaccorso, F., Bongiorno, C., Fazio, B., Gucciardi, P., Marago, O., Morone, A., and Spinella, C. Pulsed laser deposition of multiwalled carbon nanotubes thin films. *Applied Surface Science* **254**(4), 1260–1263 (2007).

[172] Dai, Q., Sabio, E.M., Wang, W., and Tang, J. Pulsed laser deposition of Mn doped CdSe quantum dots for improved solar cell performance. *Applied Physics Letters* **104**(18) (2014).

[173] Le Lay, G. and Kern, R. Physical methods used for the characterization of modes of epitaxial growth from the vapor phase. *Journal of Crystal Growth* **44**(2), 197–222 (1978).

[174] Bragg, W.H. and Bragg, W.L. The reflection of X-rays by crystals. *Proceedings of the Royal Society of London. Series A, Containing Papers of a Mathematical and Physical Character* **88**(605), 428–438 (1913).

[175] Kittel, C. *Introduction to solid state physics*. John Wiley & sons, inc (2005).

[176] Gu, K., Guan, Y., Hazra, B.K., Deniz, H., Migliorini, A., Zhang, W., and Parkin, S.S. Three-dimensional racetrack memory devices designed from freestanding magnetic heterostructures. *Nature Nanotechnology* **17**(10), 1065–1071 (2022).

[177] Hoffmann, A. Spin Hall effects in metals. *IEEE Transactions on Magnetics* **49**(10), 5172–5193 (2013).

[178] Yang, S.H., Garg, C., and Parkin, S.S. Chiral exchange drag and chirality oscillations in synthetic antiferromagnets. *Nature Physics* **15**(6), 543–548 (2019).

[179] Maurenbrecher, H., Mendil, J., Chatzipirpiridis, G., Mattmann, M., Pané, S., Nelson, B.J., and Gambardella, P. Chiral anisotropic magnetoresistance of ferromagnetic helices. *Applied Physics Letters* **112**(24) (2018).

[180] Castellanos-Gomez, A., Buscema, M., Molenaar, R., Singh, V., Janssen, L., Van Der Zant, H.S., and Steele, G.A. Deterministic transfer of two-dimensional materials by all-dry viscoelastic stamping. *2D Materials* **1**(1), 011002 (2014).

[181] Lee, M., Renshof, J.R., van Zeggeren, K.J., Houmes, M.J., Lesne, E., Šiškins, M., van Thiel, T.C., Guis, R.H., van Blankenstein, M.R., Verbiest, G.J., et al. Ultrathin piezoelectric resonators based on graphene and free-standing single-crystal $BaTiO_3$. *Advanced Materials* **34**(44), 2204630 (2022).

[182] Deng, Y., Yu, Y., Song, Y., Zhang, J., Wang, N.Z., Sun, Z., Yi, Y., Wu, Y.Z., Wu, S., Zhu, J., et al. Gate-tunable room-temperature ferromagnetism in two-dimensional Fe_3GeTe_2. *Nature* **563**(7729), 94–99 (2018).

[183] Sheka, D.D., Pylypovskyi, O.V., Volkov, O.M., Yershov, K.V., Kravchuk, V.P., and Makarov, D. Fundamentals of curvilinear ferromagnetism: Statics and dynamics of geometrically curved wires and narrow ribbons. *Small* **18**(12), 2105219 (2022).

[184] Boulle, O., Rohart, S., Buda-Prejbeanu, L., Jué, E., Miron, I., Pizzini, S., Vogel, J., Gaudin, G., and Thiaville, A. Domain wall tilting in the presence of the Dzyaloshinskii-Moriya interaction in out-of-plane magnetized magnetic nanotracks. *Physical Review Letters* **111**(21), 217203 (2013).

[185] Ryu, K.S., Thomas, L., Yang, S.H., and Parkin, S.S. Current induced tilting of domain walls in high velocity motion along perpendicularly magnetized micron-sized Co/Ni/Co racetracks. *Applied Physics Express* **5**(9), 093006 (2012).

[186] Swindells, C., Nicholson, B., Inyang, O., Choi, Y., Hase, T., and Atkinson, D. Proximity-induced magnetism in Pt layered with rare-earth–transition-metal ferrimagnetic alloys. *Physical Review Research* **2**(3), 033280 (2020).

[187] Rowan-Robinson, R.M., Stashkevich, A., Roussigné, Y., Belmeguenai, M., Chérif, S.M., Thiaville, A., Hase, T., Hindmarch, A., and Atkinson, D. The interfacial nature of proximity-induced magnetism and the Dzyaloshinskii-Moriya interaction at the Pt/Co interface. *Scientific Reports* **7**(1), 16835 (2017).

[188] Kim, H., Choi, Y., Lewandowski, C., Thomson, A., Zhang, Y., Polski, R., Watanabe, K., Taniguchi, T., Alicea, J., and Nadj-Perge, S. Evidence for unconventional superconductivity in twisted trilayer graphene. *Nature* **606**(7914), 494–500 (2022).

[189] Park, J.M., Cao, Y., Xia, L.Q., Sun, S., Watanabe, K., Taniguchi, T., and Jarillo-Herrero, P. Robust superconductivity in magic-angle multilayer graphene family. *Nature Materials* **21**(8), 877–883 (2022).

List of Publications

Thesis related publications

[1] Gu, K., Guan, Y., Hazra, B.K., Deniz, H., Migliorini, A., Zhang, W., and Parkin, S. Three-dimensional racetrack memory devices designed from freestanding magnetic heterostructures. *Nature Nanotechnology* **17**(10), 1065–1071 (2022).
[2] Gu, K., Rigvedi, P., Wang, P., Yin, Z., Deniz, H., Migliorini, A., and Parkin, S. Atomically-thin freestanding racetrack memory devices. *Advanced Materials* 202505707 (2025).
[3] Li, F., Gu, K., Guan, Y., Pan, Y., Deniz, H., Felser, C., and Parkin, S. Magnetic twist for twistronics: Freestanding correlated oxide. (co-first author, to be submitted).

Other publications

[1] Gu, K., Katayama, T., Yasui, S., Chikamatsu, A., Yasuhara, S., Itoh, M., and Hasegawa, T. Simple method to obtain large-size single-crystalline oxide sheets. *Advanced Functional Materials* **30**(28), 2001236 (2020).
[2] Wang, P., Saha, R., Meyerheim, H., Gu, K., Deniz, H., Migliorini, A., Eilmsteiner, D., Rubio-Zuazo, J., Sebastiani-Tofano, E., Ernst, A., and Parkin, S. Hot skyrmions in ferromagnets via strain gradients. (under review).
[3] Li, F., Guan, Y., Wang, P., Wang, Z., Fang, C., Gu, K., and Parkin, S. All-electrical reading and writing of spin chirality. *Science Advance*s **8**(50), eadd6984 (2022).
[4] Katayama, T., Kurauchi, Y., Mo, S., Gu, K., Chikamatsu, A., Galiullina, L., and Hasegawa, T. p-Type conductivity and room-temperature ferrimagnetism in spinel MoFe2O4 epitaxial thin film. *Crystal Growth & Design* **19**(2), 902–906 (2018).

Curriculum Vitae

First Name: Ke

Family Name: Gu

Education

05/2020 – present	Ph.D. candidate (Physics) Max Planck Institute of Microstructure Physics, Halle (Saale), Germany Martin Luther University Halle-Wittenberg, Halle (Saale), Germany Supervisor: Prof. Stuart Parkin
09/2017 – 09/2019	Master of Science Solid-state Chemistry Lab The University of Tokyo, Tokyo, Japan Supervisor: Prof. Tetsuya Hasegawa
09/2013 – 06/2017	Bachelor of Science Department of Materials Physics Nanjing University, Nanjing, China